LSBU EST 1892

Single-shot femtosecond laser ablation of nano/polycrystalline titanium investigated using molecular dynamics and experiments

George Parris

https://orcid.org/0000-0003-4496-842X

A thesis submitted in partial fulfillment of the
requirements of London South Bank University
for the degree of Doctor of Philosophy

January 2024

Abstract

Laser ablation, a crucial technique in various scientific and industrial fields, plays a pivotal role in precision manufacturing. Industries such as aerospace rely on laser technology for tasks like drilling microscale holes in jet turbine components to enhance air-cooling efficiency. Moreover, laser-based material processing is indispensable in addressing healthcare challenges with facilitating the postprocessing of 3D-printed bespoke components like patient-specific implants as an example. Ultrashort pulsed laser ablation enables precise micro and nanofabrication, enhancing material properties like wettability, adhesion and biocompatibility. This is particularly important in medical applications like implant development, as it can help reduce the possibility of post-surgery infections.

Scientifically, understanding the intricacies of ultrashort pulsed laser ablation contributes to ongoing research and development efforts in ablation technology, fostering the enhancement of new material properties related to surface modifications. Additionally, laser ablation plays a crucial role in additive manufacturing technology like 3D printing of metals by facilitating the post-processing stage.

This thesis investigates the ultrashort pulsed laser ablation of titanium, utilising a combination of molecular dynamics simulations and experiments. Molecular dynamics simulations are used for their capability to model systems at the atomistic scale and ultrashort timescale (femtoseconds in this work), in contrast to the finite element method, and for their computational efficiency compared to methods employing more detailed calculations like density functional theory. The primary focus of this work is on exploring the size effect by examining variations in beam spot diameter and grain size with profound implications for ultraprecision manufacturing of titanium surfaces in sub-micron length scale, produced by casting and additive manufacturing techniques. It contributes a nuanced understanding of ultrashort pulsed laser ablation by bridging the gap between molecular dynamics simulations and experiments. It extends the boundaries by simulating the largest feasible atomistic models and measuring features at the smallest scale permitted by the available metrology devices in experiments.

The key observations showed the critical importance of the beam spot diameter in determining the laser fluence necessary to achieve average plasma temperatures of

around 9,000 K, as well as a direct correlation between the grain size and the response of the material to laser irradiation. Notably, the simulations indicated that the 10 nm laser beam spot diameter compared to the 25 nm requires 59% more absorbed laser energy for ablation. Furthermore, the investigation revealed that by increasing the grain size in alpha-phase titanium, when the number of grains in the volume of 500,000 nm^3 were reduce from 500 grains to 10, 36% more absorbed laser fluence was necessary to achieve average plasma temperatures of approximately 9,000 K, despite the material exhibiting higher heat conductivity.

Additionally, a comparative analysis of ultrashort pulsed laser ablation between atomistic models of pure titanium with single crystal and polycrystalline structures were carried out using molecular dynamics simulations. The results revealed that the nanocrystalline sample modelled in this work, which exhibited lower heat conduction, produced a relatively deeper crater compared to its single crystal counterpart. The single crystal sample had a greater resistance to ablation, leading to the formation of a recast layer with rougher edges in contrast to the nanocrystalline sample.

In materials science and engineering "size effect" is attributed to a phenomenon where the mechanical, thermal, optical or electrical properties of a crystalline material changes as a function of its physical size where at least one dimension is in submicron length scale. Experimental examination of the size effect was carried out on commercially pure titanium (consisting of 99.6% titanium and the remaining 0.4% containing carbon, nitrogen, hydrogen, iron and oxygen atoms) and Ti-6Al-4V alloy where craters were formed on both materials using single-shots with identical fluence while varying the diameter of the laser beam. It was observed that reducing the beam spot diameter resulted in relatively shallower craters, suggesting an increased threshold for ablation.

Experiments comparing single-shot laser ablation outcomes between casted and 3D-printed Ti-6Al-4V alloy revealed that the 3D-printed surface ($R_a = 32\ nm$) produced a slightly cleaner crater and smoother recast layer compared to the casted material ($R_a = 45\ nm$). This observation was made after subjecting both substrates to ultrashort pulsed laser irradiation with identical laser parameters.

Acknowledgements

I would like to express my deepest gratitude to my supervisors Prof. Saurav Goel (London South Bank University), Dr. John Buckeridge (London South Bank University) and Dr. Xiaowang Zhou (Sandia National Laboratories, USA) whose guidance, expertise and unwavering support have been instrumental throughout this challenging yet rewarding journey. Your mentorship, wisdom and encouragement have shaped not only the trajectory of my research but also my growth as a scholar.

Sincere thanks to Prof. Deborah Andrews (London South Bank University) who chaired the annual reviews, Dr Elsa Aristodemou (London South Bank University) who oversaw my academic milestones and Dr Dihn T Nguyen (London South Bank University) for providing expert feedback. Your guidance and insights during these critical assessments have been invaluable to my progress.

I am also deeply grateful to the examiners, Prof. Simon Philbin (London South Bank University) and Dr. Chi Wai Chan (Queen’s University Belfast) who diligently assessed my thesis and Prof. Hari Upadhyaya (London South Bank University) for chairing the session. Their insightful feedback and rigorous examination contributed significantly to the refinement of my research.

My heartfelt thanks extend to my five dedicated peers, Mr. Ali Tousi (Cranfield University), Dr. Sara Hawi (Cranfield University), Mr. Syed Mehade Hussain (London South Bank University), Ms. Caaisha Warsame (London South Bank University) and Ms. Beth Muthoni Irungu (London South Bank University) as well as postdoctoral researchers Dr. Nirmal Kumar Katiyar (London South Bank University) and Dr Vishwanathan Venkatachalapthy (Stony Brook University, USA) whose intellectual insights, constructive critiques and camaraderie have enriched the research environment and made this academic endeavour a collaborative and stimulating experience.

Special thanks to Dr. Patrick Salter (University of Oxford) whose technical expertise was crucial to the success of the experimental aspects of my research. Your dedication and proficiency have left an indelible mark on the outcome of this work. Sincere thanks also to Dr. Evans Mogire, John Sharples and John Dunlop from Buehler Solutions Centre at the University of Warwick who played a crucial role in

preparing the samples for experiments and microscopic analysis. Your meticulous efforts and expertise were essential to the success of the experiments.

To my partner in crime, Katharina, your unwavering support, understanding and patience have been my anchor during the highs and lows of this doctoral pursuit. Your belief in me has been a source of strength and I am grateful for the countless sacrifices you have made to see me succeed. I extend my appreciation to our furry companions, Pashi and Haps whose wagging tails and playful antics provided moments of joy and stress relief, reminding me to embrace the lighter side of life.

I also would like to acknowledge the use of Grammarly editing tool, which was helpful in refining the language and structure of this document. Its grammar, punctuation and style tools aided in ensuring clarity and coherence in various parts of this work.

Finally, I extend my sincere appreciation to the London South Bank University for offering me this fully funded scholarship as well as everyone who has played a part in shaping this academic endeavour. Thank you all for being an integral part of this transformative journey.

Table of Contents

List of tables

List of figures

List of abbreviations

Abbreviation	**Full Phrase**
AFM	Atomic Force Microscopy
BCC	Body-Centred Cubic
CP	Commercially Pure
CPA	Chirped Pulse Amplification
Cr: YAG	Chromium Yttrium-Aluminium-Garnet
CT	Computed Tomography
DFT	Density Functional Theory
DP	Double Pulse
EAM	Embedded Atom Method
FE	Finite Element
FIB	Focused Ion Beam
GND	Geometrically Necessary Dislocations
HAZ	Heat Affected Zone
HCP	Hexagonal Close-Packed
HOS	Hyperbolic One-Step
HTS	Hyperbolic Two-Step
IB	Inverse Bremsstrahlung
LAMMPS	Large-scale Atomic/Molecular Massively Parallel Simulator
LIPSS	Laser Induced Surface Structuring
MD	Molecular Dynamics
MMD	Modified Molecular Dynamics
Nd: YAG	Neodymium Yttrium-Aluminium-Garnet
NPT	isobaric-isothermal thermostat
PIC	Particle-In-Cell
PLD	Pulsed Laser Deposition
POS	Parabolic One-Step
PPM	Parts Per Million
PTS	Parabolic Two-Step
Q	Laser Cavity Gain
RPM	Revolutions Per Minute
SEM	Scanning Electron Microscopy

SMAT	Surface Mechanical Attrition Treatment
SPD	Severe Plastic Deformation
TTM	Two-Temperature Model
USP	Ultrashort Pulsed
XRD	X-Ray Diffraction
XRF	X-ray fluorescence

List of publication

1. Parris, G. *et al.* A critical review of the developments in molecular dynamics simulations to study femtosecond laser ablation. *Materials Today: Proceedings*, 2022, 64, pp. 1339–1348. DOI: https://doi.org/10.1016/j.matpr.2022.03.723.

Chapter 1 — Introduction

1.1. Motivation

This research project is focusing on modifying surfaces of implants made of titanium alloys to enable a bactericidal effect with the prospect of reducing the possibility of post-surgery infections. Considering recent advancements in laser technology, the most effective scalable method for manufacturing bactericidal surfaces is through surface modification using Ultrashort Pulsed (USP) lasers [1]. However, the presence of structural damage and the lack of determinism in achieving precise shape accuracy during the ablation process, particularly around the Heat Affected Zone (HAZ), impede progress in the commercial viability of laser processing of nanostructures on implant surfaces [2]. This research study aims to investigate the mechanisms underlying the USP laser ablation process, employing cutting-edge atomistic simulation method. Ultimately, this augmented comprehension of the mechanisms at play will facilitate the development of an optimal configuration for the USP laser ablation procedure, thereby providing enhanced control over the process.

1.1.1. Overview of surface modification techniques

Most recently, diverse methodologies for altering the surface topography of engineering materials have been developed. The fabrication of nanostructures with the desired precision is a complex procedure and to date, laser-based precision manufacturing stands out as the most scalable and commercially viable tool capable of producing features as small as 100 nm. Generally, manufacturing techniques fall into three principal categories. One group embraces the bottom-up approach, known as additive manufacturing, which encompasses methods like chemical deposition, sol-gel processes and electrospinning. The second group involves restructuring or patterning techniques, such as Laser Induced Periodic Surface Structuring (LIPSS). The final category constitutes the top-down approach, referred to as subtractive manufacturing, which includes methods like lithography and plasma etching [3]. Although these techniques can produce nanoscale features, challenges persist in terms of precision, complexity, uniformity and repeatability. However, laser ablation, classified as a subtractive process, holds promise in addressing these concerns due to its exceptional accuracy and high-power output. This versatile technology modifies surfaces across a broad range of materials without necessitating masks, templates or sacrificial substances. Furthermore, it has a relatively uncomplicated setup compared to most other methods and often entails a single-pass operation. Notably, it offers substantial control in creating uniform, intricate and multiscale (hierarchical) geometries consistently. Its scalability, coupled with the ability to achieve precise and complex structures, positions laser ablation as a key player in advancing the field of nanostructure fabrication for diverse applications.

1.1.2. Challenges and considerations in USP laser ablation

Femtosecond laser ablation of metals comes with its share of challenges and limitations. One critical factor in this process is the beam spot size, representing the diameter of the focused laser beam on the material surface. The choice of beam spot size plays a pivotal role in addressing or exacerbating some of the challenges associated with femtosecond laser ablation. Efficient material removal is a fundamental goal in laser ablation, and the beam spot size directly influences this aspect. While a smaller spot size allows for concentrated energy delivery it also introduces challenges. The risk of excessive thermal effects increases with a smaller spot size, as the energy is densely packed into a smaller area. This can lead to issues like melting and recrystallisation, compromising the precision and quality of the ablated surface.

Spatial resolution and precision are crucial in applications requiring fine details and intricate patterns. Smaller spot sizes generally result in higher spatial resolution, enabling the creation of intricate structures. However, finding the right balance is essential, as extremely small spot sizes may lead to increased pulse overlap, potentially exacerbating thermal effects and compromising the desired precision. The influence of beam spot size extends to material-specific considerations. Metals with varying reflective properties may require adjustments to the spot size to optimise energy absorption and enhance ablation efficiency. Additionally, the dynamics of the plasma plume, which consists of particles ejected during the ablation process, are impacted by the beam spot size. Controlling the plasma plume is crucial to prevent re-deposition of particles on the ablated surface and maintaining the quality of the final product. Perriére et al [4] emphasised the crucial impact of the laser beam spot size on nanoparticle formation in femtosecond pulsed laser deposition. Their experiments revealed significant variations in emission results (droplets or nanoparticles) despite similar initial thermodynamic conditions, highlighting the pivotal role of the laser beam spot size. They argued that the geometric effect observed across diverse target materials, challenges existing theoretical models that have overlooked the role of laser beam spot size in predicting the outcomes.

Process control is another challenge in femtosecond laser ablation and the beam spot size plays a central role in achieving precise and controlled material removal. Adjusting the spot size allows for optimisation based on the specific requirements of the application, helping to avoid under- or over-processing. However, achieving a balance that meets the demands of the application without compromising other aspects of the process poses an ongoing challenge. While femtosecond laser ablation offers remarkable capabilities, addressing the challenges and limitations requires a nuanced understanding of the role played by parameters such as beam spot size. Achieving optimal results involves a delicate balance, and ongoing research aims to refine the process and broaden the applicability of femtosecond laser ablation in various fields.

Furthermore, the choice of manufacturing method of titanium, such as casting or 3D printing, also affects the efficacy of femtosecond laser ablation process. In the context of casting titanium, challenges arise from the potential creation of irregularities and microstructural anomalies, introducing complexities for the femtosecond laser in achieving efficient material removal. The inherent surface quality of casted titanium may not be optimally smooth, thereby affecting the performance of the laser ablation process. Conversely, in the case of 3D printed titanium, the precision afforded by additive manufacturing techniques allows for intricate shapes, yet the layered structure and potential stresses introduced into the material may pose challenges for femtosecond lasers, particularly in achieving extremely fine details.

Moreover, variations in material properties between casted and 3D printed titanium play a pivotal role. While casted titanium may exhibit differences in casting quality and impurity content, the specific additive manufacturing method in 3D printed titanium becomes a factor in determining the interaction of the material with femtosecond lasers. Ongoing research seeks to address these challenges and enhance the compatibility of femtosecond laser ablation with titanium in diverse manufacturing contexts.

While technological challenges in fully harnessing this tool exist, the primary limitation of laser ablation is the scale of HAZ and undesired burr and material resolidification associated with HAZ [2,5,6]. Nevertheless, the development of femtosecond pulsed lasers has raised expectations of athermal laser ablation. Thus, a meticulous exploration of the mechanisms underlying energy transfer until the equilibrium state, holds the potential to provide vital insights. Lin and Hong [7] illustrated the extent of the HAZ as a factor of the pulse duration in Figure 1.1 with comparing the craters created by an identical laser fluence and wavelength of durations, 3.3 ns and 200 fs.

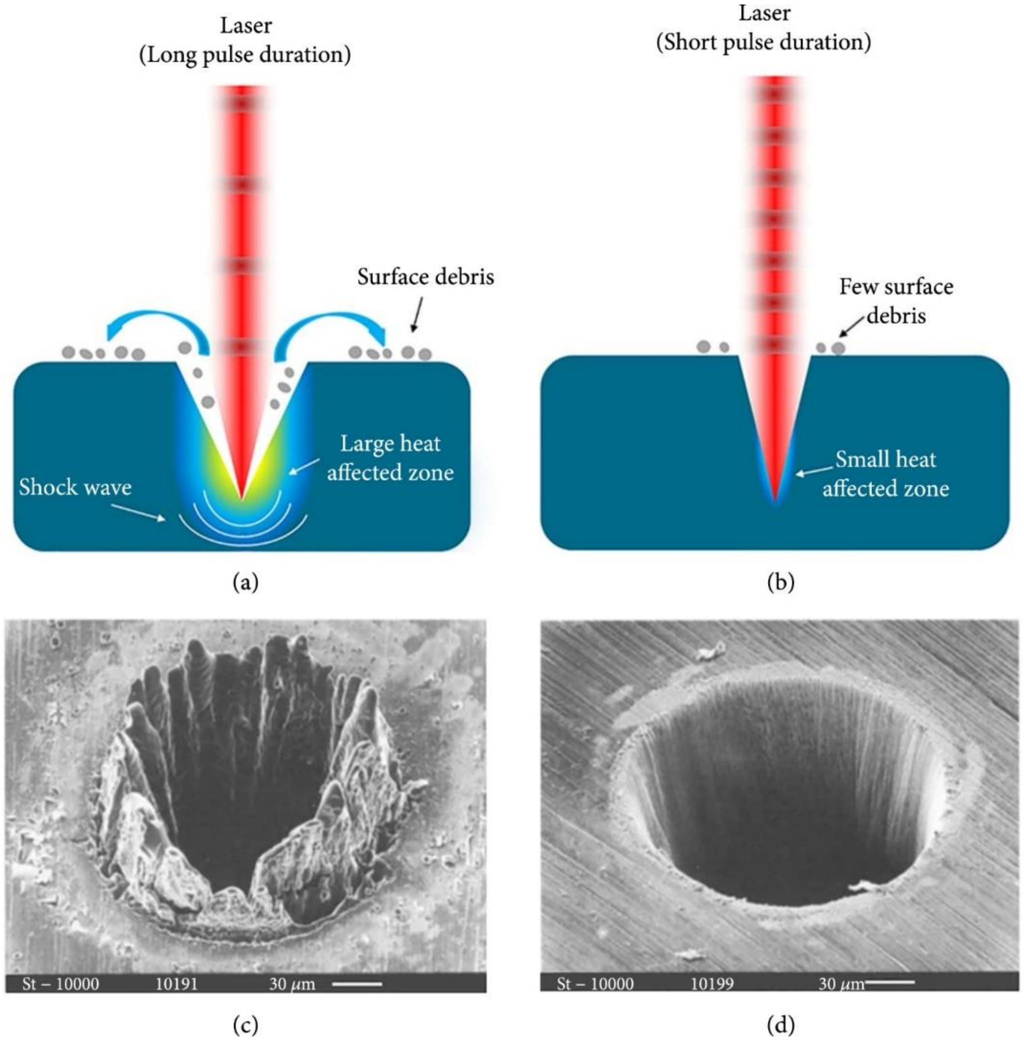

Figure 1.1 - Schematic of laser interaction with materials under different pulse durations: (a) long pulse duration and (b) short pulse duration. SEM images of laser ablated holes fabricated on a 100 μm steel foil by (c) 780 nm nanosecond laser of 3.3 ns, 0.5 J/cm and (d) 780nm femtosecond laser of 200 fs, 0.5 J/cm2 [7].

Investigating USP laser ablation at the atomic scale through experimental means poses significant challenges. Mathematical modelling of USP laser ablation relies on heat transfer equations, which are adapted to depict distinct electron and lattice temperatures in a state of nonequilibrium. The foundation of this approach lies in the two-temperature electron transport model, originally proposed by Kaganov et al [8] in 1956. This model has since served as a framework for simulating heat transfer mechanisms at the atomistic level. The timespan during which electrons are excited by an incoming laser irradiation within the material's optical penetration depth, is known as the electron thermalisation time. During this period, electrons briefly collide with each other, a moment that scientists typically consider instantaneous and omit from equations for simplification. Subsequently, they undergo collisions with the lattice, marking the onset of energy transfer known as the electron-phonon thermalisation time. This process generally takes around 10 picoseconds (subject to temperature, electron density and related factors) before energy transfer initiates. This principle underpins the concept of cold laser ablation.

In theory, for beams incident on a target for durations of less than approximately 10 picoseconds, no energy should be transferred to the lattice. However, this theoretical premise does not entirely align with experimental observations and warrants further discussion. The subsequent stage involves phonon-phonon collisions, that is referred to as thermal diffusion in continuum physics [9]. This process involves multiple variables, encompassing material properties, laser parameters and ambient conditions, all of which can be individually fine-tuned. Their cumulative impact can then be adjusted in relation to other contributing factors.

1.1.3. Insights from Molecular Dynamics simulations

Molecular Dynamics (MD) simulations offer a unique avenue to observe and analyse swiftly evolving atomistic systems through a virtual representation akin to real-life experiments. The necessity of making assumptions when constructing inputs for the simulation is inevitable, often undergoing revision when the outcomes fall short of expectations. Numerical modelling of USP laser ablation process has similarly undergone multiple revisions, demonstrating considerable enhancement, particularly within the last two decades, thanks to improved accessibility and the advancement of computational capabilities and scientific inquiry. Marla et al [9] conducted a review of the evolution of laser ablation modelling, focusing on developments up to a decade ago. Their study emphasised the identification and integration of time-critical chains of events into calculations by several researchers, yielding a significant improvement in modelling precision. Subsequently, the emergence of software tools such as LAMMPS and DL-POLY has expedited the expansion of knowledge in this domain.

Remarkably, the scientific understanding of individual processes within laser ablation has matured, gradually finding its place within modelling efforts, thus unveiling the interconnectedness among various processes. A notable instance of this is showcased in the work of Pisarev and Starikov [10], who modified two-temperature model (TTM) simulations by incorporating the temperature dependency of electronic specific heat capacity into calculations.

In a recent investigation, Zhang et al [11] explored the intricacies of laser ablation on a metallic (Ni3Al) surface using MD simulations. In an innovative method, they employed an approach that involved interpolating simulation outcomes from a computationally efficient local beam volume. This creative workaround allowed them to analyse the nonuniform (Gaussian) energy distribution profile of the entire system. Their findings reveal three distinctive phase transition mechanisms: phase explosion, photomechanical spallation and melting. Interestingly, they reported a direct correlation between these behaviours and the intensity profile of the laser beam.

1.1.4. Future directions and implications

While the Gaussian shape of laser beams is established knowledge in physics, its implications in laser-matter interactions have been predicted, albeit, not comprehensively integrated into laser ablation simulations. It is noteworthy that the practical Gaussian energy distribution of laser beams can be manipulated using various commercially available beam shapers. For example, energy distribution can be transformed into a flat-top spread. Furthermore, contemporary optics allow for alteration of the beam spot shape itself into different geometries, such as square or rectangular, consequently influencing both the energy distribution and the resulting crater shape. This aspect presents an avenue for significant advancements in material processing with laser tools, an area that has been relatively underexplored within simulation studies thus far.

The potential array of opportunities arising from laser-based micro and nano surface structuring paints a future that may feature an unprecedented level of ultra-precision manufacturing, beyond our current imagination. As emphasised in numerous laser ablation studies, a critical aspect in refining fabricated surfaces with optimal resolution lies in minimising the HAZ. Consequently, imperative further research is needed to gain a deeper understanding of the processes involved, paving the way for effective solutions.

This project is designed to dissect the mechanisms underlying USP laser ablation processes through the simulation of a select configurations. The overarching aim is to pinpoint and regulate the effects of each individual and collective variable in this process, ultimately mitigating the damage associated with the HAZ. Central to this investigation is the quest to determine the most favourable interrelationships among various tool configurations, leading to distinct laser energy distributions and mode shape geometries. To accomplish this, a comparative study is conducted, analysing the responses of single crystal and polycrystalline substrates of the same material (titanium in this study) when subjected to femtosecond pulsed laser irradiation. Additionally, samples of Ti-6Al-4V alloy manufactured by casting and 3D printing were analysed experimentally to explore the influence of the manufacturing method in material response to the USP laser irradiation. The insights gained from this research not only expand our understanding of this domain but also hold the potential to improve ultra-precision manufacturing techniques for titanium and similar materials that are extensively used in implant manufacturing and beyond.

1.2. Thesis aim

The aim is to advance the understanding of ultrashort pulsed laser ablation of titanium, particularly focusing on the effects of beam spot size as a laser parameter and grain size as a material property, with the overarching goal of guiding the future research that can contribute to practical applications using laser ablation.

1.3. Thesis objectives

- Investigate ultrashort pulsed laser ablation of titanium through molecular dynamics simulations and experimental examinations, encompassing variations in beam spot diameter and grain size.
- Examine the relationship between size effects in laser ablation with a focus on adjusting beam spot diameters for precision manufacturing applications such as fabricating nanostructures on metallic surfaces to enhance surface properties.
- Determine the influence of grain size on the efficiency of ultrashort pulsed laser ablation, exploring the correlation between grain size, ablation threshold and heat conductivity during the process.
- Conduct a comparative analysis of laser ablation outcomes on different grades of titanium, including commercially pure titanium with single crystal and polycrystalline structures, as well as casted and 3D-printed Ti-6Al-4V alloy.
- Bridge the gap between molecular dynamics simulations and experimental results by comparing the results and providing a nuanced understanding of the size effects and material distinctions in ultrashort pulsed laser ablation.
- Integrate research results into practical solutions, offering insights for precision manufacturing applications based on size effects and material considerations.
- Identify potential areas for further research and exploration in ultrashort pulsed laser ablation of titanium, contributing to the advancement of laser technologies and the development of new surface characteristics and their applications in the field.

1.4. Thesis structure and overview

A detailed roadmap is provided here to help with following the content of this thesis. The thesis embarks on a comprehensive exploration of USP laser ablation of titanium, employing a combination of simulations and experiments. In the introductory chapter, the motivation behind the study is presented.

The literature review in Chapter 2 is delving into the existing body of knowledge, covering lasers mathematical modelling and USP laser ablation. Historical developments, physical mechanisms and recent advancements are explored, concluding with a summary that bridges the literature to the current research.

In Chapter 3, the scope of the literature review is broadened to offer a comprehensive exploration of the size effect. This phenomenon, acknowledged for its substantial influence on materials' responses at micro and nanoscales. The chapter explains the challenges posed by the size effect and highlights the distinct opportunities it presents by inducing alterations in various material properties.

Chapter 4 outlines the research methodology, detailing material properties, simulation techniques and experimental procedures. From substrate preparation to laser ablation, each step is explained, offering insight into the tools and techniques used for data collection, including SEM and AFM.

In Chapter 5, the MD simulations is utilised, investigating differences in laser ablation between single crystal and nanocrystalline titanium. The simulation setup and results are presented, providing insights into these materials’ response to USP laser ablation.

Chapter 6 focuses on experimental investigations, comparing laser ablation outcomes between casted and 3D-printed Ti-6Al-4V alloy. The introduction outlines the significance of this comparison, followed by a presentation of experimental results, providing the experimental results.

Chapter 7 is focused on the size effect in USP laser ablation, exploring mechanical properties, melting point and heat conductivity concerning size variations. A detailed investigation into the size effect with varying beam spot diameters and nanocrystal sizes are presented. Experimental evaluations are also included, supported by AFM analyses, leading to a conclusive summary.

The discussion and conclusions in Chapter 8 outlines the contribution to knowledge by this project, summarises key findings, engaging in a discussion of results from both simulations and experiments. It interprets the implications of the size effect and the distinctions between materials and manufacturing techniques, concluding with overarching conclusions and avenues for future research.

The references provide a comprehensive list of all cited sources, offering the opportunity to explore the referenced literature in detail.

Lastly, the appendices include material certifications for pure titanium (cast), titanium alloy Ti-6Al-4V (cast), and titanium alloy Ti-6Al-4V (powder) used in 3D printing. These certifications provide supplementary information and validation for the materials used in the study.

Chapter 2 — Literature review

2.1. Lasers

Modern ultra-precision manufacturing owes its achievements to a lineage of inventions and innovations, continually expanding by integrating tools ranging from diamonds to lasers [12,13,14]. Lasers, having been recognised as potent energy sources since the 19th century, have undergone thorough examination for their interaction with matter. Einstein's elucidation of the photoelectric effect, attributing quantised energies to wavelike particles called photons - traveling straight at a speed of approximately 0.3 million km/s - forms the bedrock of contemporary understanding of light-matter interactions. This understanding, in turn, underpins the invention of modern laser tools, a pivotal moment shaping the evolution of ultra-precision manufacturing and metrology. Among the remarkable traits of lasers in this context are their coherence, exceptionally narrow frequency or short pulse/time (near monochromaticity within an exceedingly slender spectral range or ultra-short pulses), ability to produce highly collimated beams that can be focused onto minute spots, and controllable high-power output.

From the foundational principles of light-matter interactions, emerged the discipline of photonics, a critical branch of science. However, a scrutiny of the fundamental comprehension of laser-matter interactions reveals that the majority of the insights are primarily derived from observed experimental effects. Surprisingly, there has been relatively scant focus on employing atomistic simulations, a versatile approach to explore this subject, which holds significance in refining atomic-level material removal processes. This project attempts to delve into the evolution of available atomistic simulation methodologies, spotlighting potential opportunities as well as existing limitations.

The credit for the invention of the laser is bestowed upon Theodore Maiman, an American engineer and physicist, who in 1961 showcased the phenomenon of stimulated optical emission in ruby [15]. The progress of laser technology has been significant since then. Figure 2.1 illustrates the timeline of laser power outputs, offering a glimpse into its historical growth and anticipated trajectory.

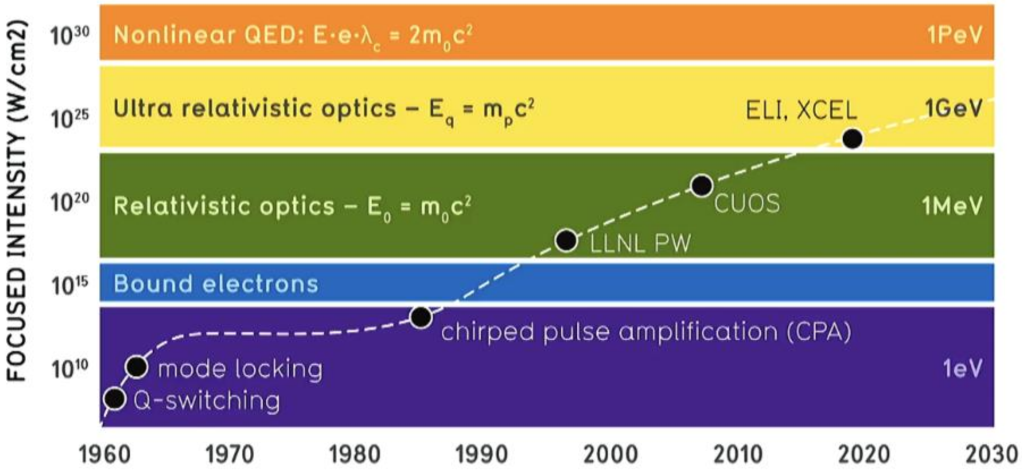

Figure 2.1 - Laser intensity vs years [16].

In the present era, lasers are categorised into two primary types based on their operational modes: continuous wave (CW) and pulsed lasers. Continuous wave lasers are predominantly employed in manufacturing for thermal processes such as cutting, welding and laser annealing, particularly on larger length scales. In contrast, pulsed lasers find their niche in ultra-precision manufacturing. Pulsed lasers encompass a range of pulse durations and qualities, with the ultrashort pulse realm garnering increasing attention within the material processing sector due to its high power density and minimised thermal impact. The consensus generally holds that longer laser pulses are more cost-effective and capable of depositing higher energy. However, as the pulse duration diminishes, the HAZ becomes smaller, leading to reductions in burring and the thickness of often undesirable recast layers [17].

Laser machines are optical oscillators comprising three fundamental components. The first component is the active laser medium, which can be in solid, liquid or gaseous form. This component serves as the source of optical gain and often determines the laser machine's associated wavelength. Common active mediums include CO2, ruby, titanium-sapphire and yttrium-aluminium-garnet doped with neodymium ions (Nd:YAG) among others. The next component is a pumping mechanism responsible for compensating for losses within the system by introducing external energy, thereby sustaining the gain bandwidth. Various methods, such as arc lamps, electric discharge and sometimes another laser beam are employed to inject energy into the system. Finally, a reflective mirror and a partially reflective mirror, positioned on opposite sides of the active medium, facilitate the oscillation of stimulated emission. They allow a portion of the generated beam to exit as the output and enable the tuning of oscillating modes within the gain curve. However, to generate pulses with higher peak power additional components and processes are required.

In contemporary laser technology, two commonly used techniques for achieving higher peak power pulses are passive and active Q-switching as well as mode-locking. Q-switching enables the generation of pulses in nanosecond and picosecond range, while mode-locking can produce pulses in femtosecond regime and even shorter durations.

2.1.1. Q-switching

In passive Q-switching, the addition of a saturable absorber material within the cavity regulates the flow of the output beam. These devices possess a variable transmission that increases when the laser intensity surpasses a specific threshold. Initially, the laser power saturates the absorber, causing an increase in loss until the gain accumulates and reaches the threshold. At this point, the resonator loss rapidly decreases, and the heightened gain (Q) is expelled from the cavity. Following the pulse, the material recovers before the gain sufficiently grows, resulting in a delay before the next pulse. The pulse frequency in such systems is controlled by adjusting the pumping power. Examples of Q-switching additives include doped crystals like Cr:YAG, passive semiconductor devices or bleachable dyes.

Active Q-switching operates on the same principle but differs in the switching mechanism, which is triggered and externally controlled. Various means, such as a mechanical variable attenuator like a shutter, rotating optics, a chopper wheel or more commonly, optical, acoustic or electrical modulators are used to manipulate resonator losses. Active switching, in general, is superior to passive methods because it provides greater control over the switching process, enables faster transitions from low to high Q and allows for externally generated beams to be coupled into the cavity, expanding the range of tunability. Karlsons et al [18] first reported a successful Q-switching experiment in a CaWO4:Nd3+ laser in 1963. Nowadays, Nd:YAG lasers are the most commonly employed laser systems in research that utilise this technology.

2.1.2. Mode-locking

Mode-locking, an additional technique for generating laser pulses was developed in the mid-1960s and is capable of compressing the resonator gain into ultra short pulses with durations in picosecond and femtosecond range. This method like Q-switching can be implemented using active, passive or hybrid setups. In mode-locking, variable attenuators and varying cavity lengths are utilised to create specific conditions that align a certain number of frequency modes beneath the gain curve of the cavity, effectively consolidating them into a single pulse. The intensity of this pulse is equivalent to the sum of the intensities of its constituent modes. Key parameters include the number of modes under the curve (which must be a multiple of C/2L), equidistant spacing between these modes and synchronised propagation of frequencies [19]. Despite the potential for femtosecond pulsed lasers to reach exceedingly high intensities, the technological and physical limitations of optical amplification in lasers often exceed the maximum tolerance of available materials used in current optical components. Consequently, there is an upper limit to the laser intensity that can be safely managed by optics before interactions occur with the beam, often resulting in collateral damage to optical components.

To overcome this limitation, Donna Strickland, a PhD student, and her supervisor Gerard Mourou developed a groundbreaking technique called Chirped Pulse Amplification (CPA) in 1985 [20]. Their innovative work earned them the Nobel Prize in Physics in 2018. The fundamental principle of CPA involves elongating a high-intensity pulse into a spectrum of distinct frequencies before entering the amplifier and subsequently compressing the amplified spectrum back into the original pulse. Following this innovation, a wide range of pulse durations and intensities combined with a practical wavelength, became achievable. This expanded range of options provides a promising platform for precise, rapid and efficient material processing in modern applications.

2.2. Early-stage development of numerical modelling

Laser-matter interaction is a complex phenomenon influenced by numerous variables that shape its outcome. As laser technology advances, particularly in ultrashort pulse generation, timescale emerges as a crucial factor. In a chronological review of laser ablation modelling by Marla et al [9], it is argued that in the early days of laser development, the interaction with matter was thought to be a straightforward process, a single-step radiation on the target leading to an instantaneous conversion into heat, subsequently elevating its temperature. Numerical modelling of this process was achieved through Fourier's heat conduction equation with the addition of laser heat as the source term. These parabolic models, aptly referred to as Parabolic One-Step (POS) models, provided accurate results for pulse durations in the nanosecond range. However, as pulses became shorter, reaching durations less than 100 picoseconds, these models began to deviate from experimental observations and could no longer accurately represent the intricate processes.

In 1993, Qiu et al [21] raised questions about the fundamental assumption of instantaneous laser-induced heat propagation within materials. They proposed a more accurate representation involving the wave-like propagation of heat, incorporating a finite rate of heat transfer. This transformation led to the modification of the POS equation, giving rise to what is now known as the Hyperbolic One-Step (HOS) method. Interestingly, nearly four decades before Qiu et al's [21] work, Kaganov et al [8] in 1955 had already predicted that heat energy is absorbed by electrons, emphasising the existence of a finite energy transfer rate between electrons and the lattice. Subsequently, in 1974, Anisimov et al [22] proposed a model to elucidate how this rate of energy exchange impacts the laser heating of metals. This assumption led to further refinements of the equation, resulting in the Parabolic Two-Step (PTS) model, which is nowadays recognised as the Two-Temperature Model (TTM).

The TTM, governing the interplay between electron and lattice temperatures in a non-equilibrium state, played a significant role in the examination of short-pulsed laser mirrors, as investigated by Qiu et al [23] in a separate experiment in 1994. Typically, the thermal design of gold-plated mirrors for high-power lasers is rooted in Fourier's heat conduction model, where a secondary material with higher heat diffusivity serves to disperse heat away from the reflective surface, minimising the risk of thermal damage. However, in the context of short-pulsed laser systems, this concept becomes irrelevant because, at shorter timescales, Fourier's heat conduction model no longer holds true and the absorbed energy cannot efficiently propagate into the bulk material [24]. To address this challenge, a proposed solution involved the multi-layer coating of the mirror's surface. In this configuration, the lower layer material, chromium in this case, exhibits a higher electron-lattice transfer rate than gold. Consequently, it efficiently converts most of the absorbed radiation energy by free electrons into lattice energy, redirecting it away from the reflective surface.

This study marked an early attempt at simulating the interactions of short-pulsed lasers with metals, ultimately leading to further refinement of the modified Fourier’s heat conduction equation for this specific context. To address the intricacies of high-intensity, short-duration irradiation energy transfer within molecular systems, a new equation was introduced known as the Hyperbolic Two-Step (HTS) model. HTS currently serves as the preferred method for simulating interactions between high-intensity, femtosecond pulsed lasers interaction with metals. However, it transitions into a PTS model when the pulse duration exceeds the electron relaxation time, typically exceeding 10 picoseconds. The HOS model is applicable to lower intensities and in cases involving slower heating processes, it can be simplified to the POS model. Figure 2.2 provides an illustrative representation of the heat transfer process during laser-matter interaction, outlining the interrelationships between these various models, as explained by Marla et al [9] and Qiu et al [23].

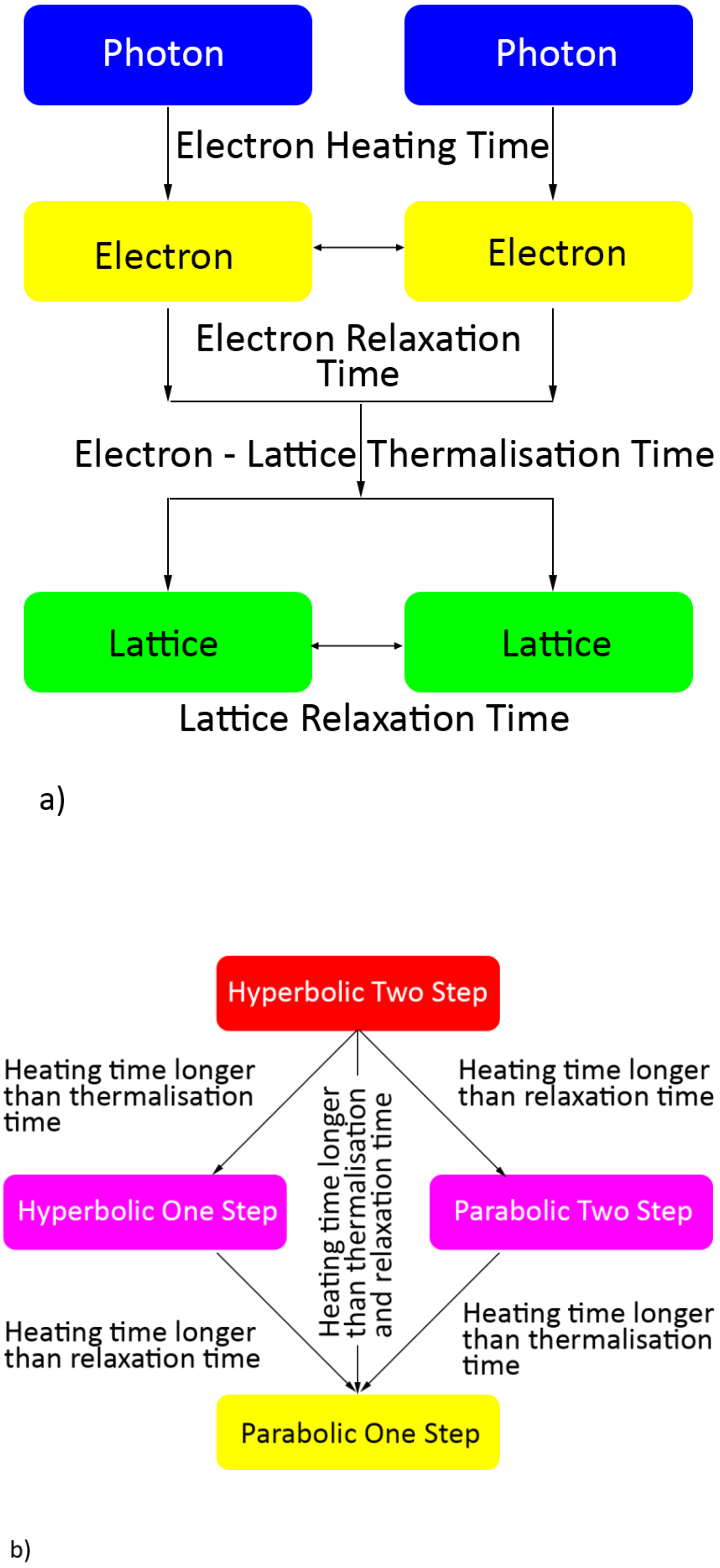

Figure 2.2 – a) Microscopic interaction during the heat transfer process. b) Interrelationship between heat transfer models [9,23].

In 1996, Chichkov et al [25] conducted a semi-empirical study to explore the impact of pulse duration, ranging from nanoseconds to picoseconds and femtoseconds, on the quality of drilled holes' edges and the presence of burrs on the surface after ablation. Their investigation included mathematical modelling, following the same principles as previously explained, and employing models based on thermalisation and relaxation times. However, this study did not present calculation results to validate the derived formulae. Nonetheless, Chichkov and colleagues conducted experiments utilising various metals and a thick silicon target while adjusting the laser fluence and pulse frequency to achieve consistent drilled depths. Their observations indicated that in femtosecond material processing, the liquid phase is notably absent and heat conduction to the surrounding areas is negligible. Additionally, they concluded that vapor and plasma phases exhibit rapid behaviour during femtosecond laser pulses, resulting in sharp and well-defined patterns. This characteristic makes femtosecond pulsed lasers a promising tool for precise material processing. Research in this field continues to evolve, with recent efforts benefiting from these analytical approaches [24].

2.3. Physical mechanisms during ultrashort pulsed laser ablation

In 2001, Ye et al [26] conducted a comparative study between picosecond and femtosecond pulsed laser ablation of titanium in vacuum. They employed time-of-flight and emission spectroscopy techniques to measure the velocities of ions ejected from the surface during the ablation process and related it to the resulting crater depths. Their measurements revealed that the ejecta produced by 80 fs laser at a wavelength of λ=800 nm carried more kinetic energy compared to particles ablated by picosecond pulses with identical wavelength. This observation aligned with the findings from MD simulations conducted by Zhigilei et al [27], which concluded that ejecting velocity is linearly related to the initial position of atoms within the substrate's skin layer. This relationship can be described by a modified Maxwell-Boltzmann distribution to account for a range of stream velocities.

Furthermore, Ye et al [26] proposed that the radiation absorption in metals involves not only free electrons excited by Inverse Bremsstrahlung (IB) absorption but also bound electrons. In simpler terms, photoionisation elevates bound electrons to the free electron level and multiphoton ionisation becomes more predominant at relatively higher laser intensities. The researchers also observed that the size of ejection clusters is proportional to the laser fluence. Additionally, they noted that the craters produced by 1000 pulses of the femtosecond laser were cleaner and smoother compared to those created by an equivalent number of picosecond laser pulses. This feature highlighted the advantages of femtosecond pulsed lasers for ultra-precision machining. This study argued that for picosecond and longer laser pulses, the ablation depth is primarily influenced by thermal diffusion. In contrast, for femtosecond laser pulses, the dominant factors are the optical penetration depth and electronic heat conduction.

These studies delved into mechanisms crucial to Pulsed Laser Deposition (PLD), where the ablated nanoparticles find utility in various applications. Close attention was paid to the ablation rate and cluster size in pursuit of process improvement. A notable challenge encountered here was the formation of a plasma plume above the surface, which interacted with the incoming laser beam, diminishing its efficacy. However, within the realm of ultra-precision manufacturing, the focus shifts to the ablated surface, culminating in a process known as direct laser writing. Hirayama and Obara [28] conducted a series of ablation experiments on surfaces of gold, silver, copper and iron using a Ti:sapphire femtosecond pulsed laser. They reported the emergence of an amorphous metal layer in the region ablated by the femtosecond laser. According to their findings, the residual beam energy not contributing to the ablation process instigates the formation of a thin melt-phase layer, which is rapidly cooled before recrystallisation occurs. The authors also referred to a simulation study that seemingly documented the creation of the melted layer at the ablation site. However, they did not expand further into the underlying factors responsible for this phenomenon or potential solutions in cases where the formation of an amorphous metallic layer is an undesirable outcome. These experiments were conducted in an ambient environment at room temperature.

In 2004, Rethfeld et al [29] reiterated that the steps involved in USP laser ablation occur at distinct temporal intervals, each amenable to individual study. They arrived at the conclusion that the solid's excitation transpires while the laser beam is directed at the target. Subsequently, subject to the intensity of the excitation, the material undergoes a phase change into a molten state within the picosecond timeframe. The material's ultimate state post-irradiation, they noted, is contingent upon laser properties such as intensity and wavelength, in addition to material-specific characteristics.

In a contemporaneous study, Feng et al [30] employed a femtosecond pulsed Ti:sapphire laser to create microholes in a single-crystal superalloy, both with and without plasma-sprayed thermal barrier coating. These microscale holes served the purpose of air cooling aero-engines, where engine failure can have catastrophic consequences. Their primary objective was to scrutinise potential defects that might arise from laser drilling. Examination via Scanning Electron Microscopy (SEM) revealed that within the machining area, there was no evidence of melting, HAZ, recast layers or microcracks. The only reported form of damage was a laser-induced, plastically deformed layer approximately 5 microns thick when the fluence reached or slightly exceeded the ablation threshold. It is worth noting that these experiments were conducted in ambient air at room temperature. The superalloys used in these experiments had an ablation threshold of 203 ± 20 mJ/cm², and the laser fluence ranged from 0.1 J/cm² to 160 J/cm². This investigation concluded that femtosecond micromachining holds promise as a method for consistent, damage-minimised production of microscale features in high-volume manufacturing processes involving multi-layered turbine aerofoil and combustor materials.

In 2005, Grojo and Hermann [31] investigated femtosecond laser ablation, targeting titanium, zirconium and hafnium. Their approach involved time-of-flight observations and rapid imaging techniques. They directly witnessed the ablated plasma plumes at nanosecond timescales and made a noteworthy discovery: the kinetic energy of the nanoparticles within the plume remained unaffected by changes in laser fluence. This finding led them to conclude that the energy initially absorbed by electrons must undergo redistribution within the electronic subsystem before reaching the lattice. Moreover, their experiments shed light on the characteristics of the plasma plume and they proposed that electrostatic phenomena like Coulomb Explosion or space-charge acceleration were unlikely contributors to the mechanisms underlying USP laser ablation. These mechanisms, if present, would have resulted in an increase in the kinetic energy of ablated particles. Another significant observation made in their study pertained to the relationship between the size of ablated clusters and the atomic mass of the material. They reported that materials composed of lighter atoms produced larger ablated clusters.

In a more recent study, Tanaka and Tsuneyuki [32] also challenged the presence of Coulomb Explosion in USP laser ablation of metals. In this comparative analysis of the mechanisms underlying USP laser ablation in semiconductors and metals, they argued the significance of including the electronic entropy in this context, emphasising that it offers a more comprehensive understanding of energy conservation in MD simulations of laser ablation on metallic surfaces.

2.4. Development of molecular dynamics simulations

Modelling serves as a valuable tool to comprehend processes that are either imperceptible to the naked eye or impractical to explore through cost-effective experimental setups. In recent years, modelling has evolved into a computational tool for design and prediction, alongside its role as an investigative tool [33]. Ciccotti et al [34] referred to molecular simulations as computational statistical mechanics in a comprehensive review of developments in MD simulations, dating back to 1950s. Utilising the fundamental law of energy conservation and Newton's second law, which states that force is the product of mass and acceleration ($F = ma$), MD simulations statistically predict the positions and velocities of individual atoms within a system at discrete time intervals. By numerically solving equations of motion for each atom, MD simulations provide insights into the dynamic behaviour of molecules, outputting information about the structural and thermodynamic properties of complex systems over a wide range of spatial and temporal scales.

MD simulation of laser ablation was first introduced by Cleveland et al [35] in pioneering research on laser annealing in 1982. This work laid the foundation for subsequent studies, including that of Yamashita et al [36] in 2006, which marked the first instance of USP laser ablation simulation. Yamashita et al [36] adopted the TTM, which had been developed in previous decades, and integrated it into conventional MD simulations, coining the term "modified molecular dynamics" (MMD). While acknowledging that heat transport mechanisms had wave-like characteristics, they emphasised the importance of considering electronic heat capacity and conductivity as temperature-dependent factors in predicting laser-matter interactions. Implementing these variables as temperature-dependent proved challenging, so they simplified the simulations by assuming fixed values for these parameters. The results of their simulations suggested that in metals (aluminium in this case), the heat transport mechanism is initially dominated by electron heat conduction. Within a few picoseconds, temperature variations became apparent. Yamashita et al [36] attributed these temperature gradients to the propagation of a thermal shock wave, which persisted until equilibrium was achieved. Subsequently, lattice vibrations took over as the primary mode of energy transport at longer timescales.

Following the rapid advancement and increased accessibility of faster and more powerful computers in the early 2000s, MD simulations emerged as a preferred method for gaining insights into the intricate processes occurring during USP laser interactions with materials. The well-documented advantages of MD simulations over the Finite Elements method (FE) further solidified its appeal [33]. Consequently, MD simulation-based studies garnered significant research interest and played a pivotal role in advancing the field to its current state. In 2006, Chen et al [37] introduced additional terms, namely electron drifting velocity and electron kinetic pressure, into the equation of energy balance within the electronic subsystem. This enhancement aimed to better account for the effects of the electric field during laser-material interactions. Through a numerical analysis involving ablating gold films, they compared the phenomenological TTM with the more recently developed semiclassical TTM. Their findings suggested that these models exhibit different thermal responses, with the damage fluence threshold obtained from the semiclassical simulations aligning more closely with experimental data. This refinement of the energy transfer equation has since been incorporated into simulation software, including LAMMPS (https://lammps.sandia.gov).

To enhance the efficiency of MD simulations in recent years, Zhou et al [38] streamlined the ablation process by simplifying it to 1D rods aligned with the direction of laser irradiation, employing a Gaussian distribution. By extrapolating these segments, they contended that their model effectively captured the phenomenon and the results can represent the system at the micron scale.

2.5. Applications of ultrashort pulsed laser ablation

Around 2007, after nearly two decades of dedicated exploration into the physics of energy transfer at short timescales and the fabrication of functional surfaces using USP lasers, its applications began to transition into commercial testing. An early-stage demonstration came from the experiments conducted by Tsukamoto et al [39] using a femtosecond pulsed laser, with the aim of fabricating cone-like protrusions on titanium plates for potential clinical orthopaedic applications. Employing an average fluence of 0.75 J/cm^2 (the ablation fluence for pure titanium being approximately 0.1021 J/cm^2 [40]), and employing various pulse frequencies, they successfully generated periodic microstructures on the surface. They noted that these features were oriented parallel to the laser's polarisation vector and that their size increased as bridging structures formed between adjacent protrusions.

Remarkably, in the same year, Vorobyev and Guo [41] claimed to have achieved the first femtosecond pulsed laser surface treatment of titanium intended for biomedical implants. This subtle assertion of rivalry underscored the potential impact of successfully executing this process. In contrast to the aforementioned work, Vorobyev and Guo [41] deliberately kept the laser fluence below the ablation threshold, maintaining it at around 0.067 J/cm^2. This approach resulted in the creation of periodic patterns on the order of about 20 nanometres. This method provides a degree of control over the produced periodicity and feature sizes and is now recognised as Laser-Induced Periodic Surface Structuring (LIPSS).

Nayak et al [42] studied the role of ambient gases in USP laser treatments applied to titanium and silicon. They documented their pioneering achievement in creating a regular array of sharp nanostructures atop cone-shaped microstructures (referred to as hierarchical structures) for the first time under vacuum conditions and in a helium ambient environment at 100 mbar pressure. Their experiments revealed intriguing findings. In their investigations, Nayak and colleagues observed that during the initial irradiation of silicon, the periodicity of the ripples closely matched the wavelength of the laser beam. This stood in contrast to the behaviour witnessed during titanium treatment, where the periodicity underwent alterations as the pillars formed. Another noteworthy observation was that the features produced in a vacuum exhibited sharper characteristics, and the height of the resulting pillars favoured lower ambient gas pressures. The precise mechanism underlying this phenomenon remained elusive, prompting the authors to emphasise the need for further exploration and investigation.

In a keynote paper, Bruzzone et al [3] highlighted the significance of engineered surfaces, establishing a vital connection between the mechanical and optical properties of surfaces and their application in high-impact fields such as bioengineering. However, they also concluded that the metrology of engineered surfaces represented a critical area requiring attention to support the widespread adoption of new applications. This underscored the profound importance of computer simulations, which inherently offer accurate metrological insights, within the realm of nanostructures and engineered surfaces.

In the year 2008, Lin et al [43] embarked on a comprehensive study involving first-principle calculations focusing on eight representative metals: Al, Cu, Ag, Au, Ni, Pt, W and Ti, all under the influence of strong nonequilibrium conditions characterised by varying temperatures between electrons and phonons. Their primary objective was to scrutinise the assumptions underpinning computer simulations, specifically the notions of a linear temperature-dependent electron heat capacity and a constant electron-phonon coupling factor, with the aim of enhancing simulation accuracy. Their findings unveiled a nuanced picture of electron-phonon coupling's behaviour in response to temperature fluctuations. Importantly, not all materials exhibited identical responses to these changes. In the cases of Al, Au, Ag, Cu and W, the coupling strength intensified as electron temperature increased, while Ni and Pt displayed a weakening of the coupling. Titanium, on the other hand exhibited nonmonotonic behaviour. The study argued that at elevated electron temperatures, there is a significant contribution from electrons below the Fermi level, whose involvement in electron-phonon energy exchange necessitates their inclusion in the quantitative analysis of this process.

However, it was noted that in situations characterised by low laser intensities, assuming a constant electron-phonon coupling factor did not substantially influence the outcomes of two-temperature calculations, as suggested by experimental evidence. Consequently, based on these ab-initio calculations, the researchers concluded that assuming a linear temperature dependency for electron heat capacity was not an appropriate assumption. Yet, the study did not propose a definitive solution for integrating these findings into MD simulations.

In 2009, Lewis and Perez [44] unveiled the results of their MD simulations, shedding light on what they perceived as the underlying mechanisms at play in the process of USP laser ablation in materials with strong absorbance properties. They summarised these mechanisms into distinct categories based on the absorbed energy: spallation, phase explosion, fragmentation and vaporisation. Notably, they introduced the fragmentation mechanism as the "breakdown of a uniform material into clusters due to the influence of high strain rates." Moreover, their research highlighted some noteworthy distinctions: spallation was found to be a phenomenon unique to femtosecond pulses, while phase explosion did not manifest under ultrashort pulses. Drawing on this classification, the researchers postulated that a laser beam with a variable intensity distribution, such as a Gaussian distribution, could trigger a combination of these mechanisms simultaneously, contingent upon the effective energy absorbed by the target material, essentially, the local energy density imparted by the laser pulse. It is important to note that these simulations were conducted on a hypothetical 2D material with reduced potentials (Lennard-Jones); however, the researchers contended that their explanations primarily applied to the thermal regime. They acknowledged that comprehending the non-thermal regime represented a formidable challenge ahead.

Around the same time, Zhigilei et al [45] conducted in-depth investigations into the effects of varying output power of USP lasers on the ablation processes of nickel, utilising atomistic simulations. Their findings elucidated a significant shift in the ablation rate observed in experimental data, signifying the transition from normal vaporisation to phase explosion. Their explanation revolved around the rapid deposition of energy during short-pulse irradiation, resulting in a swift temperature surge and the potential generation of compressive stresses. These compressive stresses then transformed into tensile stresses upon interaction with the material's free surfaces. When these tensile stresses reached a critical magnitude, they induced mechanical fractures within the solid material. The subsequent relaxation of these laser-induced stresses led to the ejection of substantial solid particles or liquid droplets, a phenomenon known as spallation or photomechanical ablation.

Remarkably, Zhigilei and colleagues asserted that their simulations revealed an abrupt transition from spallation to phase explosion, in contrast to the findings of their previously mentioned study. Their work proposed a complex interplay among melting, spallation and phase explosion, all occurring simultaneously, with their relative proportions dictated by the laser fluence. They stressed that this transition from one dominant mechanism to another transpired suddenly at specific laser fluence levels. Notably, their calculations assumed a constant electron-phonon coupling factor and the authors acknowledged that certain quantitative predictions, such as fluence thresholds for melting and spallation might be influenced by this assumption. However, they maintained that the qualitative physical framework remained valid, despite the evolving understanding of the temperature dependency of this variable.

By the year 2010, MD simulations were widely used to model the USP laser ablation process. Inogamov et al [46] reported that electron collisions had a marginal impact on light absorption in solid aluminum. They used MD simulations to delve into the kinetics of aluminum crystal melting over a time preiod of 0 to 4 ps, thus explaining the behaviour of their probes. In a similar effort, Seydoux-Guillaume et al [47] also used MD simulations to study the propagation of shock waves into the interior of monazite with a particular focus on the formation of defects. They observed that the USP laser irradiation primarily induced mechanical defects, overshadowing thermal ones. Furthermore, Fang et al [48] conducted a series of calculations based on the two-temperature model, manipulating the fluence of USP lasers to discern the effects of temperature gradients on electronic properties. The researchers contended that the electronic collisions played a pivotal role in this process, influencing electronic properties significantly. They concluded that their findings aligned with the experimental data and emphasised the importance of considering temperature-dependent factors such as electronic heat capacity, thermal conductivity, absorption coefficient and absorptivity. Subsequently, they integrated their proposition into the two-temperature model, presenting an updated version in their paper.

Leitz et al [49] also argued that phase explosion stands as one of the predominant mechanisms within the realm of USP laser ablation. They supported their assertion with empirical evidence, contrasting the outcomes of ablated substrates across various laser pulse durations, including micro, nano, pico and femtoseconds. Moreover, they underscored the practical implications from a manufacturing perspective, highlighting that the choice of laser pulse duration entails trade-offs between precision and efficiency. Specifically, they noted that longer pulses result in higher ablation rates whereas shorter pulses yield enhanced resolution. Figure 3.2 provides SEM images that visually substantiate their conclusion.

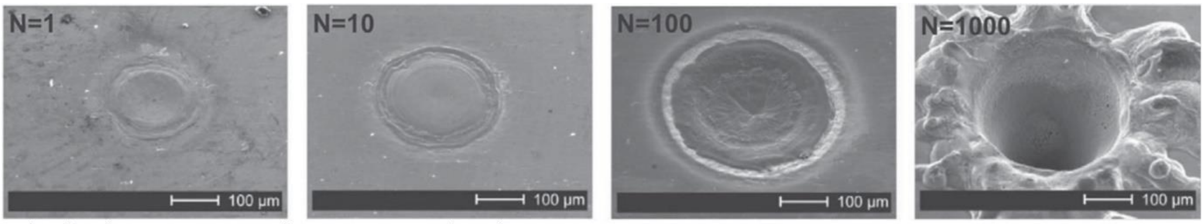

a) pulse duration 80 ms with 1064 nm wavelength

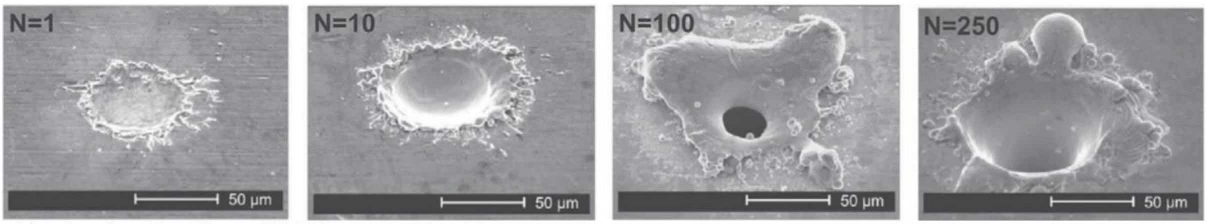

b) pulse duration 60 ns with 532 nm wavelength

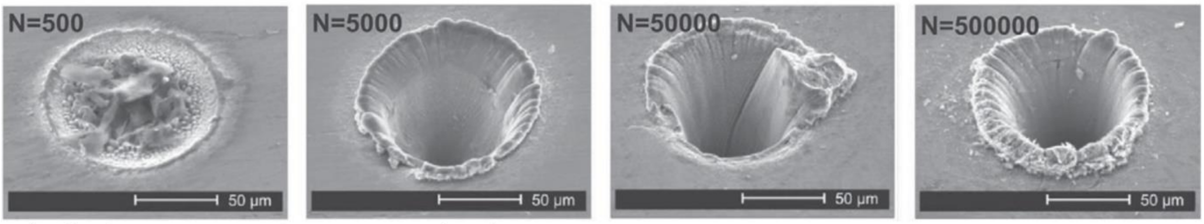

c) pulse duration 10 ps with 1064 nm wavelength

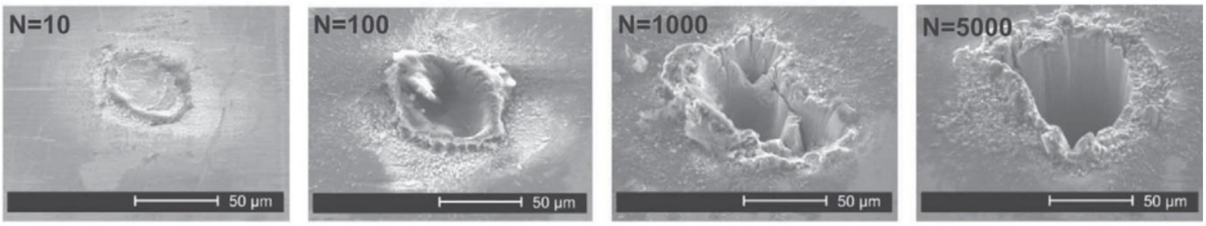

d) pulse duration 170 fs with 800 nm wavelength

Figure 2.3. Side by side comparison of ablation site in ms, ns, ps and fs pulse durations. N represents the number of pulses. (a) pulse duration 80 ms with 1064 nm wavelength, (b) pulse duration 60 ns with 532 nm wavelength, (c) pulse duration 10 ps with 1064 wavelength, and (d) pulse duration 170 fs with 800 nm wavelength [49].

Building upon the sustained efforts of the scientific community to gain deeper insights into the physics of USP laser ablation, practical applications of this technology began to emerge in the early 2010s. These developments were facilitated by advancements in laser generation technology, precise beam delivery and positioning, the production of modern optical materials and increased accessibility to cost-effective laser machines. Fadeeva et al [1] successfully fabricated a superhydrophobic surface on titanium, aiming to explore the bacteriostatic effects of the hierarchical nanostructures they generated. They employed a self-structuring technique induced by femtosecond lasers, known as LIPSS to attain a high degree of superhydrophobicity. However, it is important to note that the fabricated geometries were not optimised for repelling bacteria and their observations revealed intermittent repulsion where certain tested microorganisms managed to colonise the surface. The researchers suggested that the mechanical attachment of bacteria to the surface might have contributed to the observed limitation in achieving the desired effect.

In a separate study, Nicolodelli et al [50] investigated the femtosecond laser ablation of hard tissues, specifically dental and femur samples, to analyse the morphological characteristics of the ablated surfaces. To accurately determine the ablation threshold conditions, they faced the challenge of incorporating the Gaussian distribution of laser intensity into their calculations, as deriving values directly from the beam spot size led to inaccuracies. Their findings revealed that the morphology of the resulting cavity after femtosecond pulses was strongly influenced by the number of pulses. Importantly, even at relatively high fluences, no secondary effects of mechanical or thermal damage were observed. The researchers argued that femtosecond pulsed lasers represented suitable tools for cutting, removing and modifying the surfaces of human dentin and femur bones without causing collateral damage.

2.6. Manufacturing techniques utilising USP laser ablation

The potential impact of USP laser processing on materials has spurred the development of various innovative techniques to harness its unique capabilities. One such example involves leveraging the nonlinear effect of high-power pulses, known as Kerr self-focusing to guide the laser beam through filamentation. Valenzuela et al [51] conducted a comparative study on the ablation of steel and titanium using this technique versus sharply focused laser pulses. They deduced that when a well-defined and precise cut is the objective, short focal length lenses outperform filaments. However, for certain applications, the ability of filaments to ablate materials over extended distances (ranging from 10 to 100 meters) with minimal beam divergence can be indispensable.

Another instance of innovative exploitation of the properties of USP lasers emerged in 2015, courtesy of Vorobyev and Guo [52]. Through an undisclosed technique, they successfully engineered hierarchical micro and nanostructures on surfaces of titanium (50 µm deep microgrooves), platinum (75 µm deep microgrooves) and brass (10 µm deep microgrooves), all of which exhibited remarkable mechanical and optical properties. Figure 2.4 presents a sequence from their demonstration video, showcasing the superhydrophobicity of processed platinum surface at a tilt angle of 8°. The researchers claimed that these multifunctional surfaces possess the capability to self-clean while also manifesting all the desired attributes associated with superhydrophobicity, such as anti-corrosion, anti-icing, anti-biofouling and more. Furthermore, these surfaces exhibited significantly enhanced broadband light absorption capabilities.

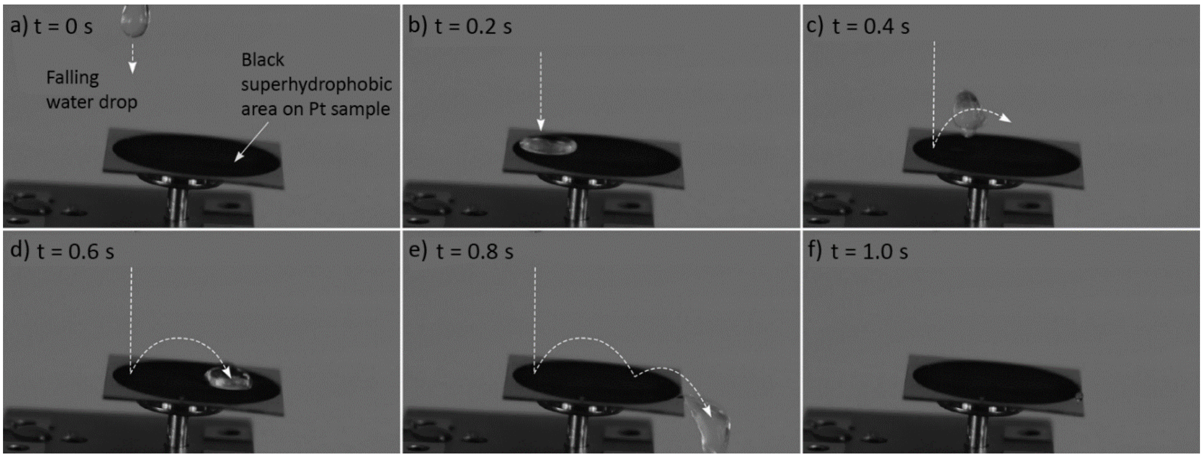

Figure 2.4 – Sequence of snapshots showing superhydrophobicity possessed by the Pt sample at, (a) t = 0 s, (b) t = 0.2 s, (c) t = 0.4 s, (d) t = 0.6 s, (e) t = 0.8 s, (f) t = 1 s [52].

In recent years, there has also been active research in exploring the effects of ablated particles and plasma plume on the surrounding environment in the immediate aftermath of the ablation, contributing to the growth of knowledge in this matter. Zhang et al [53] conducted a study to examine the propagation of shockwaves generated during the ablation process. They identified two distinct types of cylindrical waves generated as a result of air breakdown, which involves the ejection of electrons from the surface and plasma expansion and phase explosion. In their experiments involving the ablation of aluminium using a femtosecond pulsed laser, they meticulously recorded the precise formation and propagation times of shockwaves at the picosecond and nanosecond scales. Their findings led them to conclude that the expansion of the plasma plume occurs in a cylindrical shape, in contrast to the previously reported hemispherical geometry.

In a further endeavour to refine and enhance the theoretical framework, Rethfeld et al [54] published a review paper in 2017, building upon their earlier work from 2004 [29]. They brought attention to several critical issues stemming from assumptions made when modelling USP laser ablation processes. First and foremost, they challenged the accuracy of applying the concept of temperature in nonequilibrium conditions as temperature is inherently linked to an equilibrium energy distribution. Next, they raised concerns about the classical Fourier law, asserting that it remains valid only when timescales exceed the mean free path of energy carriers (electrons). Rethfeld et al also emphasised the dynamic nature of lattice parameters during phase transitions. They also highlighted a potential problem with assuming equilibrium conditions for the electronic subsystem. They argued that electrons can exist in nonequilibrium states relative to other electrons, giving rise to the possibility of multiple electron-phonon coupling factors operating simultaneously. Moreover, the researchers postulated that the penetration depth of USP laser beams could surpass the expected optical penetration depth due to the ballistic movement of electrons. This contradicted the claim made by Gamaly and Rode [55], who argued that energy transport by electrons in USP laser ablation processes should not be treated as ballistic. It is worth noting that Rethfeld et al [54] did not quantify the precise impact of these issues on the outcomes of current simulations, leaving open questions regarding the extent of their influence.

Suslova and Hassanein [56] advanced the argument that assuming constant optical properties of materials throughout the simulations is an inaccurate approach. Drawing inspiration from Lin et al's model [43], which incorporated the electron density of states to account for the effects of electrons below the Fermi level in high-intensity pulses, they developed a two-temperature code named FEMTO-2D for two-dimensional materials based on collision theory. Their aim was to achieve a more precise representation of the temperature-dependent electronic properties. With this innovative approach, they studied the reflectivity and absorptivity of metals as a function of electronic temperature. Employing a Gaussian beam profile in their simulations, they analysed how materials exhibited simultaneous temperature gradients. Their findings revealed a consistent initial rise in nickel's reflectivity at the outset of the pulse, followed by a sharp decline mirroring the behaviour observed in other metals they examined. However, the underlying reason for this trend remained unclear. They speculated that it might stem from the rapid shift in the material's plasma frequency in comparison to the effective collision frequency. Furthermore, by simulating a range of laser fluences, they concluded that temperature fluctuations did lead to changes in the optical penetration depth but did not exert a significant impact on the overall simulations.

In the year 2018, Žemaitis et al [57] introduced a novel model designed to represent the ablation of a rectangular cavity. Their research delved into the realm of multi-pulse ablation. In their study, they took into account two key observations: the decrease in ablation threshold and the saturation of ablation depth, both of which were noted with an increase in pulse frequency. Additionally, the researchers factored in the Gaussian distribution of laser intensity, which enabled them to mathematically describe the relationship between the peak laser fluence at the centre of the beam and the diameter of the resultant crater. They put forward the proposition that the most efficient ablation occurs when the peak fluence is e^2 times greater than the threshold fluence. In a parallel effort, Abdelmalek et al [58] investigated the ablation of copper using a burst of femtosecond laser pulses. They maintained the pulse interval shorter than the electron relaxation time while varying both the laser fluence and the number of pulses. Their findings suggested that increasing the number of pulses enhanced the vaporisation rate in comparison to a single pulse with the same accumulated fluence. Consequently, they posited that rapid bursts of femtosecond laser irradiation could be harnessed for a cleaner and more efficient ablation of metals.

2.7. Recent developments in ultrashort pulsed laser ablation research

In their study, Dong et al [59] conducted an analysis of the effects associated with the movement of the laser focus in ultrashort multi-pulse laser ablation, with the specific application of helical drilling of metals in mind. They employed simulations to represent a scenario where the laser focus descended at a constant speed. Notably, they emphasised the pivotal role played by pulse intervals in this method, suggesting that a higher pulse frequency led to elevated electron and lattice temperatures. However, this increase did not significantly augment the ablation depth, eventually reaching a saturation point. The researchers also argued that there exists an optimal velocity for the downward movement of the laser focus. They observed that rapid and slow movements led to negative and positive defocusing, respectively. Their conclusion for copper, the material under examination, was that maximum efficiency was attained when defocusing remained below 50 nm. Nevertheless, they acknowledged that the ablation depth values they obtained for copper did not align with previously published data in the literature.

In another endeavour aimed at enhancing simulations of nonequilibrium systems in 2019, Ullah and Ponga [60] introduced a novel approach. They replaced Fourier's heat conduction equation with the Fokker-Planck equation to capture local electronic temperature more accurately. They asserted that their method could replicate complex geometries and offered the advantage of easy integration with classical molecular dynamics codes, as it did not necessitate auxiliary mesh structures. The researchers announced their successful integration of this method with the LAMMPS open-source code. However, the superior performance of their proposal in comparison to current methods awaits comprehensive evaluation and review.

In 2020, Michalek et al [61] embarked on an investigation into USP laser structuring of freeform surfaces. They focused their efforts on addressing some of the limitations associated with freeform surface structuring within the context of LIPSS, a surface structuring method that has gained popularity and matured sufficiently for certain commercial applications. LIPSS leverages the Gaussian beam profile to create periodic features by strategically aligning the high and low-intensity regions of the laser beam while systematically scanning the target surface. It is well-established that laser fluence directly impacts the depth of ripples, while factors such as beam incident angle, wavelength and polarisation vector influence the periodicity and orientation of the features. However, when scanning a freeform surface, the most prominent factors become the beam incident angle and the focal offset distance.

Using theoretical modelling, Michalek and colleagues made predictions about the material's response based on varying laser parameters. They proposed an optimised configuration by manipulating the process setup, a configuration subsequently validated through experimentation. Nevertheless, their simulations indicated that groove formation might necessitate a hydrodynamic effect or pre-existing subwavelength-sized ripples in conjunction with the laser beam, as argued by Stratakis et al [6]. In a more technical explanation, Bonse et al [62] asserted that electromagnetic scattering played a significant role in LIPSS, while an ongoing debate persisted concerning whether the Marangoni or Rayleigh-Taylor instability dominated during the reorganisation of matter in the hydrodynamic relaxation stage. Tsibidis et al [63] introduced crystallographic orientation and interpulse delay time as additional factors influencing surface pattern formation, contending that these variables impact carrier dynamics and the thermal response of the target material.

The evolution of research in the realm of laser technology, as observed in the literature, can be categorised into several overarching trends. In the early stages of laser technology development, extending until the early 1990s, the primary focus within the scientific community was on creating increasingly powerful and shorter pulsed lasers. During this period, researchers closely observed the interactions between light and matter under extreme conditions. Following the achievement of femtosecond pulses with exceptionally high power delivery, attention shifted towards gaining a deeper understanding of the physics governing these interactions in order to harness their potential. This trend persisted until the mid-2000s. Notably, the majority of studies during this period relied heavily on experiments, with mathematical modelling employed to elucidate the underlying processes.

Around the early 2000s, the introduction of more powerful computers marked a significant development. These computational tools provided an atomistic means to gain enhanced insights into these interactions by visually representing the proposed theories. Beginning around 2005, as knowledge of physics involved in USP laser interactions continued to grow, and access to laser machines and metrology equipment became more widespread, the development of simulation frameworks and applications for USP laser-matter interactions accelerated. It is evident from the literature that computer simulations played a pivotal role in propelling the field forward and contributed significantly to the identification of valuable applications, a trend that persisted until approximately 2015. The discovery of high-impact applications for this technology garnered substantial interest and focus of further research in this area. The sheer volume of scientific publications in recent years serves as compelling evidence of this trend and as articulated by Bonse et al [62], "…the investigation [of surface structuring with USP lasers] has developed into a scientific evergreen".

Ijaola et al [64] conducted a review focusing on the techniques for creating functional biosurfaces and explored the impact of ambient conditions on surfaces treated by lasers. They particularly highlighted a transition in wettability, shifting from superhydrophilic to superhydrophobic when the surface was exposed to air and organic contaminants. Their conclusion was that the presence of carbon on a treated titanium surface heightened its hydrophobic properties. Mukharamova et al [65] employed experimental methods, utilising IR pump – X-ray probing, to examine the influence of periodic plasma generated by femtosecond pulsed lasers, a phenomenon known as the skin effect. They also studied the effects of propagating shockwaves on surface structures. The skin effect was noted to reduce the efficiency of the process. Their findings revealed that the shockwave propagation occurred more rapidly in periodic structures. These shockwaves however, disrupted the periodic formation of structures briefly before transforming into non-destructive acoustic waves. Nevertheless, no proposed solutions for removing the plasma plume from the vicinity of the beam spot area to enhance process efficiency have emerged in the literature thus far.

Inogamov et al [66] recently revisited the heat propagation within materials, suggesting that heat transfers at supersonic velocities from the skin layer (the optical penetration depth) into the bulk material. In their simulations, they explored the effects of using water as the ambient medium. They elaborated on the relationship between the expansion of a heated target in the ablation process when confined by a dense water medium and compared it to the identical process in a vacuum. Their simulation results indicated that the maximum pressure existed at the medium-target interface longer than the period when the maximum laser intensity was present.

Mazhukin et al [67] proposed that ultrafast irradiation gives rise to a strong electric field on the incident spot area due to the electronic pressure of collectivised electrons near the surface. They asserted that the primary divergence between the double electric layer (metal surface) approach and drift-diffusion calculations lies in the region of the electron pressure gradient and the electric field in each method. Their argument was that electron pressure serves as the primary catalyst for phase explosion in a nonequilibrium regime, as opposed to phase change in an equilibrium condition. Instead of employing the conventional Euler and Lagrangian methods, they opted for an arbitrary non-stationary coordinate system, as they believed it was more useful for calculating discontinuous solutions such as shockwaves.

In a recent study, Bucă et al [68] introduced a new approach to simulations, asserting that it offers computational advantages compared to the currently employed version. The customary method for simulating femtosecond pulsed laser-matter interactions involves using quantum theories to describe energy absorption and then solving heat equations with classical Fourier's heat equation. In their publication, the authors explored an alternative approach, initially treating the interaction classically and subsequently solving the heat equation with quantum operators (the Cattaneo-Vernote equation). They conducted simulations by adjusting the coupling factor and relaxation time, concluding that a lower coupling factor and/or a higher electron relaxation time led to higher electron temperatures due to slower heat transfer to the lattice. Their simulations involved the ablation of a gold surface and while their results did not contradict previously established knowledge, the potential advantages, disadvantages and specific applications of their model await further examination and evaluation.

With the continual advancement of simulation frameworks, researchers are increasingly leveraging MD simulations to validate or refine existing theories and assumptions. Xie et al [69] conducted simulations involving the ablation of a copper film and investigated the influence of pulse duration on the process. Their work confirmed that lattice temperature impacts the electron-phonon coupling factor. They observed that pulses of 100 fs, 200 fs, and 500 fs, led to surface disintegration, melting and vibration and only surface vibration respectively. Wang et al [70] also employed

MD simulations to examine the ablation of a titanium thin film using pulses of 100 fs, 300 fs and 500 fs. Their findings indicated that spallation occurred more rapidly with shorter pulse durations. Furthermore, their results suggested that the electron-lattice coupling time was affected by pulse duration while the equilibrium temperature remained constant. Consequently, for shorter pulses, more energy was absorbed by the electrons at the bottom of the titanium film. Pan et al [71] harnessed MD simulations to validate the change in absorptivity of molybdenum disulfide in relation to laser fluence, corroborating experimental findings. Meanwhile, Zhang et al [11] employed MD simulations to investigate the femtosecond laser ablation of a nickel-aluminium alloy for the purpose of drilling air cooling holes in turbine blades. Their modelling, incorporating a Gaussian beam profile, revealed that for their selected fluence, phase explosion occurred solely at the centre of the spot with the highest intensity, while other regions experienced a combination of photomechanical spallation and melting.

In recent experimental investigations, Furukawa et al [72] explored the realm of double-pulse ablation (DP), with a primary focus on priming the material's response after the initial irradiation, often referred to as the "seed pulse" in order to enhance the ablation rate. It is well-established that the ablation rate correlates directly with laser fluence, and this study centred on exploring increased absorption rather than the accumulation of heat from multiple laser pulses. However, they observed an intriguing phenomenon termed "ablation suppression" occurring at approximately a 100-picosecond delay between pulses. They contended that this suppression was a transient occurrence limited to that specific time frame. To gain insights into this phenomenon, they conducted a comparative study between titanium and platinum. This choice was informed by the fact that the electron cooling time for platinum is approximately an order of magnitude longer than that for titanium. Theoretically, it is expected that ablation suppression in platinum to manifest at a later time compared to titanium due to the delayed diffusivity. Surprisingly, this was not the case in their study. Their work indicated that the seed pulse induced changes in surface properties beyond merely raising its temperature. During the period of ablation suppression, they noted an increase in surface reflectivity. In another study, Stratakis et al [6] conducted an assessment of various surface texturing techniques, encompassing LIPSS, DP irradiation, multi-beam interference patterning, among others. They proposed that high-precision surface manufacturing, offering optimal control over the shape, size and distribution of these structures, can be achieved through direct laser writing.

2.8. Summary

Achieving ultra-precision manufacturing and manipulating materials with nanoscale precision necessitates a high level of control over the laser ablation process. By attaining more deterministic outcomes that are economically viable, this technology can become accessible to a broader range of manufacturing capabilities. This, in turn, will expedite innovation in this field, leading to the development of new inventions and the creation of high-impact applications. As highlighted by numerous researchers discussed in this literature review, the primary obstacle hindering the transition of direct laser writing from scientific laboratories to manufacturing sites is the undesirable resolidification of material in the beam-affected zone, often referred to as thermal damage. This challenge requires further research, especially when the required resolution is in the nanoscale range. A more profound understanding of the mechanisms involved in USP laser-matter interactions will empower scientists to push the boundaries and gain deeper insights into this process. MD simulations show promise as a tool for further exploring the intricate process of USP laser ablation and numerous other related processes. Furthermore, MD simulations of ultrafast energy transfer in materials induced by external sources represent a less developed aspect of current available software. As argued in this literature review, this aspect plays a pivotal role in advancing USP laser ablation technology, ultimately leading to a more deterministic form of ultra-precision manufacturing.

In the subsequent chapters, more focused literature review sets the stage for an in-depth exploration of laser ablation applied to various grades of titanium. The discussion will extend to the critical examination of factors such as the influence of beam spot size, grain size and the manufacturing method of the material on the laser ablation process. Additionally, relevant examples drawn from the existing body of literature is discussed, offering a comprehensive understanding of the nuanced interactions and the size effects involved in the laser ablation of titanium across different grades and processing conditions.

Chapter 3 — Review of size effects in manufacturing

3.1. Introduction

In materials science and engineering "size effect" is attributed to a phenomenon where the mechanical, thermal, optical or electrical properties of a crystalline material changes as a function of its physical size where at least one dimension is in submicron length scale. This effect becomes stronger as materials are scaled down to a smaller size. The size effect is particularly relevant in nanomaterials and microstructures, where the ratio of volume-to-surface area becomes significant. Therefore, the geometry of a component is also a contributing factor in pronouncing the size effect when it is in submicron scale at least in one dimension. This is often referred to as "Hall-Petch strengthening". It is argued that it occurs because smaller grain sizes in polycrystalline materials result in fewer defects and dislocations that can move through the material, making it harder for deformation to occur. This added strength is often exploited for industrial use. For instance, it is widely acknowledged that the yield strength of metallic alloys can be enhanced by refining the grain size. In this context, the yield strength exhibits a proportional relationship with the inverse square root of the average grain diameter. This principle generally holds true for grains spanning sizes from millimetres to tens of nanometres.

In series of experiments carried out in Cavendish Laboratory, Cambridge UK in 1951, Hall [73] attempted to explain the size effect with the old grain boundary theory of Nadai (1924), Kuroda (1938) and “dislocation clogging” mechanism of Cottrell and Bilby (1949) by treating mild steel and observing its response in tensile tests. Since then, more sophisticated techniques and instruments have been developed to study mechanical properties of materials in submicron length scale [74,75,76]. In material mechanics, a commonly observed size effect is an increase in yield or flow strength as the submicron dimension of a specimen is reduced.

Conventional plasticity theory proves inadequate when attempting to explain the mechanical characteristics of metals under conditions where the size effect is prominent. For instance, this theory does not account for fracture mechanisms that involve atomic separation in the presence of plasticity. Generally, fracture related failure in metallic materials is ductile. However, there are instances where cleavage fractures occur during experiments, even in the presence of a substantial level of plastic flow. Intriguingly, these cleavage fractures often exhibit atomic decohesion, a phenomenon that demands tractive stresses on the order of the lattice strength (around 10 times of the materials' yield stress). For example, McMeeking [77] calculated the stress value ahead of a propagating crack to be around 3 times of the yield stress using finite element method. On the other hand, Reimantis et al [78] studied fracture propagation by experimentally analysing metal and ceramic interface (gold and sapphire) where they measured a larger fracture energy than what FE calculations suggested and they attributed this to the influence of plasticity. Nevertheless, the finite elements calculations based on the theory of plasticity show far lower values for stresses induced ahead of a propagating crack, warranting further research in this area.

It is argued that the plastic strain gradient of Geometrically Necessary Dislocations (GNDs) plays a crucial role in the size effect of this nature. The density of the GNDs scales with the gradient of plastic strain that can increase the flow strength in metals. Fleck et al [79] demonstrated the size effect in their experiments involving thin copper wires. Their findings revealed that when subjected to uniaxial tension, tensile stresses remained relatively insensitive to the wire diameter. Conversely, when exposed to torsion stress, wire diameters played a substantial role, with thinner wires exhibiting significantly greater strength compared to the thicker ones.

The proposed theories for incorporating the size effect into plasticity calculations [80,81,82,83] involve defining the flow stress or the plastic strain rate as functions of both plastic strength and plastic strain gradient ($\ell \nabla \varepsilon^p$) to include the length component as shown in the equations below:

$$a) \qquad \sigma_{flow} = \sigma_y \sqrt{f^2(\varepsilon^p) + \ell \nabla \varepsilon^p} \qquad b) \qquad \dot{E}_p = \sqrt{\frac{2}{3}(\dot{\varepsilon}^p)^2 + \ell^2 (\nabla \dot{\varepsilon}^p)^2} \qquad (3.1)$$

Where σ is stress, ε is strain, l is length, subtext 'y' denotes yield and 'p' stands for plasticity.

Tho et al [84] compared FE simulation results with experimental data obtained from indentation tests and they reported that the finite element solutions that employ classical plasticity theory significantly diverge from the experimental values. They found that this discrepancy becomes more pronounced as the indentation depth decreases. They argued that incorporating the conventional theory of mechanism-based strain gradient plasticity exhibit strong agreement with experimental results across all levels of maximum indentation depth (400 – 3400 nm). In a series of experiments, Lu et al [85] explored the nanoscale plasticity and shear-banding in metallic glasses in experiments, characterising the size effect as a shift from "distributed" to "localised" shear-banding at the nanoscale. Furthermore, by comparisons with dislocation-mediated plasticity in crystalline metals, they highlighted the distinct deformation mechanisms at play. Figure 3.1 in their work illustrates the evolution of shear offset and hardness with increasing indentation depth.

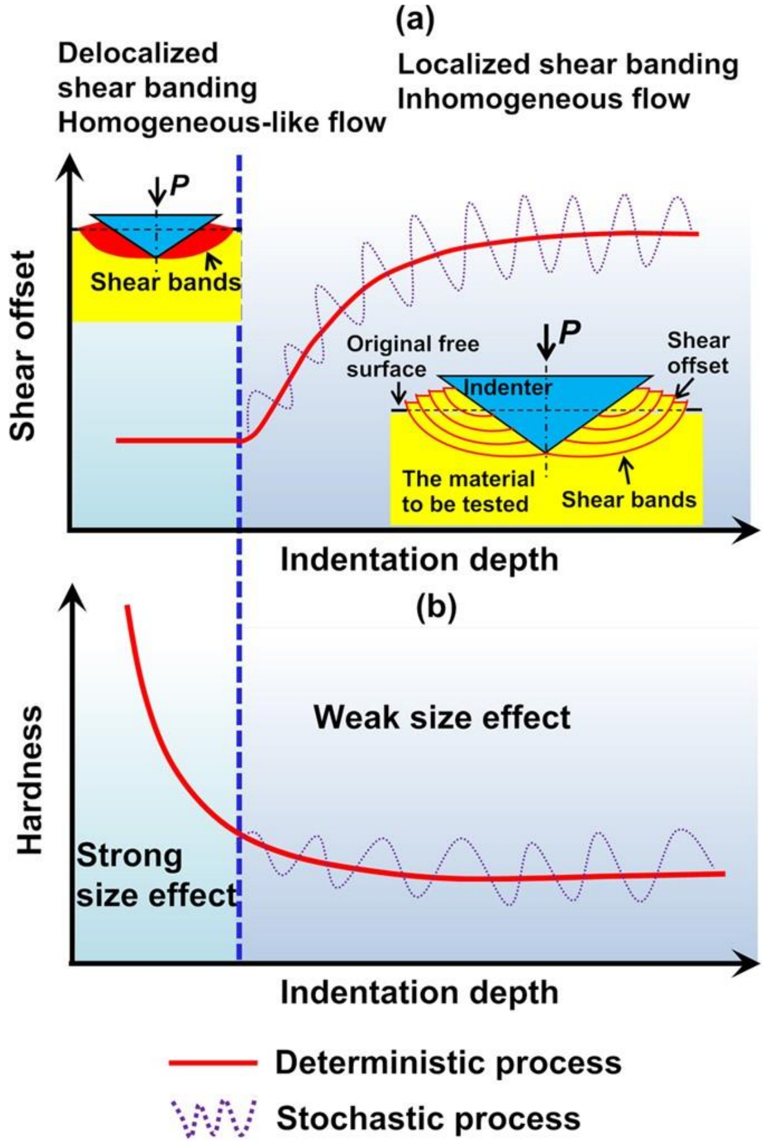

Figure 3.1 – Evolution of shear offset (a) and hardness (b) with increasing indentation depth [85].

The size effect in femtosecond pulsed laser ablation, which pertains to how dimensions of a material impact its response to ultrashort laser pulses, carries significant implications across a range of applications such as microfabrication, nanofabrication and nanoparticle synthesis. In the design and optimisation of processes involving USP laser ablation across different scales, careful consideration of the size effect is essential. Effectively understanding and accommodating this phenomenon is crucial for achieving precise and efficient material processing and manipulation. For example, Ridier et al [86] in an effort to examine ultrafast molecular switches triggered by ultrashort laser pulses, harnessed the size effect by manipulating the thickness of the thin film used in their work, allowing them to fine-tune the lattice response to laser irradiation. It contrasts with the “bulk effect” where in bulk crystals, the limited laser penetration depth results in an uneven dispersion of photoswitched molecules, along with the development of temperature and stress gradients within the specimen. These gradients, in turn, trigger delayed dynamic reactions linked to the propagation of strain waves and the diffusion of heat.

Considering the size effect is also of paramount significance when interpreting the results of MD simulations. Due to computational limitations, simulations often involve smaller representations of larger systems. The ability to make informed predictions hinges on recognising potential discrepancies in the behaviour of these representative models. Due to the computational constraints, it is often necessary to reduce the size or scale of the system being simulated. Therefore, it is essential to acknowledge that the behaviour of these smaller models may not perfectly mirror that of the full-scale system. As a result, when analysing simulation output, the size effect can manifest as differences in molecular interactions, thermodynamic properties or structural characteristics.

In summary, to draw meaningful conclusions and make accurate predictions from MD simulations, it is crucial to account for these size-related inconsistencies. It is vital to recognise that while simulations offer valuable insights, the accuracy of predictions made can be influenced by the choice of model size. Therefore, a thorough understanding of the size effect and its potential impact on simulation results is of utmost importance for conducting robust and reliable simulation studies in fields such as chemistry, materials science, and nanotechnology.

3.2. Mechanical properties

Mechanical properties of materials can be significantly altered due to the size effect. For instance, brittleness or ductility can change at the nanoscale compared to meso or macroscale. Dislocation glide processes play a facilitating role in plasticity, while the strength of a material is governed by the interactions between the dislocations. Uchic et al [87] in their work examined the size effect in pure Ni, which has a well-known mechanical behaviour of bulk single crystals and Ni_3Al-Ta that is considered to exhibit fundamentally unique flow mechanisms. They noticed the size effect in a larger than expected sample sizes. In their proposed method of characterising the size effect using a Focused Ion Beam (FIB), they aimed to minimise the deformation related to GNDs and argued that the demonstrated alterations in deformation mechanisms in this work extends beyond the gradient induced storage of defects. Therefore, defining the strength of a specific material at the micrometre length scale may not be achievable without thoroughly specifying the physical conditions. They argued that for some materials in submillimetre length scale, the internal structure and external geometry both affect the response of the material.

In relation to the size effect, the assertion that "smaller is stronger" is generally supported by the majority of studies. Nonetheless, there are instances where unexpected results arise, contributing to the ongoing research intrigue surrounding this topic. Nanoindentation technique is widely used in characterising mechanical properties of materials in submicron length scale. In an experimental work carried out by Pharr et al [88], they reported smaller is stronger in the length scale of the spherical nanoindenter used in their experiments. This is in contrast to geometrically self-similar indenters like cones and pyramids. In self-similar indenters the size effect manifests itself as increased hardness of the test sample in shallower penetration depths. Swadener et al [89] also previously reported similar mechanical behaviour exhibited in iridium alloy subjected to spherical and pyramidal indenters.

There is ongoing scientific discourse on the underlying mechanisms of the size effect in nanoindentation method. According to the conventional size effect theory, an escalation in dislocation density occurs at shallower indentation depths, leading to an increase in material hardness. However, some experimental studies observed and reported an increase in hardness of the material without a concurrent growth in dislocation density. McLaughlin et al [90] is one such example where they reported increased hardness in copper under lower loads. They suggested the size effect was linked to the diminished likelihood of encountering a suitable dislocation source within the loaded volume. There are also similar works [91,92] reporting such inconsistencies. It can be argued that challenges in direct observation and taking measurement in micro and nanoscale could also cause complications. Historically it was difficult to measure the exact zero point of the indentation tip to be used in calculations [93] and nowadays with available advanced instruments and innovative techniques, analysing behaviour of materials in nanoscale remains a laborious endeavour requiring more research.

3.3. Melting Point

Melting point of materials is an important parameter in the USP laser ablation process. Ablation threshold of a material is often lower than its melting point. This is because ultrashort laser pulses deliver energy to the material so quickly that it can be ablated before it has a chance to melt. During an ultrashort pulse in an ablation process, the heat generated is confined to a very small volume. As a result, the material around the ablation site remains relatively cool and there is a minimal HAZ compared to longer-laser pulses. This is advantageous when working with materials with low thermal conductivity or high melting points, as it reduces the chances of thermal damage to the surrounding of the beam spot area. Melting point also affects the resolidification of ablated particles and formation of the recast layer. In femtosecond pulsed laser ablation, the material is removed mostly in the form of a plasma plume of ionised atoms and electrons. The process is so rapid that there is limited time for the ablated material to resolidify. This is particularly important for materials with high melting points, as they may resolidify in a different crystalline form or with defects if heated and cooled slowly, which can affect the material properties.

Crystalline materials mostly have higher melting point in their pure form. In other words, impurities reduce their melting point. This is known as melting point depression and interestingly, the size effect can also influence the melting point. Some materials in smaller sizes like nanoparticles, can have lower melting points compared to their bulk counterparts. It can be argued that this happens due to the increased importance of surface energy as the size decreases, making it energetically favourable for the material to be in a different phase. This effect is known for a long time and in 1976 Buffat et al [94] demonstrated the size effect on melting temperature of gold particles. In the turn of the century, Zhang et al [95] investigated melting point of indium nanoparticles. Their experimental results indicated that the melting point of the investigated indium nanostructures decreased as much as 110 K for particles with a radius of 2 nm compared to the bulk material. Similarly, Little et al [96] studied silver nanoparticles via in situ real time spectroscopic ellipsometry, reporting variations in melting point with physical thickness and average nanoparticle diameter.

The underlying mechanism for melting point depression due to the size effect is not very well understood. Recently, Zhang et al [97] employed MD simulation to investigate NaCl (table salt) particles. They argued that in smaller nanoparticles, atomic motion was more vigorous, making the crystal structure more susceptible to disruption, resulting in a lower melting point. This trend in latent heat aligns with the coordination number, where a lower coordination number indicates a loosely packed structure. Consequently, less energy is needed to disrupt the crystalline lattice, leading to a decrease in latent heat as well.

3.4. Electrical and Thermal Conductivity

The electrical and thermal conductivity of materials can also be influenced by size. In nanoscale materials, the scattering of electrons and phonons at boundaries and interfaces becomes more significant, leading to changes in conductivity. Tong et al [98] examined electrical and thermal responses in different grain sizes of pure Mg and found that the grain size had insignificant effect on residual electrical resistivity, but the thermal coefficient of resistant varied in their work.

Researchers in the realm of thermoelectric materials, especially for energy-related applications and integrated circuit cooling [99], are actively pursuing the capability to independently manipulate a thermal conductivity of materials apart from its electrical conductivity. This objective is driven by the fundamental premise that thermal conductivity and electrical conductivity can theoretically be fine-tuned separately within semiconducting nanostructures. This separability arises from the clear distinction in length scales governing the behaviour of phonons (the agents responsible for heat conduction) and electric charges (the carriers of electrical current). Yu et al [100] explored this phenomenon, successfully reducing the thermal conductivity of silicon nanomesh films by manipulating their dimensions, all while keeping electrical conductivity consistent with that of the bulk material.

In USP laser ablation, both thermal and electrical conductivity of the material being ablated can have significant effects on the ablation process. The thermal conductivity of a material affects its ability to conduct heat away from the ablation zone generated by the laser pulse. Materials with high thermal conductivity can dissipate the heat more efficiently, potentially reducing the extent of material removal which in turn increases the threshold fluence. Conversely, materials with low thermal conductivity are more likely to experience localised heating and vaporisation, leading to more efficient ablation. The electrical conductivity plays a role in how efficiently the material absorbs the laser energy. Materials with higher electrical conductivity tend to absorb laser energy more effectively, leading to faster heating and potentially more efficient ablation. In USP laser ablation, a plasma plume is often generated due to the intense heating of the material. The electrical conductivity can affect the dynamics of plasma formation and expansion. Highly conductive materials may generate more energetic plasmas, which can influence the ablation process by partially absorbing the incoming laser irradiation and affecting the quality of the resulting features.

3.5. Surface Effects

As the size of a material decreases, the surface-to-volume ratio becomes significant and a higher proportion of its atoms or molecules are located at or near the surface. This can result in increased surface energy, reactivity, surface diffusion, surface adsorption and other surface-related properties that differ from those of the bulk material. In their review paper, Ouyang et al [101] classified surface morphology into those having nanostructures with positive curvatures and ones with negative curvatures and elucidated how thermodynamic properties are influenced by surface effect in nanostructures with negative curvature.

Surface effects can significantly influence USP laser ablation in several ways. Surface effects can lead to enhanced absorption of femtosecond laser pulses at the surface of the material. When a USP laser interacts with a surface with nanoscale textures, it can couple more effectively with the surface features due to increased surface area and multiple scattering events. This enhanced absorption can result in more efficient energy transfer to the material, leading to faster ablation and reduced laser fluence requirements for material removal. In a theoretical study, Klimo et al [102] argued that a target with diminished dimensions and surface microstructures may gain advantages from increased absorption and effective redirection of hot electrons. They employed numerical simulations based on Particle-in-cell (PIC) code [103] to demonstrate thin foil coated with a monolayer of polystyrene spheres, each having a diameter on the scale of the laser wavelength that was a promising candidate for taking advantage of the surface effect for such a target.

Surface effects can lead to the localisation of energy near the surface, where it can be absorbed and concentrated. This is particularly important in USP laser ablation, because these lasers deliver energy within an extremely short pulse duration. Energy localisation at the surface can induce rapid heating and ionisation of surface atoms or molecules, promoting the ejection of material. Multiphoton absorption can also be more pronounced near the surface due to the high local intensity of ultrashort laser pulses. These effects can lead to more efficient ionisation and excitation of electrons in the surface region [104].

Surface effects can lower the ablation threshold, which is the minimum laser fluence required to initiate material removal. This occurs because surface states or defects may introduce additional energy levels within the bandgap of the material, making it easier to achieve the energy required for ablation. Lower ablation thresholds near the surface allow for finer control over the ablation process and enable precision micromachining and material patterning. Therefore, surface morphology and roughness can be controlled and tailored for specific applications, such as creating superhydrophobic surfaces or enhancing the performance of photonic and optoelectronic devices.

3.6. Examples of size effect reports informed by simulations

Bardella and Panteghini [105] employed the finite element method to simulate the response of copper nanorods to torsional forces, with a particular focus on investigating the size effect. Their study incorporated Gurtin's gradient theory [106] , which accounts for the unrecoverable energy component of plastic spin, referred to as "dissipative" in addition to the conventional strain gradient plasticity theory. In Figure 3.2, they demonstrated a comparison between their simulated data and empirical values derived from Fleck et al [107]. Notably, the void symbols in this figure represent calculated values that exhibit a commendable alignment with experimentally measured data.

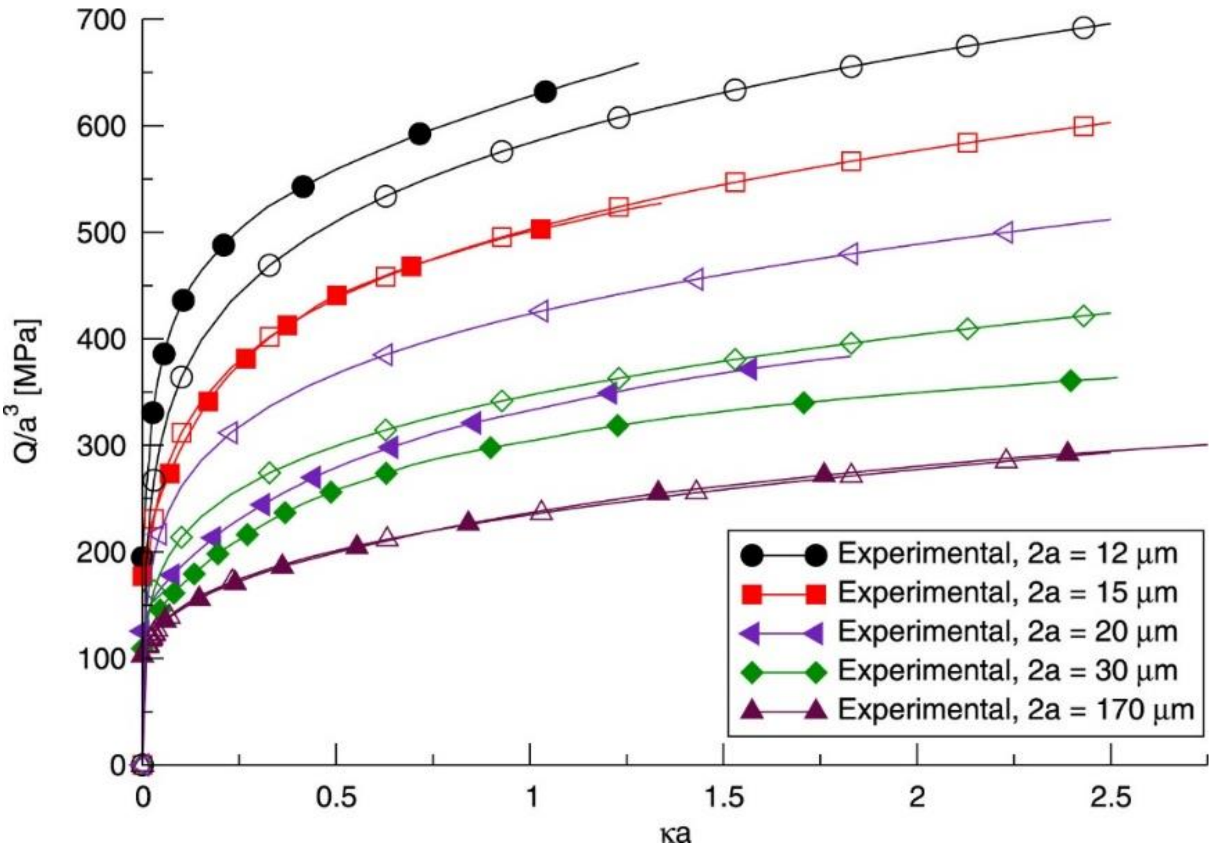

Figure 3.2 - Bardella and Panteghini's simulation results (denoted by void circles) [105] *compared to Fleck et al experimental data for torsional response of copper nanowires with diameters in the range of 12-170 µm. a = wire radius, Q = torque and K = twist per unit length* [107].

In their research, Goel and colleagues [108] utilised MD simulations to investigate the mechanical characteristics of nanocrystalline tantalum within a displacement-controlled nanoindentation simulation. They demonstrated the hardness variation obtained from MD simulation of the nanoindentation of 200 nm film of tantalum. As depicted in Figure 3.3, they demonstrated the region where the size effect phenomena influenced the response of material to the induced forces.

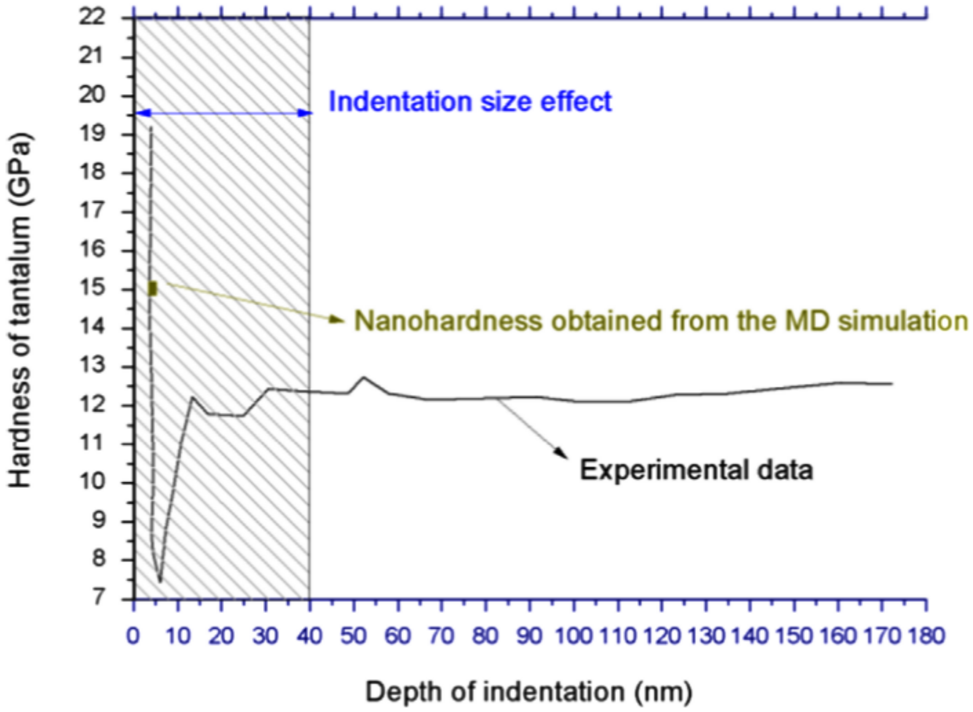

Figure 3.3 - Hardness variation in nanoindentation of tantalum obtained from a 200 nm film [108].

Wu [109] also conducted atomistic simulations to investigate the bending of copper nanorods, revealing results that contradicted predictions based on continuum mechanics. This discrepancy in material response at this scale was attributed to the influence of the surface effects. Utilising MD simulations to investigate organic films [110] and fluids [111] has also argued that surface effects are key factors contributing to inconsistencies in materials' response at the submicron length scale.

3.7. Summary

In this chapter, the size effect in literature was explored, discussing how the mechanical properties, melting point, electrical and thermal conductivity as well as surface effects are intertwined with size-dependent dynamics relevant to USP laser ablation. In the subsequent chapters, this exploration extends, focusing specifically on the size of the laser beam and grains of titanium substrates. Utilising both MD simulations and experiments, this comprehensive approach was designed to further investigate how the size effect manifests in the context of USP laser ablation. This knowledge allows for optimising ablation processes, reducing the HAZ, improving surface quality and ablation efficiency, ensuring consistency, reducing waste and advancing the technology development.

Chapter 4 — Research methodology

4.1. Introduction

In this study, MD simulations was the primary tool for investigating the process of USP laser ablation of titanium. The methodology involved the setup and execution of LAMMPS code to simulate the interactions between the laser pulse and the material at the atomic level. The simulation setup involved modifying the TTM package to account for temperature dependency of the electronic properties and enabling the modelling of the custom shape of beam affected area as well as defining the parameters of the laser pulse, such as fluence, pulse duration and spot size. Additionally, the substrate material, titanium in this work, was modelled at the atomic scale using EAM interatomic potentials. These potentials capture the interactions between atoms within the material and allow for the accurate prediction of material behaviour under different conditions.

Post-processing of simulation results, as described in more detail in this chapter, involved two primary approaches. Firstly, temperature profiles and probing were conducted wherein the core LAMMPS code computed various thermodynamic properties across the simulation period. Strategic grouping of atoms in key regions facilitated the recording of local temperatures, aiding in comprehensive data collection. Statistical analyses and visual representations using Microsoft Excel were then employed to discern trends and patterns within the data. Secondly, visual representation was pursued by employing an independent computational command to calculate kinetic energy for each atom at regular intervals during the simulation. OVITO software then facilitated the visualisation of atomic movement, geometrical changes and the evolution of melt pools.

In preparation for experiments, this chapter outlines steps taken to ensure sample integrity and compatibility with laboratory instruments. Commercially pure titanium, as well as samples machined from cast Ti-6Al-4V alloy and 3D-printed counterparts, were sourced. It also includes steps taken to plan and execute experiments as well as SEM and AFM instruments used to collect experimental data. In simulations, the largest feasible atomic system was modelled to capture atomistic behaviour, providing insights into overall trends during the USP laser ablation. On the other hand, experiments focused on measuring with a high resolution the smallest possible craters using techniques like AFM and SEM. Combining these approaches helped the study gained a comprehensive understanding of the impact of the beam spot size as a laser parameter and grain size representing some of the material properties, thus, pushing the boundaries in comparing simulation predictions with experimental observations in this length scale.

MD simulations is the primary tool for investigating rapidly unfolding events during USP laser ablation due to several key reasons. First and foremost, MD simulations offer unparalleled temporal resolution, enabling atomic-scale observation of processes unfolding in femtoseconds and picoseconds. This level of temporal granularity is essential for capturing the rapid dynamics inherent in USP laser ablation, where material interactions occur on extremely short timescales.

Additionally, computational modelling offers flexibility and control over experimental parameters, such as laser fluence, beam spot size and material properties. This control enables varying parameters systematically and explore their effects on the ablation process, which may be challenging or impractical to achieve experimentally. Furthermore, MD simulations offer a cost-effective alternative to experimental studies of USP laser ablation, which can be costly and time-consuming. MD simulations was first used by Cleveland et al [35] in 1982 to study laser annealing and ever since it has been used by majority of researchers in this field, for example [43,44,45,112,113,114], either individually or accompanied by experiments to study laser ablation of various pulse energy and durations, investigating diverse aspects of this process such as physical mechanisms involved in the process, size of the ablated particles and their velocities and so on.

The investigation of USP laser ablation holds significant promise in various fields, ranging from materials science to industrial applications. This chapter presents the employed methodology aimed at studying the USP laser ablation with emphasis on the impact of beam spot size and the grain size of the substrate material on the process, with implications for precision manufacturing in nanoscale. Figure 4.1 represents the overview of this methodology.

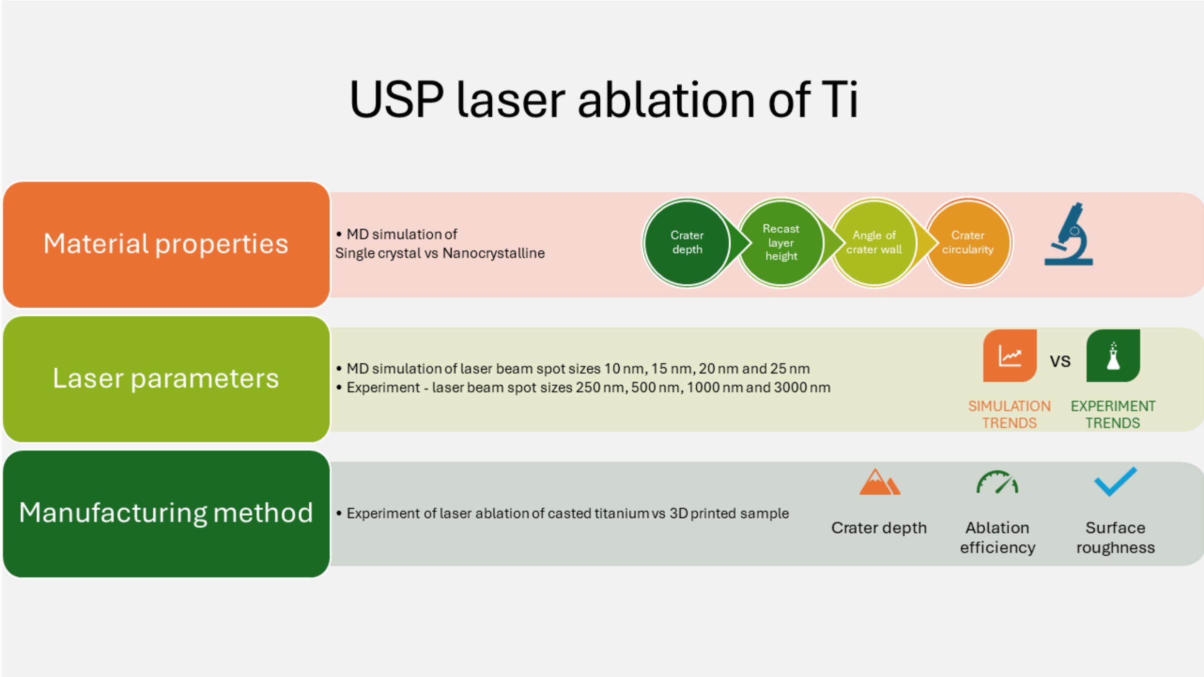
USP laser ablation of Ti

Material properties
- MD simulation of Single crystal vs Nanocrystalline

Crater depth
Recast layer height
Angle of crater wall
Crater circularity

Laser parameters
- MD simulation of laser beam spot sizes 10 nm, 15 nm, 20 nm and 25 nm
- Experiment - laser beam spot sizes 250 nm, 500 nm, 1000 nm and 3000 nm

SIMULATION TRENDS
VS
EXPERIMENT TRENDS

Manufacturing method
- Experiment of laser ablation of casted titanium vs 3D printed sample

Crater depth
Ablation efficiency
Surface roughness

Figure 4.1 – Overview of methodology used in this thesis.

4.2. Material

In this project, all experiments and simulations were conducted on titanium samples. As previously mentioned, the primary objective of this project aligns with the broader research focusing on surface treatments of implants to reduce the risk of post-surgery infections. Titanium is a material of great significance in numerous industries due to its unique set of properties, which include high strength, low density, exceptional corrosion resistance and biocompatibility. Its importance becomes evident in applications where durability, reliability and performance are critical. Titanium remains a valuable material in the development of cutting-edge technologies and a wide range of products.

In the realm of medical science, titanium plays a pivotal role in the fabrication of various types of medical implants. These encompass dental implants, joint replacements and various orthopaedic devices. Biocompatibility of titanium and its ability to osseointegrate with bone tissue are essential in enhancing the quality of life for numerous patients. Titanium, despite its current ubiquity, is a relatively recent discovery dating back to 1791 in Cornwall, United Kingdom. Its primary source is derived from naturally occurring mineral ores, with ilmenite, rutile and titanite being the most prevalent sources. Commercially, titanium is available in various grades and alloys. Simulations in this study were conducted on pure titanium. Commercially available pure titanium Grade 2 was processed and utilised in laboratory experiments. Additionally, titanium alloy Grade 5 (Ti-6Al-4V) was processed and used in experiments due to its widespread popularity in the world of materials science and engineering. This popularity stems from its exceptional versatility, which allows it to be tailored to meet specific requirements with tuning some of its properties, simply by adjusting the heat treatment process in its manufacturing.

4.2.1. Composition

Grade 2 titanium, also known as commercially pure titanium Grade 2 (CP Grade 2), is one of the most used grades of titanium due to its excellent combination of properties and relatively low cost. It is characterised by its high purity and lack of significant alloying elements. The composition of Grade 2 titanium typically conforms to specific standards and can vary slightly depending on the exact specifications. Titanium is the primary element, making up most of the composition, typically exceeding 99% by weight. This high purity distinguishes Grade 2 titanium as "commercially pure."

Oxygen is the most common impurity in Grade 2 titanium. The maximum allowable oxygen content is usually specified by industry standards, and it is typically kept very low, often less than 0.25% by weight. Reducing the oxygen content is crucial to maintain the ductility and formability of the metal. Iron is another common impurity in Grade 2 titanium. Its presence is usually controlled to keep the content below a specified maximum level, often less than 0.3% by weight. Grade 2 titanium typically also has a low carbon content, usually less than 0.08% by weight. Keeping the carbon content low is important to maintain the ductility and corrosion resistance. Nitrogen is generally kept at low levels, typically less than 0.03% by weight and the hydrogen content is usually minimised to maintain the metal's integrity and prevent embrittlement.

High purity of Grade 2 titanium makes it highly corrosion-resistant, biocompatible and suitable for a wide range of applications, including medical implants, aerospace components and chemical processing equipment. Its excellent combination of properties, along with its availability and cost-effectiveness, contribute to its widespread use. The specific composition of Grade 2 titanium can exhibit variations contingent upon the manufacturing process and adherence to industry standards. The titanium sample used in this project was sourced as a plate with a remarkable purity level of over 99.6%. This high purity titanium plate was supplied by Advent Research Materials in the United Kingdom, accompanied by a Certificate of Conformity. This document indicated that the titanium plate was manufactured through a process known as "Temper annealed". Additionally, it included parts per million analysis (PPM) detailing containing elements other than titanium as:

- Carbon (C): 200 PPM
- Nitrogen (N): 120 PPM
- Hydrogen (H): 50 PPM
- Iron (Fe): 1500 PPM
- Oxygen (O): 1500 PPM

4.2.2. Crystal structure

Titanium adopts several different crystal phases, depending on temperature and pressure conditions. Its crystal structure is primarily hexagonal close-packed (HCP) at temperatures below 1155 K and body-centred cubic (BCC) at elevated temperatures. At temperatures below 1155 K, titanium atoms are arranged in layers of hexagonally close-packed, known as the alpha phase (α-Ti). This structure is characterised by a hexagonal unit cell and it provides titanium with its high strength, low density and excellent corrosion resistance. Alpha-titanium serves as the primary focus in the MD simulations conducted within this project.

At temperatures above 1155 K, titanium undergoes a phase transformation to a BCC crystal structure known as the beta phase (β-Ti). Beta-titanium has a cubic unit cell and its atomic arrangement is less tightly packed compared to the HCP structure.

Beta-titanium is characterised by improved ductility and formability, making it suitable for applications where these properties are essential. Some titanium alloys, called beta alloys, are intentionally designed to maintain the beta phase at lower temperatures.

Many titanium alloys, such as Ti-6Al-4V are designed to exhibit a combination of both alpha and beta phases. These alloys are often referred to as alpha-beta or α-β alloys. By carefully controlling the alloying elements and heat treatment, these materials can be tailored to have a balance of properties, including strength, corrosion resistance and formability. The ability of titanium to exist in multiple phases provides the flexibility to design and select titanium alloys that meet specific requirements for a wide range of applications. For example, in aerospace, alpha-beta alloys like Ti-6Al-4V are often used for components requiring high strength and good weldability, while pure alpha-titanium is used in medical implants for its biocompatibility and corrosion resistance. Understanding the crystal structure and phase transitions of titanium is essential for optimising the performance of materials in different environments and applications.

In this project, an X-ray diffraction analysis (XRD) was conducted to verify the crystal structure of the CP sample before and after the ablation process. This also enabled the assessment of any possible morphological changes resulting from the laser ablation treatment by comparing the XRD results. XRD is a powerful analytical technique used to study the structure of crystalline materials. It relies on the principle of X-ray interference when they interact with a crystalline solid. The analysis was performed using a Bruker D8 X-ray diffraction machine at London South Bank University, using copper at the wavelength of 1.5406 Å, operated in the Bragg-Brentano mode. Data was collected within the range of 10 to 100 degrees with 0.02-degree increments for both the pre- and post-ablation examinations. Subsequently, the obtained data was processed using Match and Microsoft Excel software. Figure 4.2 is the image of the machine while processing the sample pre-ablation.

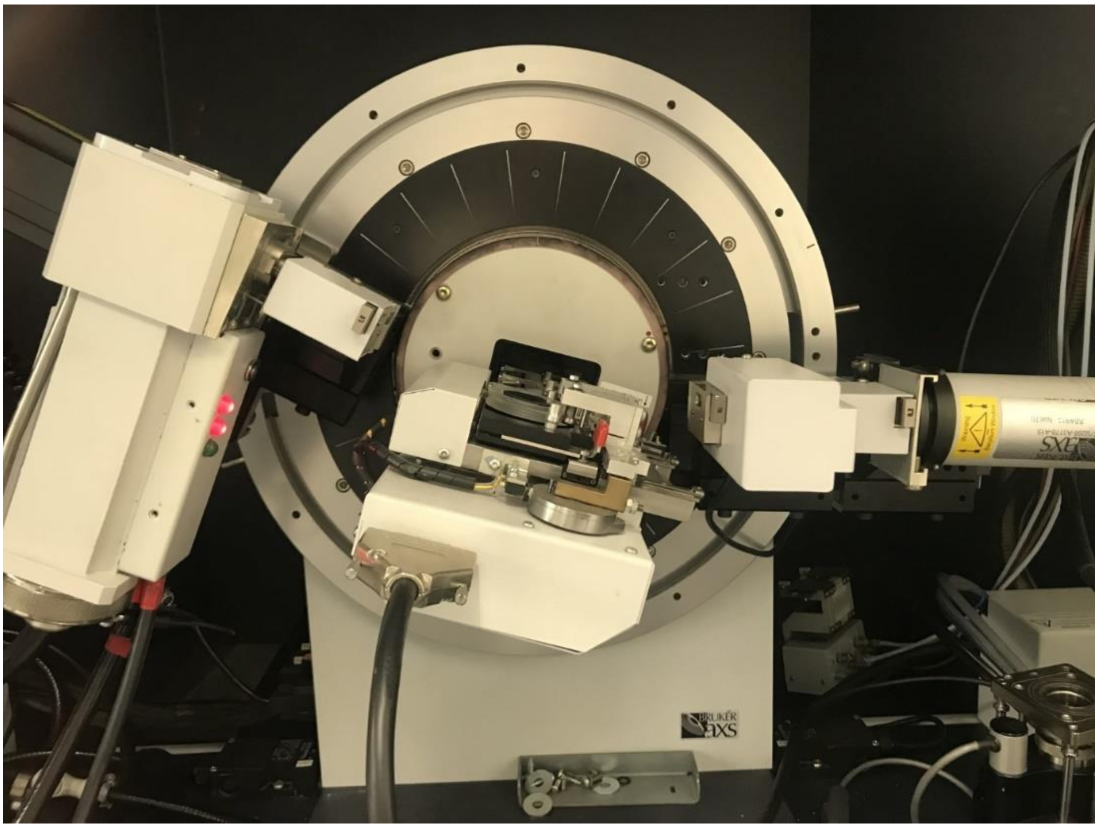

Figure 4.2 - Bruker D8 X-ray machine processing CP titanium for XRD analysis at London South Bank University.

The HCP spacings based on the peak angles observed in the XRD data aligned with the peak angles reported for the alpha phase titanium (α-Ti) in the literature [115,116,117]. Figure 4.3 shows the XRD graph, illustrating peak angles consistent with the expected HCP lattice structure of CP titanium. Given the limited dimensions of the ablated craters site, not exceeding 50 µm x 100 µm at most compared to the overall scanned surface dimensions of 10 mm x 10 mm, variations within this range are challenging to perceive. Interplanar spacing at each peak was calculated using Bragg's law, detailed in table 4.1. Miller-Bravais indices of peaks occurring at 35, 40 and 63 degrees for pure titanium were previously reported by Conforto and Caillard [118] corresponding to planes $01\bar{1}0, 1\bar{1}01$ and $11\bar{2}0$ respectively. Peak matches with crystallography open database (COD) obtained from the Match-3 software correspond to [96-901-6191] Ti and [96-900-0935] Fe2 O4 Ti documents.

Table 4.1 - d spacing calculated using Bragg's law.

2θ (°) **pre-ablation**	**2θ (°)** **post-ablation**	**d_{hkl} (Å)** **pre-ablation**	**d_{hkl} (Å)** **post-ablation**	**Plane** **(α-Ti)**
			$d_{hkl} = \frac{\lambda}{2\sin\theta}$	$\lambda_{cu} = 1.5406$ Å
26.6	26.7	3.35	3.34	
35.1	35.3	2.55	2.54	$(01\bar{1}0)$
40.2	40.3	2.24	2.24	$(1\bar{1}01)$
63.0	62.9	1.47	1.47	$(11\bar{2}0)$
74.2	74.3	1.28	1.28	
77.3	77.4	1.23	1.23	

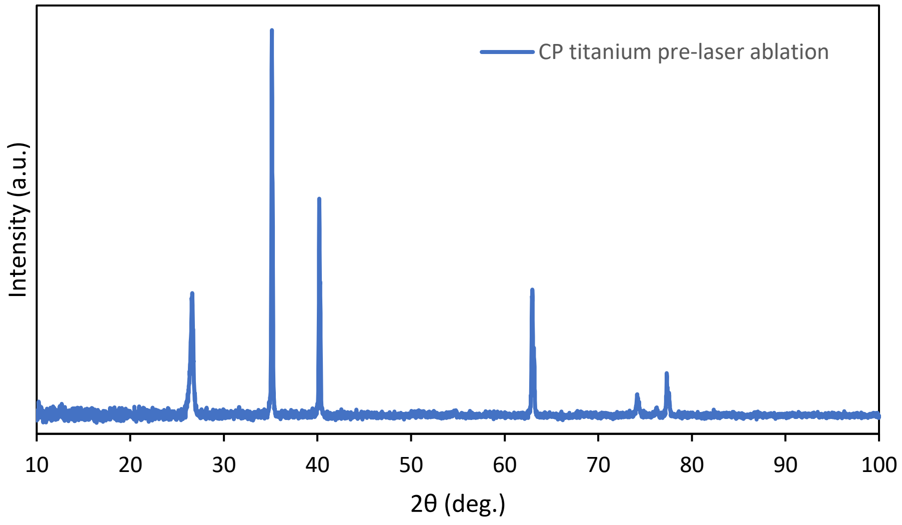

Figure 4.3 - XRD plot indicating peak angles for the CP titanium sample before laser ablation.

4.3. Simulation

The Large-scale Atomic/Molecular Massively Parallel Simulator, known as LAMMPS, is a code that focuses on materials modelling at the atomic scale using molecular dynamics. It is an open-source software primarily developed by the Sandia National Laboratories in the USA [119]. This PhD project used LAMMPS for all the simulations due to its efficient parallelisation, comprehensive documentation and flexibility for different applications. Moreover, LAMMPS can be easily modified to meet specific requirements, such as incorporating the two-temperature model and modelling a laser beam as an external energy source, which are unique to USP laser ablation and essential for the context of this work. The base code package employed for this project was the user-package TTM (two-temperature model), which was developed by Phillips et al [120] for studying radiation damage. It uses an explicit approach with an inhomogeneous Langevin thermostat applied locally, and the core simulator follows the conservation of energy and Newton's law of motion. Energy transport between the electronic and atomic subsystems is solved according to the heat diffusion equation:

$$C_e \rho_e = \frac{\partial T_e}{\partial t} = \nabla(K_e \nabla T_e) - g_p(T_e - T_a) + g_s T_a' \tag{4.1}$$

where C_e is electronic heat capacity, ρ_e is electron density, T_e is electronic temperature, K_e is electronic heat conductivity, g_p is electron-phonon coupling factor, T_a is atomic temperature and g_s is electron stopping parameter.

The effects of inelastic scattering by electrons are incorporated into the equation of motion through a friction term. The energy lost due to electronic stopping or electron-ion interactions is fed back to the system via a source term. The underlying algorithm for this thermostat is based on the work of Duffy and Rutherford [121,122], who argued that electrons can reach very high temperatures and significantly alter material properties for up to 300 femtoseconds at the beginning of simulations. In this code, electrons are represented by finite element (FE) grid points that overlap with the atomic subsystem. Electronic properties are provided as input parameters and energy equations are solved separately for each subsystem. The calculated energy is then exchanged between the electronic and atomic subsystems at a rate (r in Figure 4.4) controlled by a coupling factor (denoted as G in Figure 4.4). The electronic properties and coupling factor can be estimated using Density Functional Theory (DFT) calculations. Figure 4.4 illustrates the electron-phonon interactions within the TTM user-package.

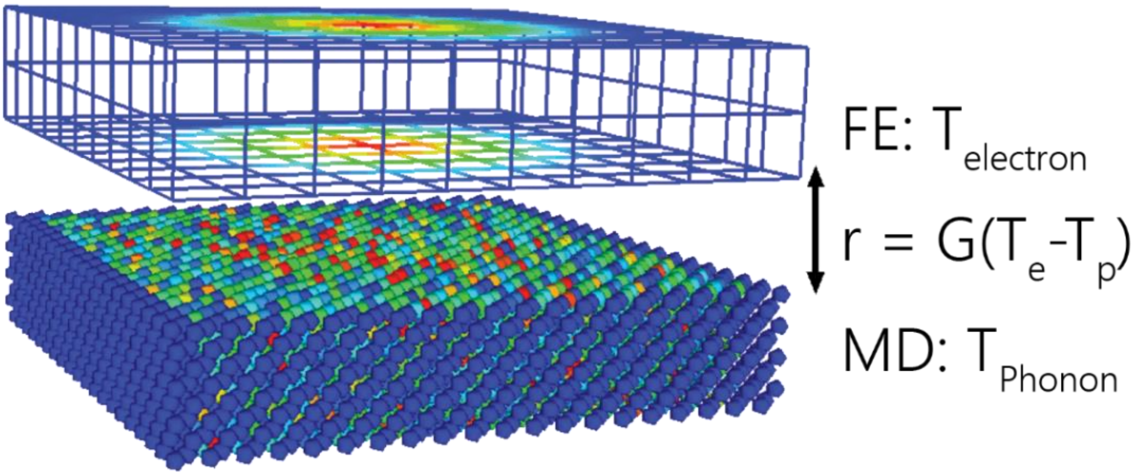

Figure 4.4 - Electron-phonon interaction in LAMMPS user-package TTM [123]. *$T_{electron}$ = T_e, and T_{Phonon} = T_p.*

4.3.1. Modelling substrate

Modelling and equilibration of single crystal and polycrystalline samples were conducted at room temperature (300 K) using LAMMPS. The models assumed the HCP lattice structure to represent the alpha phase of titanium, with equilibrium lattice parameter of a_0 = 2.951 Å and c/a ratio of 1.587, at 300 K [124]. Subsequently, random velocities were assigned to each atom and a Nose/Hoover thermostat and barostat were applied to adjust the temperature to 300 K and the pressure to 1 atmospheric unit, while periodic boundary conditions were implemented in all three dimensions. The LAMMPS code utilised a constant isothermal-isobaric NPT integration method to update the positions, velocities, orientations and angular velocities of the particles at each iteration of the simulation (equal to 1 femtosecond), with the thermostat applied to both translational and rotational degrees of freedom.

For the polycrystalline substrates, a similar equilibration procedure was followed with the distinction that the initial atomic system was generated externally and then accessed by the LAMMPS code. To create the initial atomic system, a C++ script developed by Alexander Stukowski (https://gitlab.com/stuko) was utilised to organise substrate atoms into a predefined number of grains of random sizes based on a Voronoi Tessellation scheme. Running each simulation for 100,000 iterations, equivalent to 100 picoseconds, resulted in the creation of alpha phase pure titanium systems at 300 K.

4.3.2. Development of additional software package

To incorporate external laser beam energy into the LAMMPS code, a modification was introduced enabling the addition of an extra grid file, alongside the one needed for initialising electronic temperatures. This file contains grid points identical to those employed for setting initial temperatures within the electronic subsystem, however, it includes additional energy in the form of elevated temperatures at specific grid points, simulating the laser beam while adding zero temperature to the bulk. This approach enables independent modelling of a laser beam with user-defined geometry, which can be embedded into the LAMMPS model with a substrate.

The updated code now necessitates an additional user-input parameter for specifying the pulse duration. This parameter determines the number of timesteps during which the average beam temperature, specified by previously built grid file, representing the laser beam, will be merged with the electronic temperature profile. To facilitate this process, a C++ script was developed to populate grid points, initial electronic temperatures and a Gaussian beam profile with user-defined characteristics such as diameter of beam spot area, depth and average beam temperature. This script produces these two input files crucial for operation of the modified TTM code this script can be downloaded from: https://github.com/Parris-G/Laser-beam-and-electronic-grid-generator.git.

Moreover, the original code was modified to accommodate a spectrum of electronic heat capacity and coupling factor values sourced from external text files, as per user-defined specifications, as opposed to the singular value entries found in the original package. This adaptation was implemented to consider the temperature-dependent nature of these electronic properties throughout the laser ablation process, as documented in prior research [43,125,126]. Furthermore, recognising the direct proportionality between electron heat conductivity and electronic heat capacity, the code was subsequently adjusted to dynamically adjust the single input value for electronic heat conductivity in accordance with the fluctuations in electronic heat capacity used during the ablation procedure. The new modified code was named "ttm/laser" and it is available to download from https://github.com/Parris-G/TTM-LASER.git. The LAMMPS code must be compiled with this code added to the folder named “src/EXTRA-FIX” and to initiate the fix (as referred to in LAMMPS), the user must use the modified syntax in the following format:

fix ID group-ID **ttm/laser** seed rho-e kappa-e gamma-s v-0 Nx Ny Nz infile <file name> outfile N <file name> **pulse-duration beamfile <file name> Cfile <file name> Gfile <file name>**

In this context, units are the same as the original package in LAMMPS and the parameters and their descriptions are as follows:

- **ID**: This is the identifier for the fix.
- **group-ID**: It refers to the name of the group of atoms to which this fix will be applied.
- **ttm/laser**: This initiates the modified code for TTM.
- **seed**: A random seed number for generating random data.
- **rho-e**: The electron density.
- **Kappa-e**: The electronic heat conductivity.
- **gamma-s**: The friction coefficient due to electronic stopping.
- **v-0**: The critical velocity for electronic stopping.
- **Nx**, **Ny**, **Nz**: These represent the number of grid points in each direction.
- **infile**: A switch indicating the input file, followed by a user-defined name for the initial grid temperatures.
- **outfile**: A switch indicating the output file, followed by a user-defined name for the calculated electronic temperatures.
- **N**: The number of timesteps for which the electronic temperature will be calculated and stored in the output file.
- **pulse-duration**: An integer specifying the number of timesteps during which beam temperatures, defined in the grid file will be added to the electronic grid.
- **Beamfile**: A switch indicating the input laser beam file, followed by a user-defined name for the average electronic temperatures representing the laser beam.

- **Cfile**: A switch indicating the file containing values of temperature dependent electronic heat capacity.
- **Gfile**: A switch indicating the file containing temperature dependent electron-phonon coupling factors.

4.3.3. Electronic properties of titanium

While the two-temperature model primarily focuses on the separation of electronic and lattice temperatures, the accurate description of electronic properties and their interactions with the lattice is crucial for obtaining meaningful results. These properties influence various aspects of the simulation, including energy transport, phase transitions and specific heat capacities and should be considered when setting up and interpreting two-temperature MD simulations. The calculations in this study made use of several electronic properties including electron density, electronic specific heat capacity, electronic heat conductivity and the electron-phonon coupling factor (representing the energy exchange rate with the lattice). The specific values and their respective sources are detailed in the following sections.

4.3.3.1. Electronic density

The electron density was determined by running a simulation on LAMMPS and comparing the results with values reported in the literature. A titanium atomic system with dimensions of 15 x 15 x 15 Å was created, and the energy of the system was minimised to achieve an equilibrium condition at room temperature (300 K). The central volume of the simulation box, measuring 10 x 10 x 10 Å, contained a total of 56 atoms. Therefore, the electron density was calculated based on this configuration as:

$$Number\ of\ atoms\ \rightarrow \quad \frac{56}{1000} = 0.056\ /\ \text{Å}^3$$

$$number\ of\ valence\ electrons\ per\ atom = 4\ \ \rightarrow \rho_e = 0.056 \times 4 = 0.224\ {}^{valence\ e}\!/_{\text{Å}^3}$$

Çatli in a study [127] calculated number of electrons in one cubic centimetre of pure titanium with computed tomography (CT) method to be 12.56 X 10^{23}. Therefore:

$$12.56 \times 10^{23} \times \frac{1\ cm^3}{10^{24}\ Å^3} \times \frac{4\ (valence\ e)}{22\ (all\ electrons)} = 0.2284\ {}^{valence\ e}/_{Å^3}$$

The difference between the two values is negligible, and for this project, the value calculated by LAMMPS was utilised.

4.3.3.2. Electronic heat conductivity

The thermal conductivity of annealed pure titanium at 300 K, as measured by Ho et al [128], is 0.219 W/(cm K). This value was converted to the units used in this simulation, which is 0.014 eV/ps (Å K).

4.3.3.1. Electronic specific heat and Electron – Phonon coupling factor

The coupling factor and electronic heat capacity values were calculated in the temperature range of 300-50,000 K by Lin et al [43,129,130,131] and He et al [113] using DFT simulations. Each dataset was stored in its own distinct file and made accessible to the script utilising LAMMPS software. Each file comprised a reference temperature followed by the corresponding calculated value, either for the electronic heat capacity or the electron-phonon coupling factor, in approximately 1000 increments. During each timestep, a modified function scoured the files for values corresponding to the current electronic temperature and integrated them into the relevant calculations to precisely establish a new electronic subsystem interaction with the atomic system.

4.3.4. Laser beam energy and profile

The format of the initial electronic grid temperature file, which was accepted by the original TTM package within LAMMPS, included integer coordinates for x, y, and z, followed by the temperature value at each line initiating the electronic temperature for the grid point. The number of grid points is dependent on the size of the simulation box, with a guideline of approximately 1000 atoms associated with each grid point for a balanced efficiency and accuracy. This format was employed to define the laser beam profile added to the system.

The laser beam profile encompassed an array of temperature values, varying in intensity based on the energy distribution profile on XY plane and according to the Beer-Lambert law at Z axis, as it permeated the beam geometry. This design allowed for the creation of laser beam profiles with diverse geometries, such as Gaussian, cylindrical or rectangular shapes, which were constructed outside the simulation environment. This approach granted significant flexibility in modelling a wide range of ablation processes. To streamline the generation of grid and beam profile data for larger and more complex simulation setups, the C++ script explained in section 4.2.2 was used. This script employed nested loops to systematically generate the required input values, thus facilitating the preparation of input data for extensive simulations. The equation of circle in a Cartesian coordinate system with its centre at (h, k) and radius r is:

$$(x-h)^2+(y-k)^2=r^2 \tag{4.2).}$$

A function in the code subsequently verifies whether the grid point (x, y) lies within the circular region defined by:

$$\sqrt[y\leq]{\left(r-\left(\frac{Z}{Z_{surface}}-z\right)\right)^2-(x-x_{centre})^2+y_{centre}+x_{centre}}$$

$$\sqrt[y\geq]{\left(r-\left(\frac{Z}{Z_{surface}}-z\right)\right)^2-(x-x_{centre})^2+y_{centre}+x_{centre}}$$

(4.3)

for each XY plane. If the condition is satisfied, the average temperature is added to the grid; otherwise, the value zero is assigned to the grid. To populate grid points on the next XY plane, both the radius and the assigned temperature values shrink by a user-defined percentage to achieve the desired output.

These input files are in text format and may include lines with comments indicated by the '#' character. Each line comprises four numeric columns: i_x, i_y, i_z, Temperature. Lines that are either empty or solely consist of comments will be disregarded. The total number of lines should match the specified grid points set by the user (N_x by N_y by N_z). The indices i_x, i_y, i_z represent grid points, ranging from 1 to N_{xyz} inclusive in each dimension. The order of lines within the file is flexible. As an illustration, the initial electronic temperatures for a grid of dimensions 1 by 2 by 3 can be specified in the file in various orders as the following:

```
# COMMENT: initial electron temperature
1 1 1 300.0
1 1 2 300.0
1 1 3 300.0
1 2 1 300.0
1 2 2 300.0
1 2 3 300.0
```

4.4. Interatomic potential

The Embedded Atom Method (EAM) is a theoretical framework used in materials science and condensed matter physics to describe the interatomic potential energy in a material. The EAM potential represents the energy associated with the interactions between atoms in a crystal lattice. In the EAM model, each atom is embedded in a background electron density, and the energy of an atom is a function of both its own electron density and the electron densities of neighbouring atoms. The central idea is that the total energy of the system is a sum of two components, embedding energy and pairwise interaction energy. Embedding energy accounts for the interaction between an atom and the background electron density. It represents the energy required to place an atom in the electron cloud created by all the other atoms in the system. The embedding energy is often represented as a function of the local electron density at an atom's position. Pairwise interaction energy on the other hand is the energy associated with the pairwise interactions between atoms in the material. It typically includes contributions from short-range repulsion, long-range attraction and intermediate-range interactions. To calculate these values, equation 4.4 is used:

$$E_i = F_\alpha\left(\sum_{j\neq i}\rho_\beta(r_{ij})\right) + \frac{1}{2}\sum_{j\neq i}\phi_{\alpha\beta}(r_{ij}) \tag{4.4}$$

where F is the embedding energy which is a function of the atomic electron density ρ, ϕ is a pair potential interaction, and α and β are the element types of atoms i and j. The multi-body nature of the EAM potential is a result of the embedding energy term. Both summations in the formula are over all neighbours j of atom i within the cutoff distance.

The EAM potential is designed to accurately describe a wide range of properties in metallic systems, such as lattice constants, elastic constants, defect energies and diffusion coefficients. It has been widely used in MD simulations and other computational approaches to study the behaviour of materials at the atomic scale. In this project, interatomic potentials for titanium, developed by Mendelev et al [132], were employed. These potentials are accurate up to 2000 K in one package, producing precise melting point, and results are acceptable at higher temperatures in a separate package.

4.5. Simulation setup

Simulations in LAMMPS were initiated through a script that included instructions for sourcing input information and executing required actions. Consequently, instructions were established to configure the environment and specify the type of calculations, maintaining uniformity across all laser ablation simulations. The script commenced by specifying the unit style for simulations, with the choice of metal units. This set of units were chosen for their suitability in defining unit-based input parameters informing internal conversion factors within LAMMPS. Subsequently, the simulations were defined in three dimensions, aligning with "atomic" style of calculations in LAMMPS to consider relevant attributes of atoms.

Despite a preference for a fixed boundary at the z-axis to capture atom departure from the surface, boundary conditions were set to periodic at all dimensions due to limitations within the original TTM package, restricting conditions to periodic in all directions. After setting these conditions in all simulations, the script defined the size of the simulation box and inserted the atomic system, where atoms were individually defined by coordinates in a 3-dimensional space within the simulation box. For all simulations, a substrate was initially modelled separately and equilibrated at room temperature (300 K), mirroring the planned experimental environment. The simulation box was set 5x larger in Z direction to address the boundary limitation by creating vacuum above the substrates to accommodate the ablated particles. Figure 4.5 depicts a simulation box with an atomic system before laser irradiation.

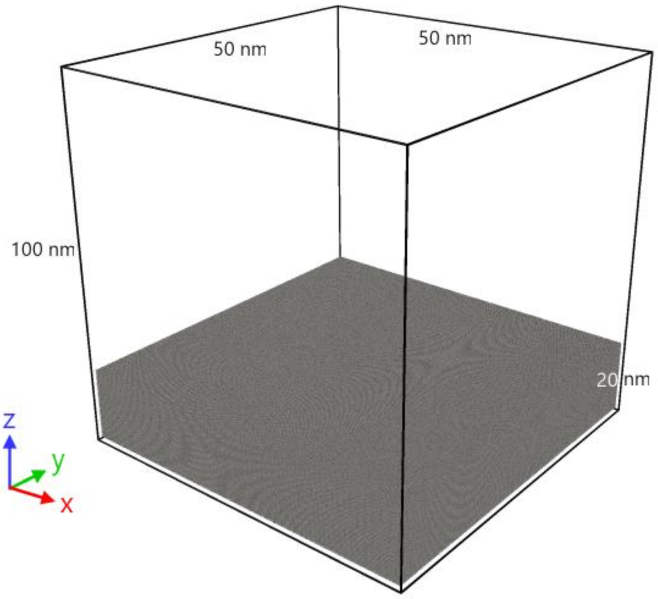

Figure 4.5 - Atomic system containing a single crystal titanium sample with around 3 million atoms.

The equilibration involved the script filling the entire simulation box modelled as the required substrate with atoms, spaced according to the pure titanium lattice. Random velocity values were assigned to each atom and an isobaric-isothermal thermostat (NPT) scaled velocities to equate the temperature of the system to 300 K, considering interatomic energies from the designated potential file. The simulation box at the end with resulting interatomic spacings were stored as the atomic system of pure titanium with the minimum energy at room temperature.

Equilibrating the substrate outside the main simulation aimed to increase time efficiency during the study of various ablation scenarios on an identical substrate. This practice was also necessitated by restrictions imposed by the TTM calculations. To overcome periodic boundary limitations for ablation simulations, the simulation box was defined larger than the substrate in the z-direction. A vacuum above the surface accommodated ablated particles, preventing the periodic wall from returning them to the atomic system from the opposite side. However, this workaround complicated substrate equilibration within a continuous simulation run and inserting an equilibrated substrate into the environment rectified the issue.

After inserting the equilibrated substrate in each simulation run, the electronic grid was initiated with the modified TTM code adding the starting electronic temperatures to the grid overlapping the atomic subsystem. The simulation then commenced by setting the timestep to zero and adding average beam temperatures to the beam profile on the electronic grid for a predefined number of timesteps (350, equal to 350 femtoseconds of laser pulse duration in this project). A modified Langevin thermostat continuously monitored the evolution of the system until the end. Thermodynamic values calculated by the core LAMMPS code were logged, along with a separate file containing the coordinates of each atom in 3 dimensions with corresponding time-averaged temperatures at each timestep for visualisation and post-processing purposes.

4.6. Post processing simulation results

Postprocessing is crucial for extracting meaningful information from the vast amount of data produced by LAMMPS simulations. It transforms raw output into valuable insights, assisting in drawing conclusions, validate models and refine the understanding of the simulated systems. This project focused on examining temperature fluctuations, energy exchange and geometrical disparities across multiple laser ablation processes conducted on titanium samples with diverse characteristics arising from their crystal structure diversity, elemental composition and the techniques employed in their manufacturing. Methods used in analysing the simulation results is explained below.

4.6.1. Temperature profile and probing

The core LAMMPS code is capable of computing various thermodynamic properties throughout the simulation period. In this study, the employed input scripts directed the software to calculate and archive potential energy, kinetic energy, and total energy of the system at one-picosecond intervals. To enhance the granularity of analysis, atoms were strategically grouped in key regions of the sample: the beam spot volume, the remaining substrate, a small cubic volume of atoms directly beneath the laser beam, areas near the surface at all four corners of the substrate and a distinct group near the bottom of the sample.

In addition to energy-related parameters of the entire system, the local temperatures of these designated atom groups were recorded at each picosecond, contributing to a comprehensive dataset for subsequent analysis. Microsoft Excel was the tool of choice for conducting statistical analysis and generating visually informative plots and graphs. This approach allowed for the identification and illustration of trends, patterns or anomalies within the simulation data.

4.6.2. Visual representation

An independent "compute" command was employed to execute a time-averaged calculation of the kinetic energy for each atom at intervals of 1 picosecond. The results were then stored along with atomic coordinates in designated "dump" files. These files served as repositories for visualising atomic movement, tracking geometrical changes, monitoring evolution of melt pools and facilitating temperature and stress calculations among other potential postprocessing actions.

To extract meaningful insights from this stored data, OVITO software was enlisted [133]. This tool enabled further processing, allowing for the generation of snapshots and animations, showcasing numerous configurations and properties. The comprehensive visualisation capabilities of OVITO proved instrumental in unravelling the intricacies of the laser ablation processes on titanium samples, providing dynamic and illustrative representations of the atomic systems over the course of the simulations.

4.7. Experiments

Several experiments were undertaken to compare them to the outcomes of MD simulations, examining the size effect and scrutinising the influence of surface quality and characteristics resulting from the manufacturing techniques employed in fabricating the substrates. The subsequent sections explain the sourcing and preparation of samples, along with details on the ablation setup.

4.7.1. Substrate sourcing and preparation

A titanium plate with high purity of 99.6% (consisting of 99.6% titanium and 0.4% containing carbon, nitrogen, hydrogen, iron and oxygen atoms) was procured from Advent Research Materials in the UK. Initially supplied as a 100 x 100 x 10 mm plate, the material was cut and prepared for compatibility with various laboratory instruments utilised in processing and analysis. The plate was cut into sections measuring 10 x 10 x 3 mm using a Buehler AbrasiMet M saw (see Figure 4.6). To maintain the integrity of the material and avoid any undesirable deformations or heat-induced alterations, an abrasive blade and a continuous flow of coolant were employed during the cutting process. The machine's RPM was set to 2300, accounting for the size of the blade as detailed in the user manual (12-inch blade in this instance), and the federate was manually controlled using a lever. Following the precision cutting, the resulting samples underwent a deburring process using a metal file to eliminate any rough edges and ensure a smooth and uniform finish.

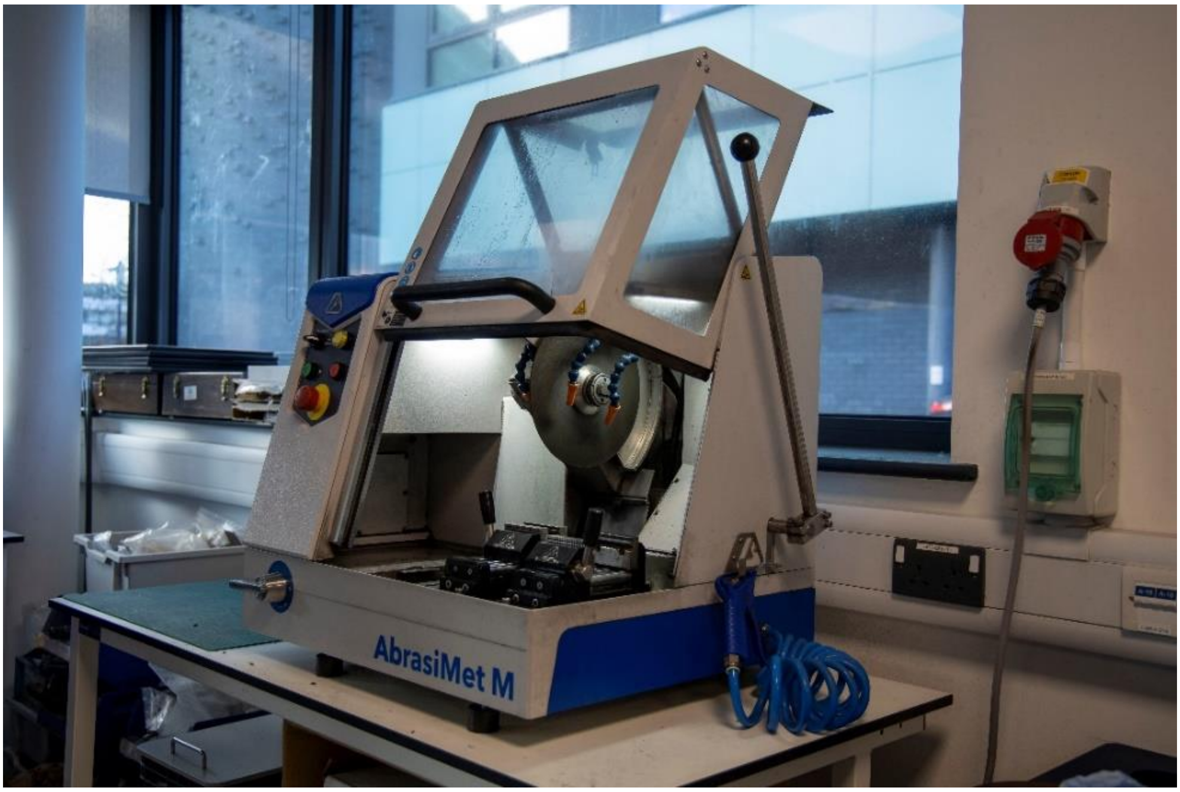

Figure 4.6 - Buehler AbrasiMet M saw used to cut CP titanium samples in material's lab at Warwick University.

Alongside the commercially pure titanium, a 3 mm thick sample with a 10 mm diameter, CNC machined from cast titanium alloy Ti-6Al-4V, was obtained from the fabrication group Xometry UK. Additionally, a corresponding 3D-printed sample, featuring the same dimensions and material, was sourced from the European branch of the same company for the purpose of a comparative experiment. Information regarding the elemental composition and inspection methods employed for manufacturing the samples utilised in these experiments are detailed in their respective certificate of conformity available in the appendix. Surface preparations preceding the laser experiments and data collection were conducted at the Buehler lab at Warwick University as detailed below.

4.7.1.1. Epoxy mount

The samples were moulded in epoxy using a Buehler SimpliMet 4000 machine. Figure 4.7 shows the machine used for this purpose. This moulding process served various purposes, including safeguarding the samples from potential damage and facilitating their handling during subsequent processing steps. Additionally, the epoxy moulding material possessed favourable conductive properties, eliminating the necessity for supplementary treatments such as coating the sample holder with gold particles or using adhesive carbon tapes when scanning samples with a SEM device used for imaging.

Figure 4.7 - Buehler SimpliMet 4000 used to mount all samples at material's lab at Warwick University.

Moreover, the thickness of the moulded samples surpassed the maximum capacity of the XRD machine utilised in this project, which could only accommodate samples up to 5 mm in thickness. However, a minimum thickness of 15 mm was imperative for conducting grinding and polishing with the available equipment. To overcome this limitation, the samples were moulded into pucks with a diameter of 30 mm and a depth of 4 mm. A detachable extension, 25 mm in thickness, was added individually using a metal spacer, one sample at a time. For secure attachment, double-sided tape was employed to connect the samples to their extensions. Subsequently, the extensions were safely removed after the grinding and polishing process was completed. Figure 4.8 shows a prepared titanium sample in epoxy of 30 mm diameter and 4 mm thickness.

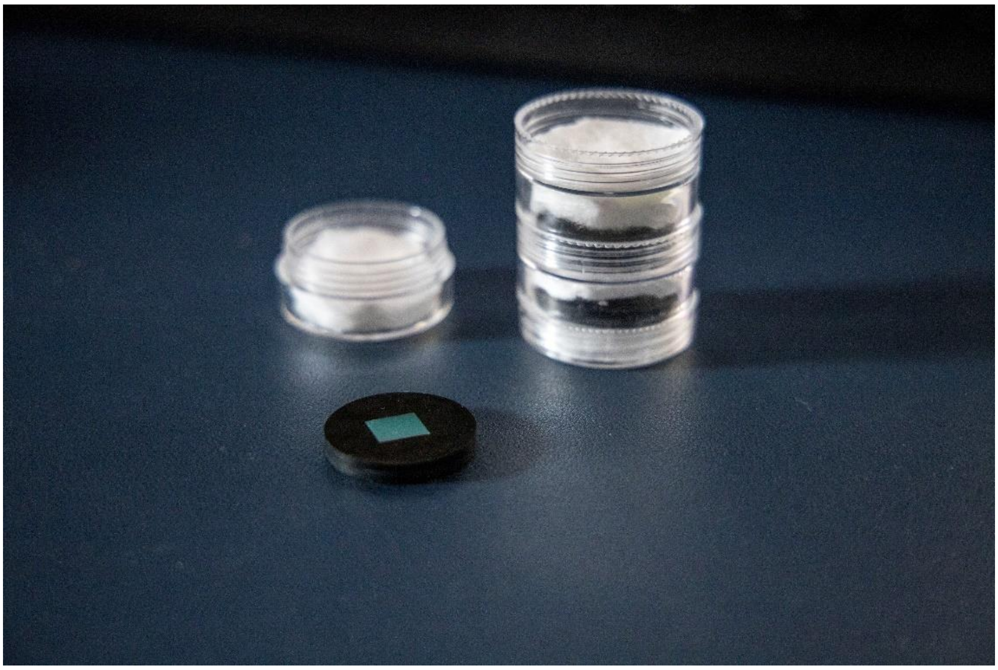

Figure 4.8 - Titanium sample in epoxy mould of 30 mm diameter and 4 mm thickness.

4.7.1.2. Grinding

The surface preparation of the samples was done using a Buehler EcoMet 30. Initially, a 240-grit carbide disc was employed to smooth the surfaces. It was imperative to adhere to a one-minute grinding time with each disc and promptly replace the disc with a new one. This precaution was taken to prevent the risk of contaminating the sample surface with carbide particles, which could potentially compromise the efficacy of the grinding process. Two new 240-grit discs were consecutively used for one minute each before progressing to finer 400-grit discs. Similarly, two discs of finer 600-grit were applied for one minute each to finish the grinding process. Two duplicates of each sample type were prepared, allowing one to be retained as a reference.

4.7.1.3. Polishing

The process of polishing titanium samples is unique compared to most other metals. Initiated with a 9 µm Ultrapad disc and its corresponding suspension solution, the samples underwent a 10-minute polishing cycle. Following this, a 0.05 µm Chemomet disc and its suspension were employed for an additional 10 minutes of polishing. Unlike the typical gradual reduction in grit size for many metals, the unique nature of titanium polishing allows for this relatively swift transition.

To conclude the polishing procedure, the suspension was switched to soap water for a final minute of polishing. It is crucial to acknowledge that given the current state of the technology and the available machinery, the finest attainable surface quality is achieved using 0.05 µm discs and the average roughness value reached for these surfaces was approximately 9 nm ($Ra = 9.19$). An additional sample of CP titanium was prepared and immersed in Tetrafluoroboric acid for a duration of 30 seconds. This specific treatment was undertaken to facilitate the imaging of the crystal structure on the sample's surface using an optical microscope. Figure 4.9 is the machine used to grind and polish the samples.

Figure 4.9 - Beuhler EcoMet 30 machine used to grind and polish surface of all samples at material's lab at Warwick University.

4.7.2. Laser ablation

Samples were ablated using Spectra Physics Spirit® High Power Femtosecond Laser at the Engineering and Materials Lab – University of Oxford, UK. Figure 4.10 is the laser machine utilised in this experiment. Three distinct sample types were incorporated into this experimental study: a sample composed of commercially pure titanium, another fabricated from the casted Ti-6Al-4V alloy using a CNC machine and a third sample of the same material produced through 3D printing. The green laser beam functioning at the second harmonic with a wavelength of 515 nm at 1MHz was employed for ablating all sample variations.

To ensure precision, the height of the laser bed was initially calibrated to align the focal plane of the beam with the surface of each respective sample. Once the settings were established, the laser power was adjusted at four discrete values at four beam spot diameters, as detailed in Table 3.2. The beam spot diameters are derived from the machine parameters, with the displayed values rounded for simplicity. The pulse duration was consistently maintained at 350 femtoseconds throughout the experiments. This duration was deliberately selected as the safest minimum value feasible with the instrument, aimed at enhancing the creation of cleaner craters. To ensure the repeatability of the laser ablation experiment, five spots were ablated at each laser power setting on every sample. These spots were ablated with a 5 µm separation to facilitate subsequent imaging and postprocessing.

Table 4.2 - Laser beam power settings used in the experiment.

Spot ⌀ (nm)	Objective Lens N.A.	Aperture ⌀ (mm)	Beam power #1 (nJ)	Beam power #2 (nJ)	Beam power #3 (nJ)
250	0.95	6.8	2.25	3.375	4.5
500	0.5	8	9	13.5	18
1000	0.3	9.9	36	54	72
3000	0.1	open	324	486	648

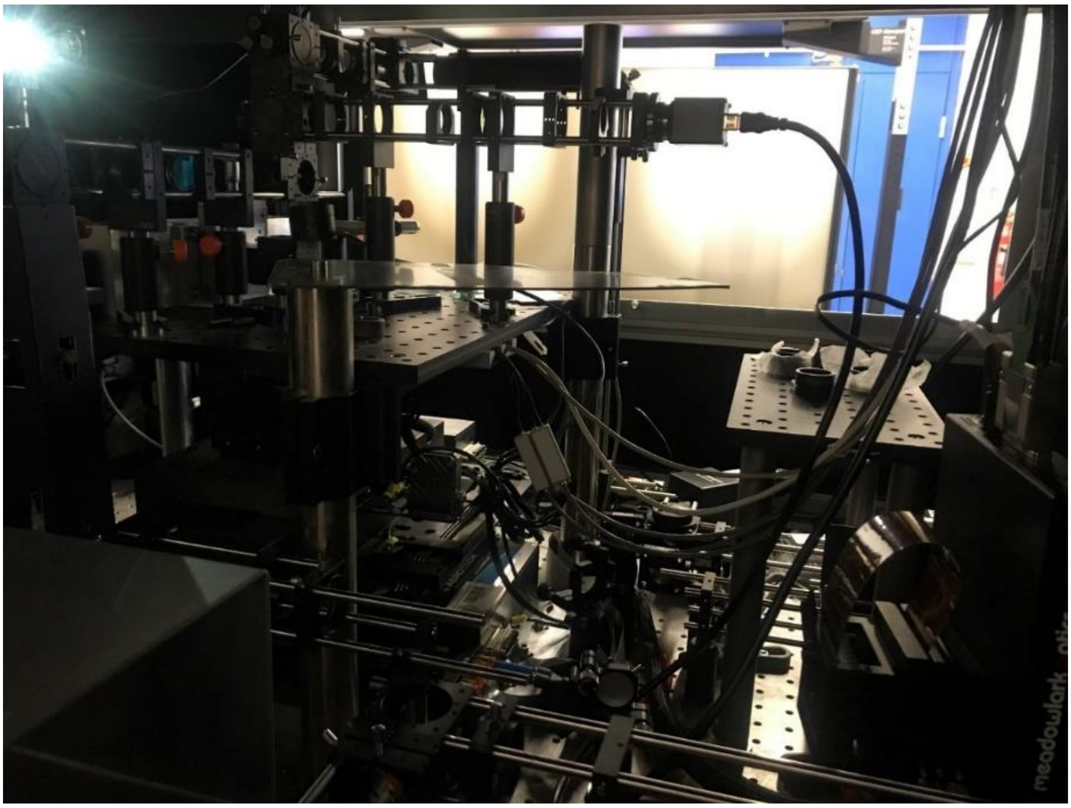

Figure 4.10 - Spectra Physics Spirit® High Power Femtosecond Laser used in this experiment at Engineering and Materials Lab, University of Oxford, UK.

4.8. Data collection

4.8.1. SEM

A scanning electron microscope (SEM) is a type of microscope that produces detailed images of a sample by scanning it with a focused beam of electrons. It is widely used in various scientific and industrial fields for high-resolution imaging of surfaces. Unlike traditional light microscopes that use visible light to illuminate specimens, electron microscopes use a beam of electrons, which have much shorter wavelengths than light, allowing for much higher resolution. SEM images can provide information about the surface morphology of a sample at a very high resolution, making it a valuable tool to study nanostructures and craters resulted from laser ablation.

The prepared samples were scanned using a ZEISS SUPRA 55 VP SEM microscope at London South Bank University prior to ablation for a reference and post ablation for detailed investigation. The chamber was kept under vacuum and the samples were mounted before performing a 1 second scanning passes with the SE2 lens to fine-tune the focus of the device within an appropriate range. Scanning the samples before ablation posed challenges due to the lack of texture on the surface and low contrast for focusing the apparatus. Despite these challenges, preliminary scanning indicated the absence of significant imperfections on any of the surfaces, and no textures exceeded 50 nm in size. Figure 4.11 illustrates a SEM image of the CP titanium sample obtained after preparation.

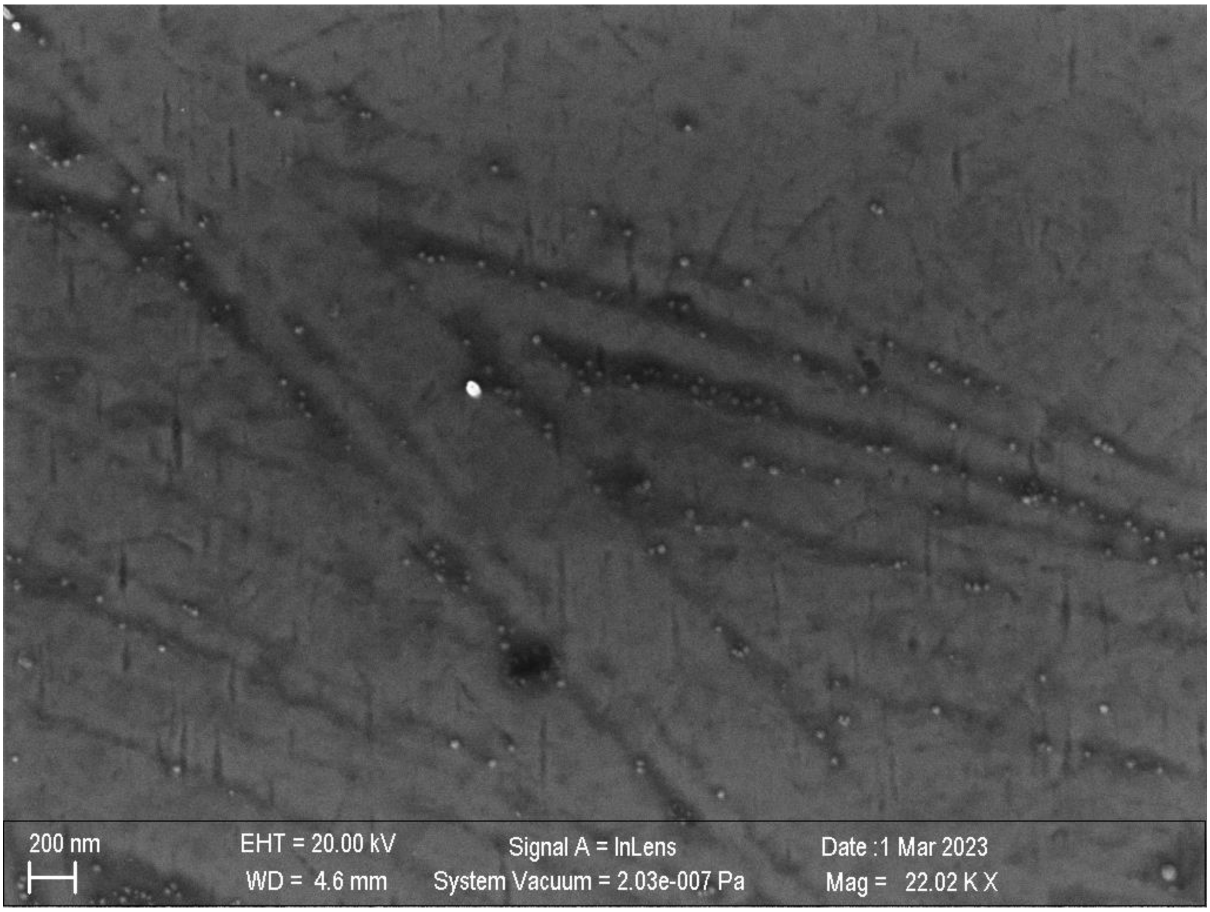

Figure 4.11 - SEM image of CP titanium surface post preparation.

To enhance clarity, fine-tuning was conducted using the InLens apparatus. Subsequently, scanning passes of approximately 21 minutes for each image were executed to gather a series of high-resolution images at magnification of approximately 20,000 times. This comprehensive imaging process was applied consistently for both before and after images, ensuring thorough documentation of the samples. The SEM device used for this work at London South Bank University is shown in Figure 4.12.

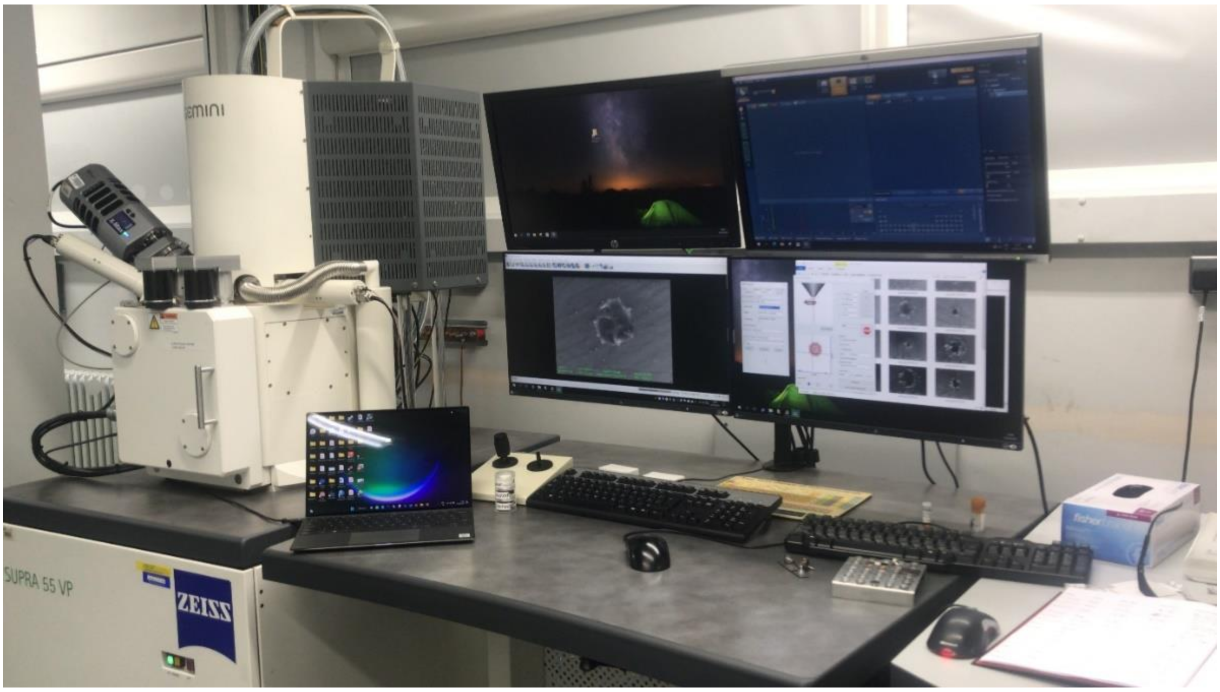

Figure 4.12 - ZEISS scanning electron microscope in the Material's Lab at London South Bank University.

4.8.2. AFM

Atomic Force Microscopy (AFM) is a powerful imaging technique used in nanotechnology, materials science and biology to visualise surfaces at the atomic and molecular levels. It provides high-resolution three-dimensional images by measuring the forces between a sharp probe and the sample surface. The basic principle of AFM involves scanning a sharp tip (usually at the end of a cantilever) across the surface of a sample. The tip interacts with the surface forces of the sample and the resulting deflection of the cantilever is detected by a laser or other detection system. The feedback mechanism adjusts the tip-sample distance to maintain a constant force or distance, producing a topographical map of the sample surface.

There are several modes of AFM, including contact mode, tapping mode and non-contact mode, each with its own advantages and applications. Bruker Multimode AFM in contact mode was used to map the surface of samples after the laser ablation. Then, Nanoscope Analysis software was used to postprocess and extract the required data for this work. Figure 4.13 shows the machine utilised for this project in the Engineering Lab at London South Bank University.

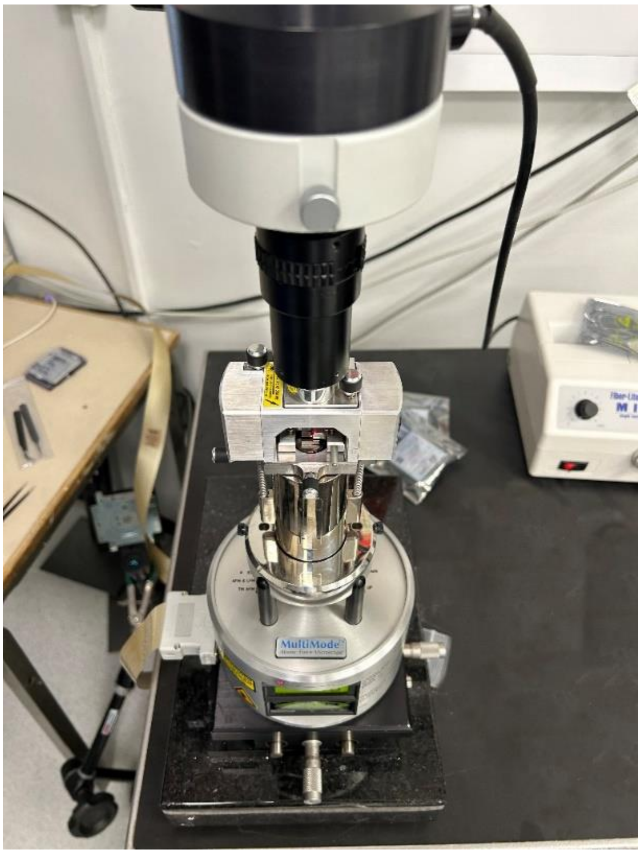

Figure 4.13 - Bruker Multimode AFM device in the Engineering Lab at London South Bank University.

4.9. Summary

This chapter detailed the methodology employed to investigate USP laser ablation through a combination of MD simulations and experiments. This methodology was designed to help better understand the impact of various factors such as the number and size of crystal grains and different beam spot sizes while maintaining identical laser fluence, on craters ablated with single ultrashort laser pulses.

In the MD simulations, crucial parameters, including the beam spot size and crystal grain characteristics were precisely defined. However, it is important to emphasise that these simulations were modelled in vacuum. This simplification, a common practice in MD simulations to streamline computational complexity, has its limitations. The absence of environmental effects, such as the presence of gases and ambient conditions, introduces deviations from real-world scenarios. Moreover, the assumption of material homogeneity at the atomic level and the simplification of laser-material interactions may not entirely capture the intricacies of the ablation process in real-world conditions.

In experiments, various beam spot sizes were tested while ensuring identical laser fluence. Despite rigorous control of experimental conditions, achieving complete control over variables were challenging, especially, maintaining an identical focus plane at the nanoscale. Furthermore, computational constraints and the scale-up of findings presented additional challenges. Simulating larger systems or extending the time scale can be computationally demanding. Despite these limitations, the combined approach of MD simulations and experiments were chosen to provide a comprehensive exploration of USP laser ablation dynamics. This methodology aimed to offer valuable insights into the influence of different parameters on the laser ablation process, acknowledging the intricacies and challenges associated with both simulation and experiment.

Chapter 5 — Comparative analysis of single crystal and nano(poly)crystalline titanium in USP laser ablation using MD simulation

5.1. Introduction

In this chapter, the USP laser ablation of a single crystal titanium substrate was compared to a nano(poly)crystalline sample using MD simulations. Nanocrystalline titanium refers to polycrystalline titanium with nanometric size grains. This small grain size can lead to unique properties and characteristics compared to their coarse-grained counterparts. The production of nanocrystalline materials often involves specialised manufacturing techniques such as Severe Plastic Deformation (SPD), mechanical alloying or other methods aimed at refining the grain size to the nanoscale. SPD methods are the most used methods of manufacturing nanocrystalline titanium. The nanocrystalline titanium produced by SPD methods often exhibits enhanced mechanical properties such as increased strength and hardness as demonstrated by Naydenkin et al [134]. Additionally, the refined grain structure can lead to improvements in other properties like wear resistance and corrosion resistance. However, it is essential to note that the processing conditions and parameters during the manufacturing process play a crucial role in determining the final properties of the nanocrystalline titanium.

Guo et al [135] studied ultrafine-grained pure titanium surface layer produced by Surface Mechanical Attrition Treatment (SMAT). SMAT involves applying mechanical attrition to the surface of a material using a ball milling process. This process can lead to severe plastic deformation of the material's surface layers, resulting in grain refinement and the formation of a nanocrystalline structure. The high-energy impacts from the milling balls induce plastic deformation, breaking down existing grains and promoting the creation of smaller grains. In agreement to the findings presented in this thesis, Guo et al argued that the thermal conductivity of the nanocrystalline surface layer decreased compared to its coarse-grained counterpart.

Nanocrystalline titanium has a range of potential applications due to its unique properties resulting from the nanoscale grain structure. The nanocrystalline form of titanium offers improved mechanical properties, potentially making it beneficial for certain biomedical applications such as implants and prosthetics. It is acknowledged that the properties of nanocrystalline titanium could drastically vary based on the production method and processing conditions. To provide a visual reference, Figure 5.1 is included here, illustrating the arrangement and dimensions of the CP titanium sample utilised for experiments in this study. This image sourced from the surface of the sample that underwent a polishing process and was subsequently immersed in fluoroboric acid for 30 seconds to amplify grain visibility under an optical microscope. As indicated by the scale in this Figure, a laser spot diameter greater than 50 nm impacts multiple grains, contingent upon its incident location. However, it is anticipated that even a minute laser spot will affect multiple grains and therefore, the nanocrystalline form of the same material will exhibit varied characteristics when it is subjected to a laser irradiation compared to this coarse-grain polycrystalline sample.

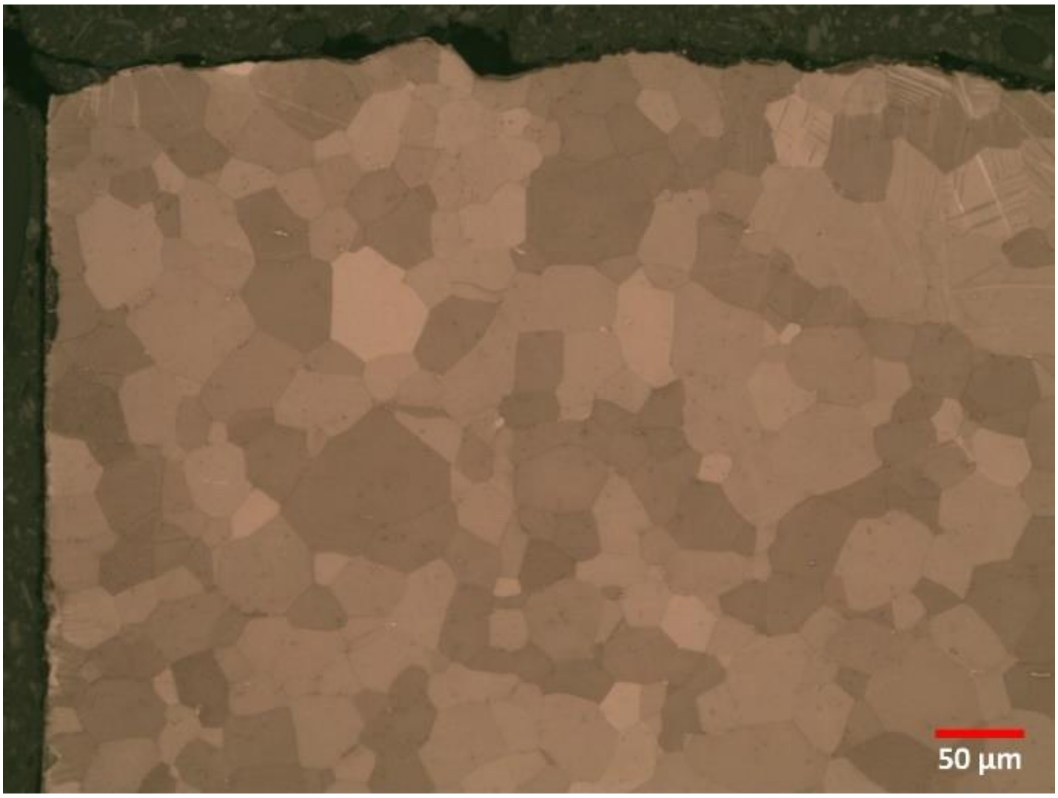

Figure 5.1 – Image of CP titanium sample obtained from an optical microscope.

5.2. Simulation setup and results

To perform the simulations, a substrate measuring 100 nm x 100 nm x 20 nm with alpha-phase titanium lattice parameters was modelled using LAMMPS. This substrate underwent equilibration at room temperature (300 K) to represent a single crystal titanium sample. Additionally, another sample of identical dimensions and lattice parameters was generated, employing a code explained in the methodology chapter to create a Voronoi pattern comprising 2000 random grain sizes and orientations. Subsequently, this atomic system was equilibrated in LAMMPS following the same procedure as the single crystal sample. Figure 5.2 shows both samples side by side after equilibration.

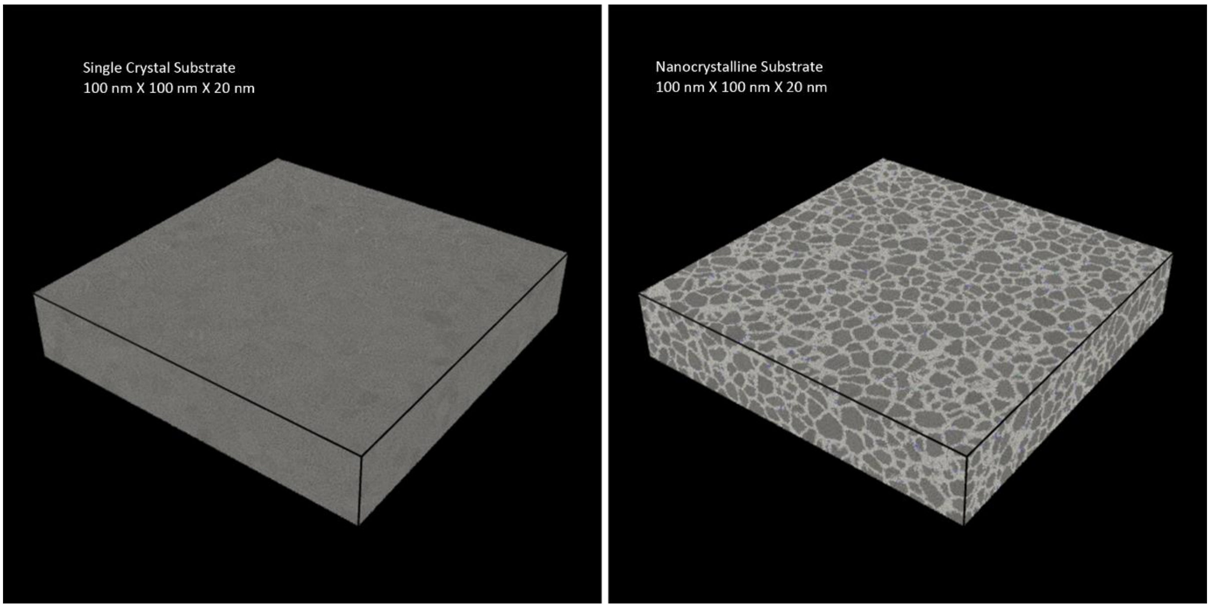

Figure 5.2 - Single crystal and polycrystalline titanium samples equilibrated in LAMMPS.

Both specimens were subjected to 350 femtosecond laser irradiations, featuring a beam spot diameter of 50 nm and an absorbed fluence of 2.2 J/cm^2. The simulations were carried out for a duration of 50 picoseconds. Temperature readings beneath the craters were consistently recorded at every computational step. To capture this data, a cubic region measuring 4 nm x 4 nm x 4 nm, situated 15 nm below the surface, was selected. This region contained 3,711 atoms and was used for these temperature assessments. All the substrates are modelled with identical dimensions and Figure 5.3 shows the location of this region on the cross-sectional view of the models.

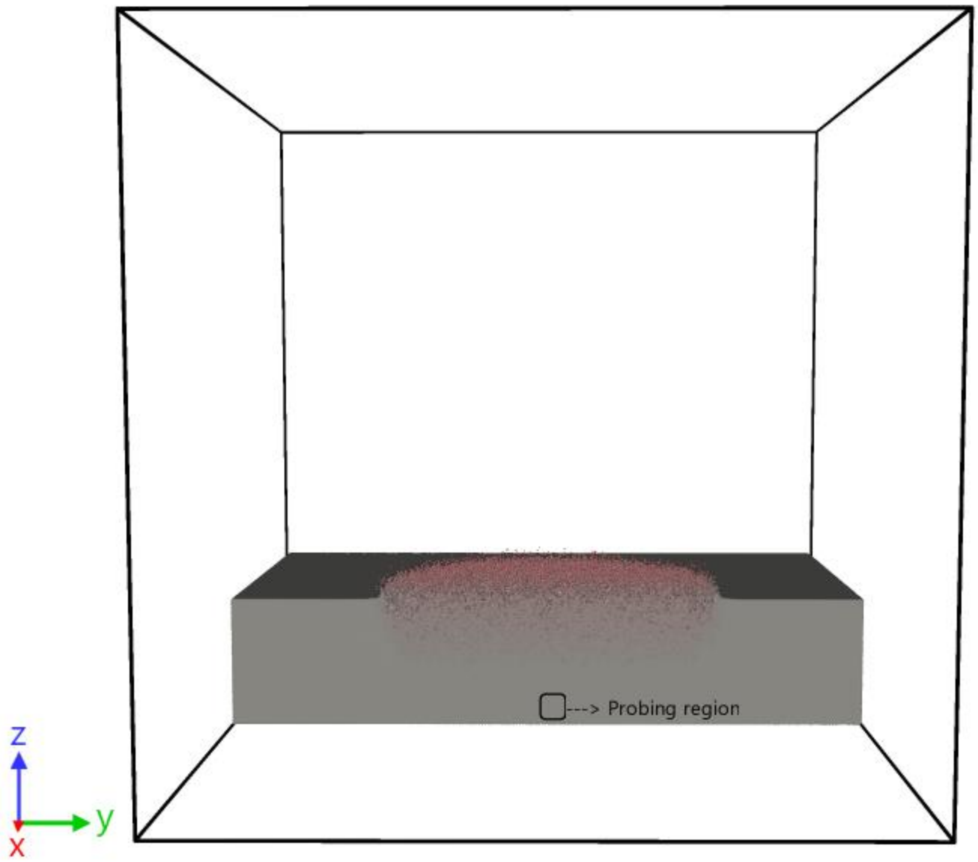

Figure 5.3 - Square shape below the beam depicts the region where temperature measurements were recorded. The red region depicts the beam spot area.

The average plasma temperature and the average temperature measured beneath each crater are depicted in Figure 5.4. The nanocrystalline simulation revealed a reduced energy transfer to the temperature recording site compared to the single crystal simulation. This observation signified lower heat conduction in the nanocrystalline sample as opposed to single crystal titanium. As a result, a greater proportion of the absorbed energy remained confined within the specific volume of atoms in the nanocrystalline arrangement, leading to a diminished transfer of energy to the bulk material compared to the single crystal sample. This finding indicated a slightly higher efficiency in the ablation process for the nanocrystalline material when compared to the single crystal model.

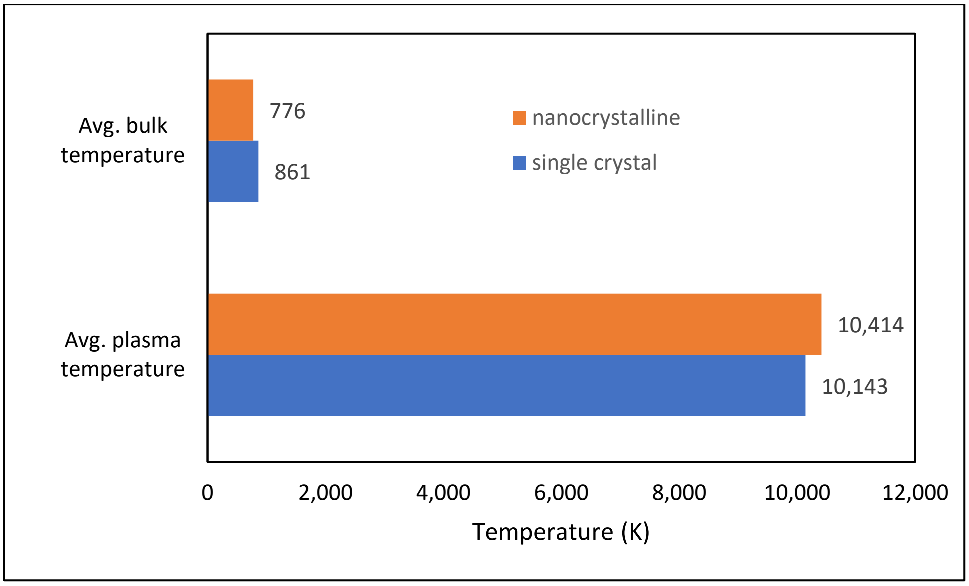

Figure 5.4 - Average plasma temperature and temperatures measured beneath craters after 50 ps simulations.

In Figure 5.5, the result of dislocation extraction algorithm obtained by OVITO software illustrates the cross-section of craters. The graphical representation indicated a smoother crater appearance in the nanocrystalline sample, suggesting a distinct response to the induced stresses. This observation aligned with the discerned lower heat conduction in the nanocrystalline sample compared to the single crystal variant. The distinctive nanoscale grain structure of nanocrystalline titanium introduced complexities in heat transfer mechanisms during femtosecond laser ablation. Grain boundaries, acting as preferential sites for high-pressure phase transformations, influenced thermal energy distribution. This is in agreement with similarities found in silicon nanoindentation study conducted by Goel et al [136]. They compared the response of single crystal and nanocrystalline silicon to nanoindenter and both investigations revealed a commonality in the response of nanocrystalline structures to high-pressure phase transformations.

Consequently, the nanocrystalline sample exhibited localised heat containment, particularly noticeable in the region adjacent to the crater wall. This localised heat concentration induced changes in the original crystal structure of this region. The close connection between nanoscale grain structure and heat distribution in the nanocrystalline sample emphasises the intricate relationship between material characteristics and thermal response during femtosecond laser ablation.

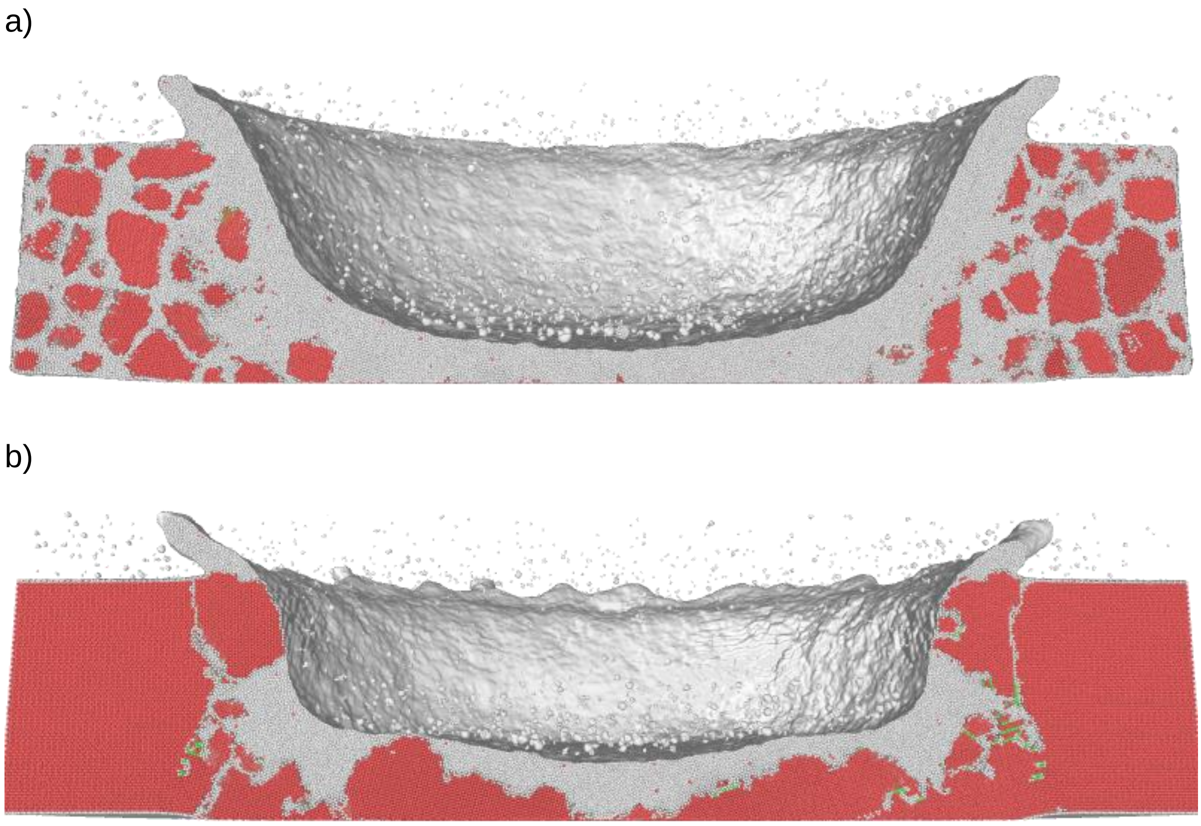

Figure 5.5 – Dislocation extraction algorithm results obtained by Ovito software showing (a) cross-section of nanocrystalline crater (b) cross-section of single crystal crater post laser ablation measuring 20 nm x 100 nm.

While the observed deeper crater in the nanocrystalline sample during femtosecond laser ablation signified enhanced efficiency in material removal, it is essential to acknowledge that this efficiency comes with the trade-off of potential undesired changes in the crystal structure. The localised heat in this case induced alterations in the original crystal structure, especially in the region adjacent to the crater wall. These changes in crystal structure have implications for the properties and performance of the material. In certain applications, maintaining the original crystal structure might be crucial for optimal material functionality. Therefore, while efficient ablation is desirable for material removal processes, careful consideration is needed to balance efficiency with the preservation of the desired material characteristics, particularly in applications where the crystal structure plays a critical role. For example, semiconductor fabrication relies heavily on the precise arrangement of atoms in crystals for the production of devices such as microchips and transistors.

Furthermore, as evident in Figure 5.5, the single crystal crater had a less acute crater wall angle compared to the nanocrystalline sample. This characteristic is desirable in laser processing scenarios where geometrical accuracy is crucial. The smoother contour of the crater walls in the single crystal sample indicated more desirable material removal, contributing to better-defined geometries. However, in applications where precision is paramount, such as microfabrication or device manufacturing, the less acute crater wall angle of the single crystal sample is advantageous. It enables the generation of precise corners that align with the profile of the incident laser beam, as often intended. This highlights the importance of considering specific material characteristics to meet the requirements of laser processing applications.

The results also provided valuable insights into the dislocation mechanisms and structural changes induced by the identical USP laser irradiation. The nanocrystalline titanium sample exhibited a complex dislocation landscape characterised by various dislocation types, including 1/3<1-210>, 1/3<1-100>, <1-100> and 1/3<1-213>. The presence of these dislocations indicated a significant restructuring and deformation. The longer dislocations and higher segment count in the nanocrystalline sample suggested that the smaller grain sizes and the presence of grain boundaries in nanocrystalline titanium contributed to a more intricate dislocation network.

In comparison, the single crystal titanium sample also showed dislocations associated with shear deformation, including 1/3<1-210> and 1/3<1-100>. Additionally, <1-100> and <1-213> dislocations were present, signifying deformation along different crystallographic directions. The dislocation characteristics in single crystal titanium differed from the nanocrystalline sample, with generally shorter dislocations and slightly lower segment count. The absence of grain boundaries in single crystal titanium influenced the dislocation behaviour and resulted in a distinctive dislocation pattern compared to the nanocrystalline counterpart. Figure 5.6 illustrates the resulting patterns and data generated by the postprocessing software.

Both nanocrystalline and single crystal titanium exhibited dislocations associated with shear deformation, emphasising the commonality in the response to the USP laser irradiation. However, the nanocrystalline sample displayed longer and more numerous dislocations, suggesting that the smaller grain sizes and the presence of grain boundaries contributed to a more complex dislocation network.

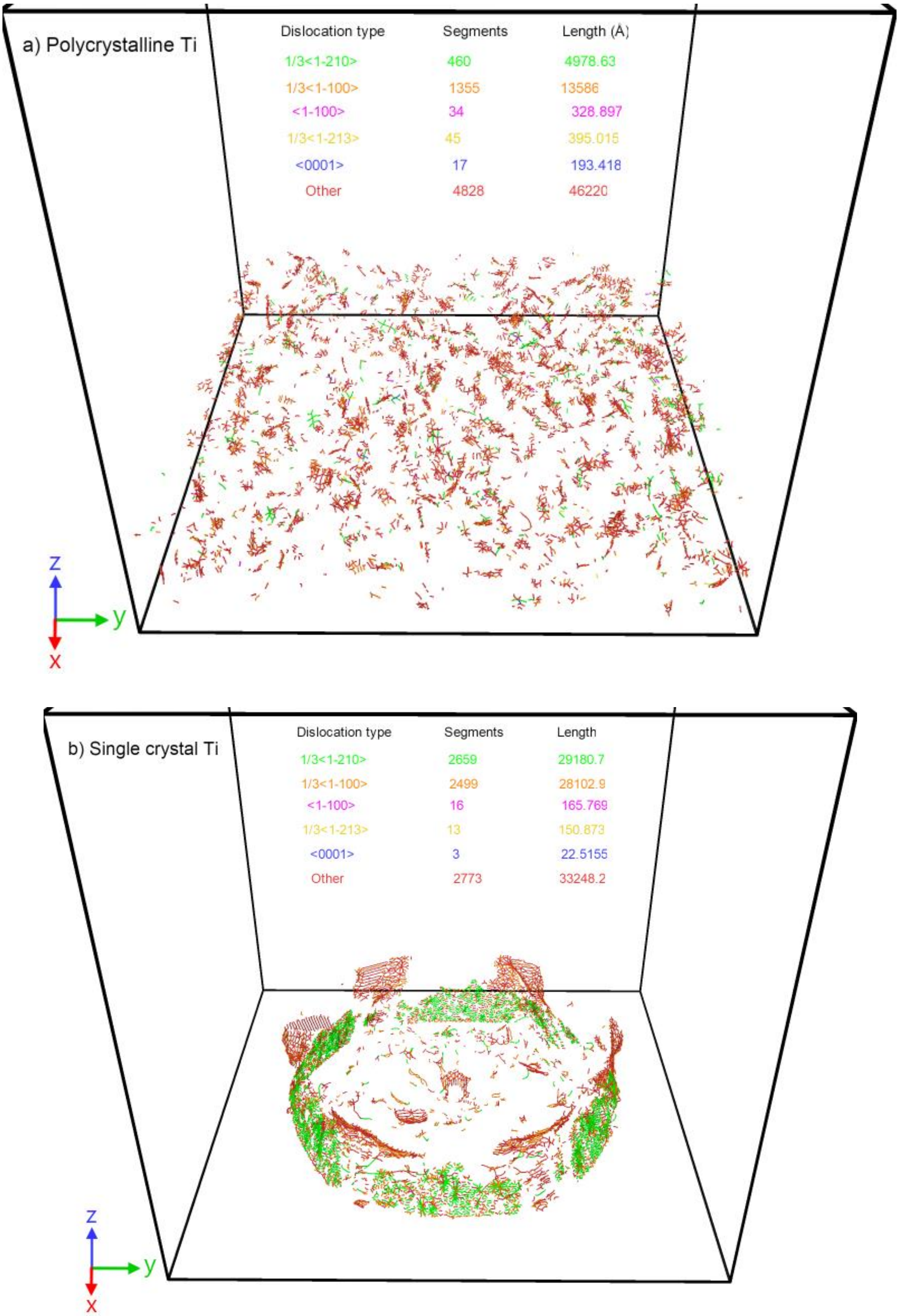

Dislocation type	Segments	Length (Å)
1/3<1-210>	460	4978.63
1/3<1-100>	1355	13586
<1-100>	34	328.897
1/3<1-213>	45	395.015
<0001>	17	193.418
Other	4828	46220

Dislocation type	Segments	Length
1/3<1-210>	2659	29180.7
1/3<1-100>	2499	28102.9
<1-100>	16	165.769
1/3<1-213>	13	150.873
<0001>	3	22.5155
Other	2773	33248.2

Figure 5.6 - Dislocation results of MD simulation of (a) nano(poly)crystalline titanium, (b) single crystal titanium subject to an identical laser pulse obtained by OVITO.

Comparing the results between the nanocrystalline and single crystal titanium samples provided crucial insights about the material removal efficiency, energetic aspects, structural rearrangement and the accuracy of the crater geometries. The higher density and specific types of dislocations observed in the nanocrystalline titanium sample suggested a more effective material removal or structural modification during USP laser ablation. This may indicate a higher efficiency in achieving desired outcomes with less laser energy. The dislocation patterns also offered insights into the energetic efficiency of the ablation process, providing clues about the resulting crater characteristics.

Variations in dislocation lengths and densities shed light on the extent of structural rearrangement in the material during laser ablation. The nanocrystalline sample, with longer and more dislocation segments, undergone more substantial structural changes, leading to a more uniform and smooth crater geometry. Accurate control of dislocation patterns is crucial for tailoring material properties with precision, particularly in microfabrication and precision manufacturing.

Furthermore, the observed dislocation patterns can help in minimising undesirable effects, such as residual stresses or damage, by developing strategies to mitigate these issues. This optimisation process ensures that the final product meets the desired accuracy and quality standards. These findings stress the importance of considering the material's microstructure when assessing the impact of USP laser irradiation, offering valuable information for optimising laser ablation processes in precision manufacturing applications.

Examining the recast layer in both samples, as shown in Figure 5.7, revealed distinct resolidification characteristics post-ablation. In the single crystal sample, the anisotropic nature of the material's resolidification indicated a degree of resistance to the ablation process. This resistance contributed to the formation of a recast layer with rough edges, particularly in regions where the material did not respond uniformly to the laser-induced thermal effects.

In contrast, the nanocrystalline sample exhibited a more isotropic resolidification with a recast layer resulting from a smoother outward flow of material during the ablation. This observation also highlights the significant impact of material microstructure on the overall ablation process and the quality of recast layer.

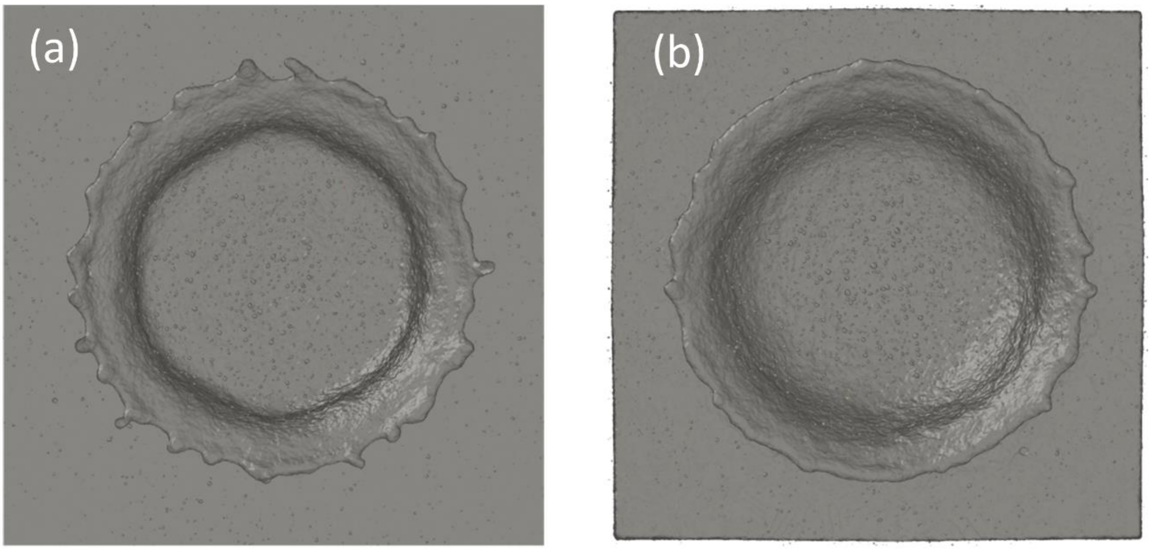

Figure 5.7 - Top view of ablated craters of (a) single crystal (b) nanocrystalline titanium samples measuring 100 nm x 100 nm, simulated for 50 ps, produced by OVITO software.

To demonstrate the extraordinary capability of MD simulations acting as a very high resolution and accurate virtual microscope, a series of snapshots from 1, 3, 5, 10, 25 and 50 picoseconds, as well as the cross-sectional view of the melt pool at the end of the simulations are presented side by side in Figure 5.8. These images involve surface meshing performed by OVITO software to improve visibility and it is remarkable how various details, numerical or visual, can be evaluated with MD simulations. As it is evident on the snapshots, the resulting crater of nanocrystalline sample is slightly deeper with smoother recast layer. These minor differences at this length scale are likely to be influential in determining the precision of desired geometries during manufacturing with direct laser writing of nanoscale textures.

a) Single Crystal Titanium
1 picosecond

Nanocrystalline Titanium
1 Picosecond

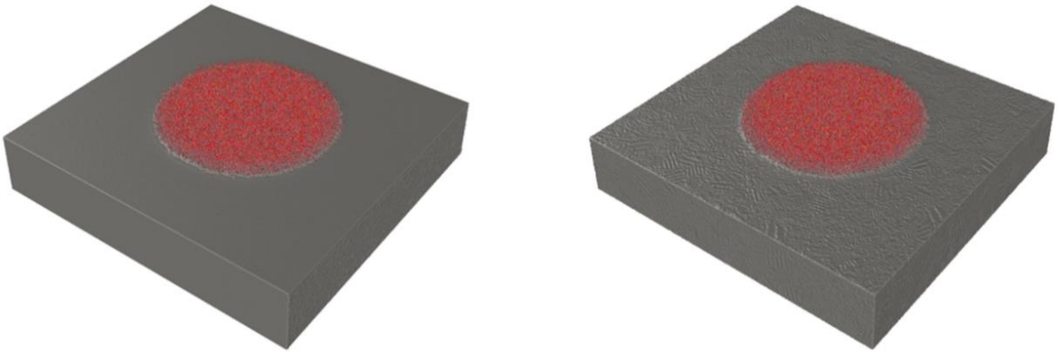

b) Single Crystal Titanium
2 picoseconds

Nanocrystalline Titanium
2 Picoseconds

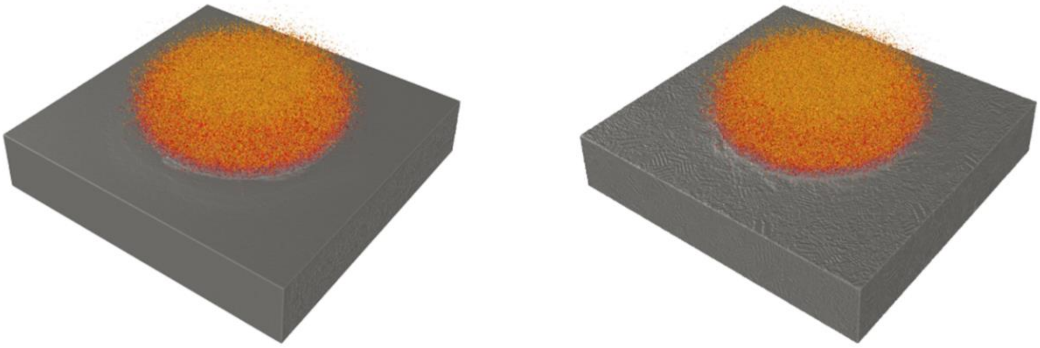

c) Single Crystal Titanium
3 picoseconds

Nanocrystalline Titanium
3 Picoseconds

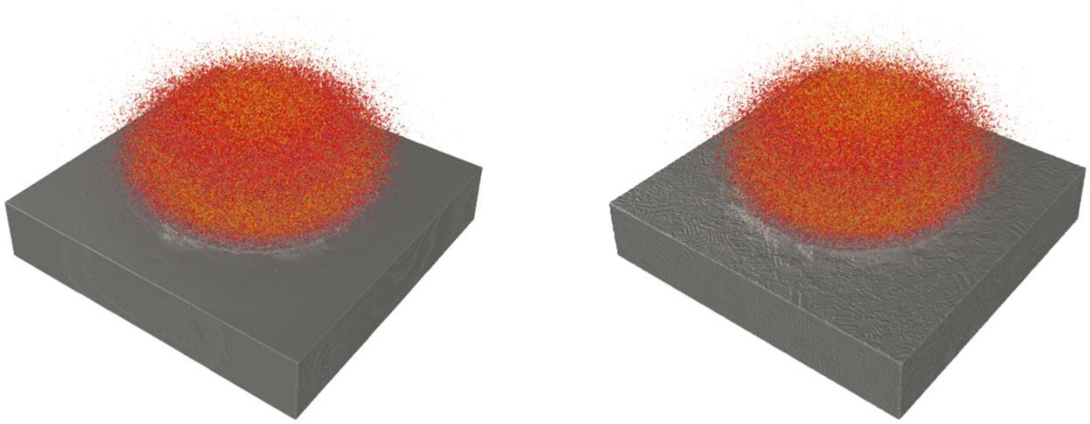

d) Single Crystal Titanium
5 picoseconds

Nanocrystalline Titanium
5 Picoseconds

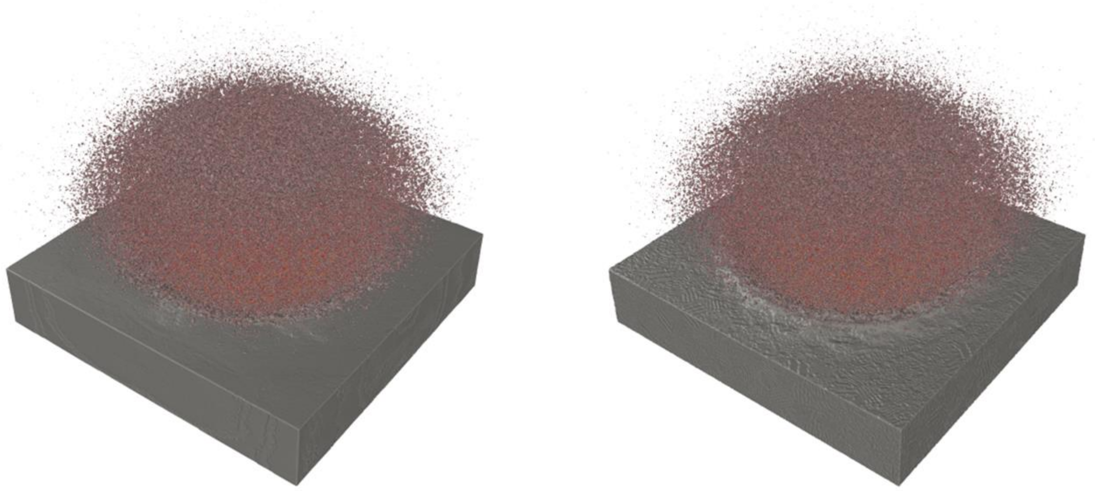

e) Single Crystal Titanium
25 picoseconds

Nanocrystalline Titanium
25 Picoseconds

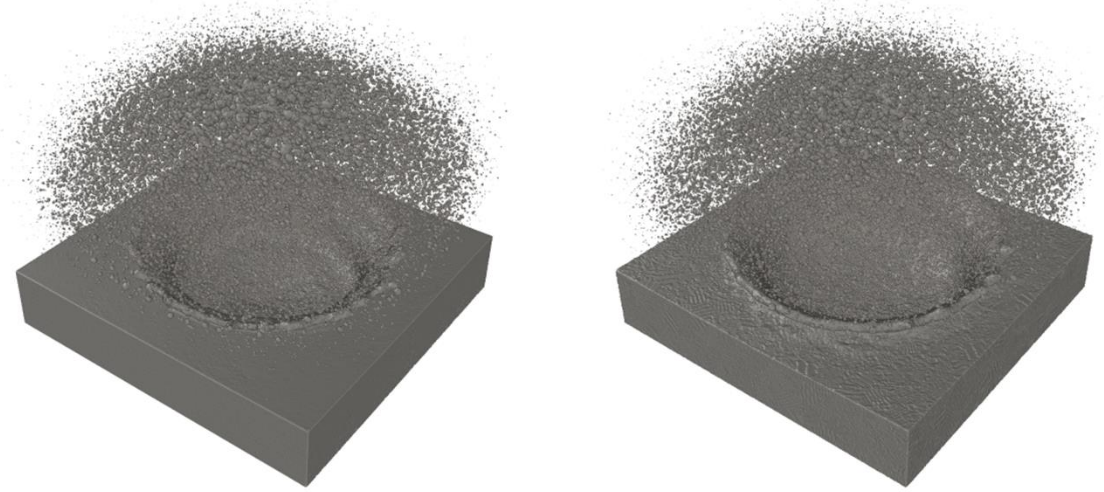

f) Single Crystal Titanium
50 picoseconds

Nanocrystalline Titanium
50 Picoseconds

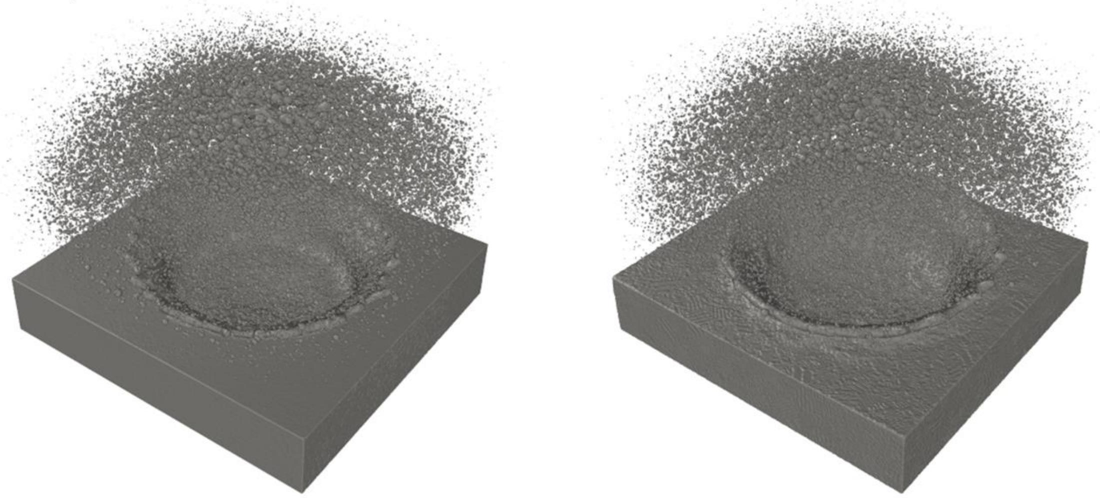

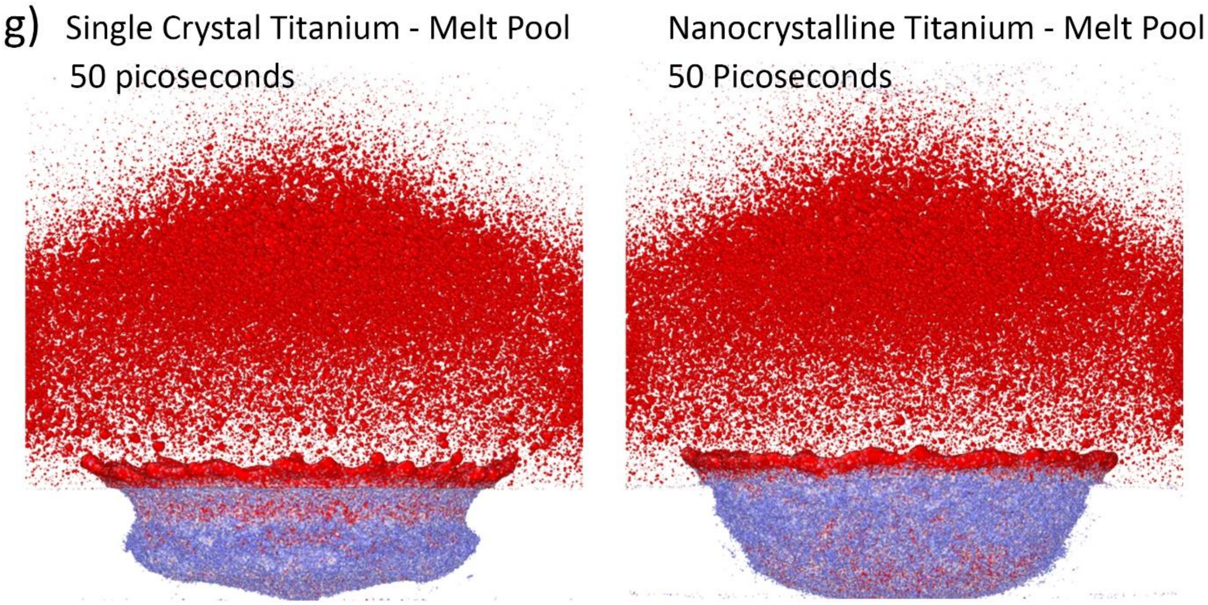

Figure 5.8 - A sequential snapshots illustrating MD simulation outcomes contrasting single crystal and polycrystalline titanium across various temporal intervals: (a) 1 ps, (b) 2 ps, (c) 3 ps, (d) 5 ps, (e) 25 ps and (f) 50 ps. Additionally, (g) captures melt pool formations at 50 ps.

5.3. Conclusion

In conclusion, the comparative analysis of USP laser ablation, as explored through MD simulations, highlighted the varied responses of a single crystal titanium substrate and a nanocrystalline titanium sample to an ultrashort laser pulse. The nanocrystalline titanium, distinguished by its unique nanoscale grain structure, exhibited notable variations in mechanical and thermal properties, aligning with the observations reported by Guo et al [135] particularly, the heat conductivity. The MD simulations showed that the nanocrystalline sample, characterised by lower heat conduction, demonstrated enhanced efficiency in the ablation process with less HAZ compared to its single crystal counterpart, evident in the crater depth and geometry. The anticipated outcome stems from the allocation of additional energy towards forming deeper craters, thereby reducing the energy available for HAZ. The single crystal sample showed more resistance to ablation, resulting in a recast layer with rough edges. In contrast, the nanocrystalline sample experienced a smoother outward flow of material resulting in a recast layer with smoother resolidification. Figure 5.9 illustrates both craters created after 50 ps simulations, providing visual evidence of the differences to support this statement.

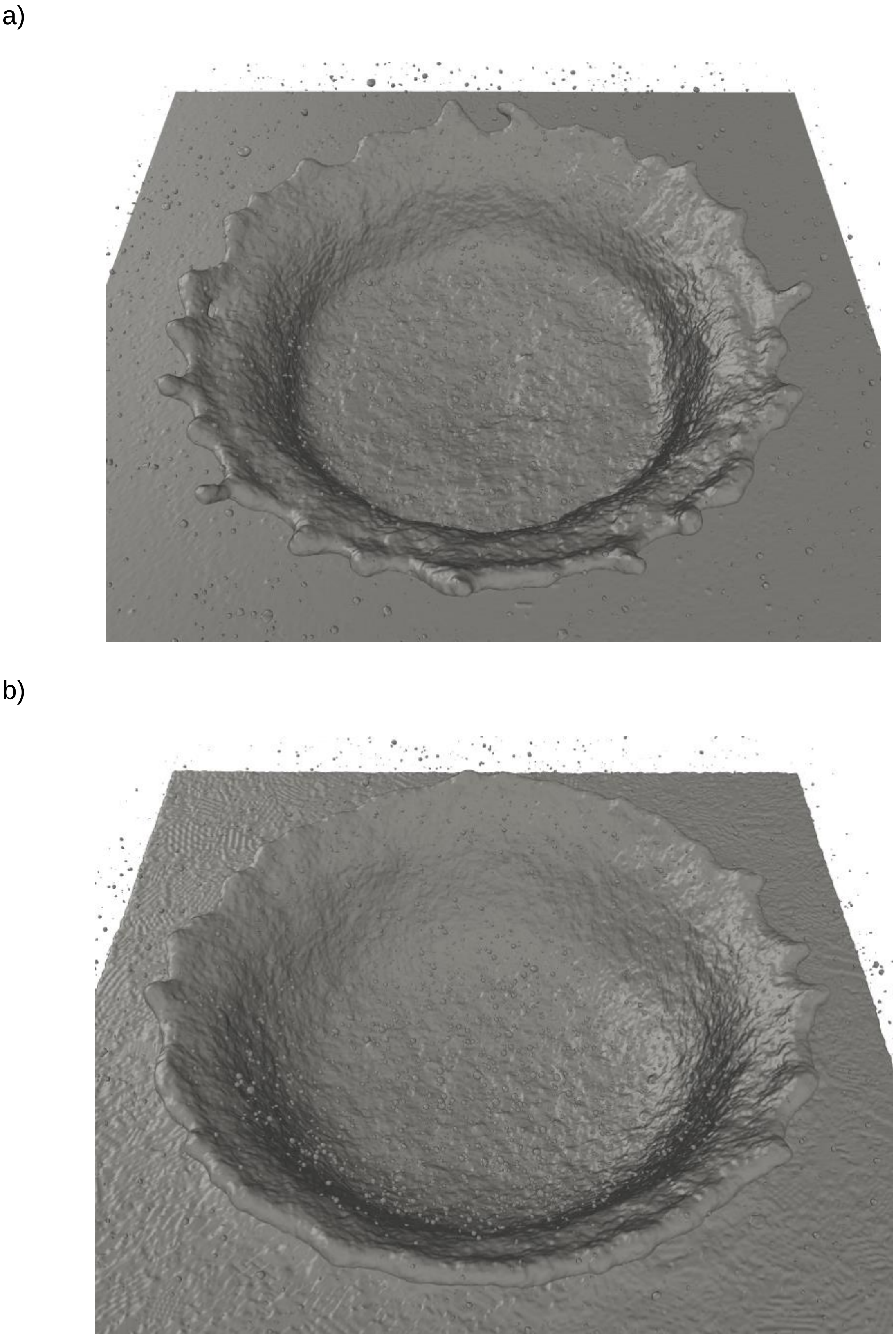

Figure 5.9 – Craters created by MD simulation of laser ablation on the surfaces of polycrystalline and single Crystal titanium samples with an identical laser beam after 50 ps. Both surfaces are 100 nm x 100 nm.

Moreover, the alteration of the crystal structure in the crater wall due to boundary conditions and localised heat during USP laser ablation can be problematic for applications relying on specific material properties associated with the original crystal structure. In instances where mechanical strength, thermal conductivity or electronic response of the material are linked to the crystal structure, alterations near the crater wall can lead to unintended changes in these properties. This can pose challenges in maintaining the desired performance and efficiency of materials engineered for specific applications, such as in electronic devices, sensors or structural components.

Nevertheless, the enhanced efficiency observed in the nanocrystalline sample proves a potential for more controlled material removal processes while ablating larger grains can result in a more accurate crater as predicted by dislocation analysis. The reduced HAZ and smoother recast layer in nanocrystalline sample further enhance the control over manufacturing processes at the nanoscale. In the realm of ultra-precision manufacturing where tolerances are in nanoscale, any improvement in the efficiency and accuracy of material removal processes is highly valuable. The findings from these simulations, offer insights into the microstructural influence on ablation efficiency and surface quality.

Chapter 6 — Experimental results of laser ablation of casted vs 3D printed Ti-6Al-4V alloy

6.1. Introduction

The versatility and increasing popularity of 3D printing of titanium implants in the medical field stem from its ability to craft highly customised solutions tailored to individual patient needs. In medical applications where standardised solutions may fall short, the capacity to produce patient-specific implants becomes crucial. Traditional manufacturing methods often struggle with the complexity of shapes required for certain implants, whereas 3D printing excels in creating these unique geometries, ensuring optimal fit and functionality. Beyond customisation, 3D printing offers sustainability advantages. It operates as an additive process, creating parts layer by layer, reducing waste compared to subtractive processes. This aligns with the growing emphasis on environmentally conscious practices in manufacturing.

Furthermore, the design flexibility enabled by 3D printing allows for the incorporation of specific porosities in titanium implants. This feature is pivotal in promoting superior osseointegration, facilitating bone growth into the implant and enhancing its long-term stability. The process also enables the creation of implants that are not only robust but also lightweight, alleviating overall weight and strain on patients. Innovatively, 3D printing allows the integration of multiple components into a single, cohesive structure. This not only streamlines the manufacturing process but also mitigates the risk of component failure, contributing to the heightened reliability of these implants. The synergy between biocompatibility of titanium and the unique capabilities of 3D printing positions these implants as a versatile, patient-centric and sustainable solution with potential benefits across various medical applications [137,138].

Surface modification is a crucial phase in the postprocessing of 3D-printed implants, playing an important role in determining the long-term prognosis of orthopaedic and dental implants. This significantly influences the overall success of this technology as highlighted by Subramani [139]. The utilisation of USP lasers emerges as a sophisticated technique in this context, offering precision and versatility. USP lasers serve as effective tools for refining and enhancing the surface finish of 3D-printed titanium implants. Their capacity for controlled material ablation and etching proves instrumental in removing excess material and crafting specific surface textures. This capability becomes a strategic asset in optimising implant properties, ensuring the overall efficacy and longevity of parts and facilitating enhancements such as improved osseointegration through the creation of surface features conducive to bone growth. Additionally, the same technology can be harnessed to engineer bactericidal surface structures, addressing concerns related to post-surgery infection control.

This chapter presents the outcomes of experiments designed to investigate the ablation characteristics of Ti-6Al-4V alloy under a single ultrashort laser pulse. The study involved alloys produced using both casting and 3D printing methods, and the resulting craters were systematically compared under identical laser irradiation conditions. The experimental setup involved ablating craters with identical shots on both materials while employing various beam spot diameters. Notably, the examination extended to assess the size effect within each material, since all laser beam sizes were tuned to maintain the same fluence. This approach ensured a comprehensive evaluation of ablation characteristics and size effects specific to each material.

6.2. Characterisation of 3D printed and casted Ti-6Al-4V

The experimental configuration, sourcing samples and preparation methods are outlined in the Methodology Chapter section 4.6. The XRD results shown in figure 6.1 revealed crystallographic disparities between the 3D printed and cast Ti-6Al-4V alloys. The 3D-printed alloy has a tetragonal crystal structure with lattice parameters characterised by c/a ratio of 1.98, while the cast alloy has a hexagonal crystal structure with c/a ratio of 1.59. These variations in crystal structures indicate distinct atomic arrangements, influencing the mechanical and thermal properties of the alloys.

Gorsse et al [140] reported that the distinct crystallographic structures observed between 3D-printed and cast Ti-6Al-4V alloys are the result of their manufacturing processes. In 3D printing, rapid localised heating and cooling lead to quicker solidification, resulting in finer microstructures with smaller grain sizes compared to the slower solidification rates often occurring during casting processes. Additionally, the mechanisms of defect formation during manufacturing, such as not melted and partially melted particles, lack of fusion, and gas entrapment contribute to irregularities in the formed structure of crystals. For example, porosity formed due to incomplete melting or gas entrapment in 3D printing can influence crystal growth and result in variations in crystallographic structures between 3D-printed and cast alloys. Furthermore, the resulting microstructural features, including grain size, grain boundary characteristics, and phase distribution are influenced by the manufacturing process. The rapid solidification process in 3D printing can lead to finer microstructures with smaller grain sizes and more homogeneous phase distributions compared to the microstructures formed in cast alloys. These differences in microstructural features directly affect the crystallographic arrangements within the material, ultimately resulting in the observed disparities between 3D-printed and cast Ti-6Al-4V alloys.

These differences in crystal structures can have notable implications for the response of each material to USP laser ablation. The tetragonal structure of the 3D printed alloy impacts its thermal responses, affecting the temperature at which ablation occurs and the energy required for the process. Additionally, the anisotropic nature of the tetragonal structure may result in directional variations in the efficiency of laser ablation across different crystallographic orientations.

Crystallographic disparities can influence material removal efficiency between the alloys, with variations in atomic arrangements affecting how effectively the material is removed during ablation. Furthermore, differences in crystal symmetry and lattice parameters may impact the ability of the material to dissipate heat generated during the laser ablation, influencing the thermal management of the process.

These structural variations may also contribute to differences in residual stresses and recrystallisation behaviour post-ablation. The distinct lattice structures can lead to variations in the final material state, influencing its mechanical properties. Understanding these effects is crucial for tailoring laser ablation processes to specific material compositions and structures in precision manufacturing applications.

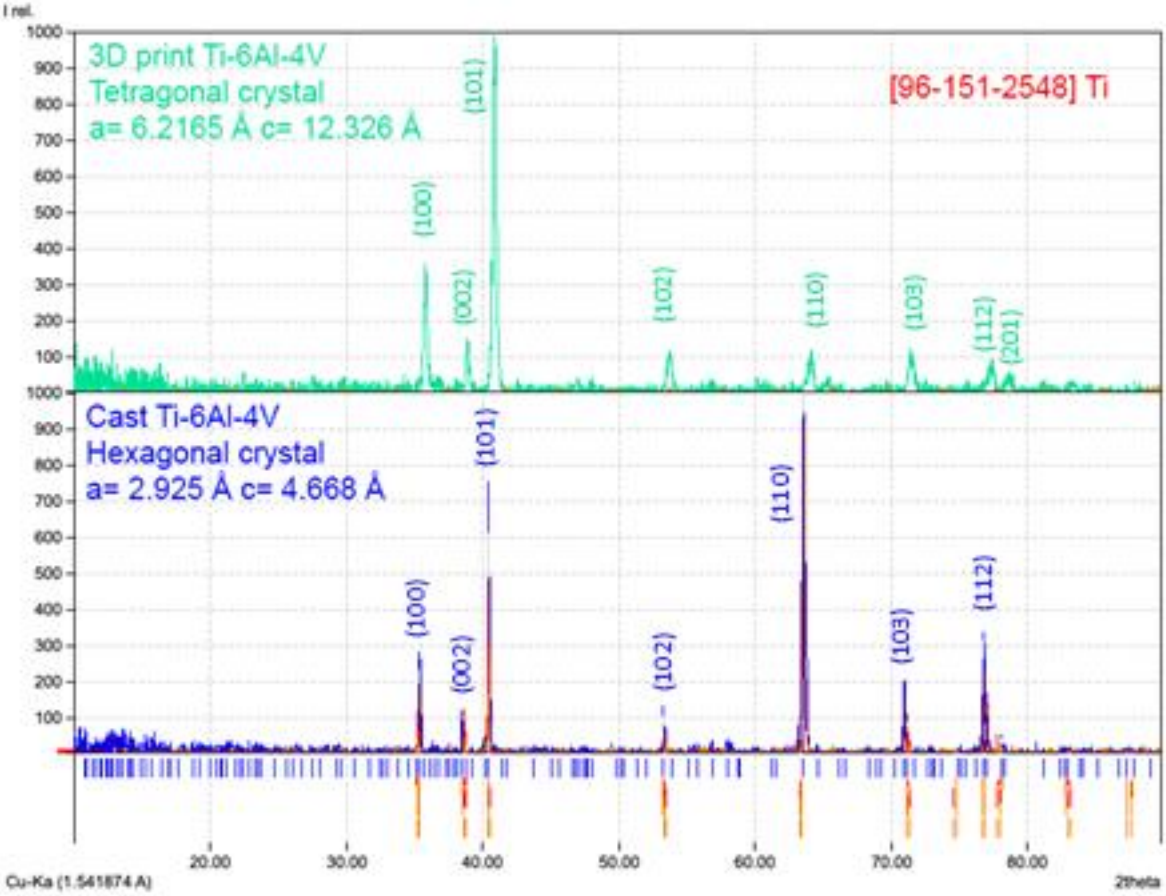

Figure 6.1 - XRD results comparing 3d-printed Ti-6Al-4V alloy to cast material.

6.3. Experiment results

The data collection as well as the SEM and AFM machines utilised are detailed in methodology chapter section 4.7. Here, a comparative analysis is conducted on crater depth, recast layer height and geometry variations among pairs of materials subjected to ablation by laser spot sizes of 250 nm, 500 nm, 1 µm, and 3 µm. The laser fluence and pulse duration were maintained at around 23 J/cm^2 and 350 femtoseconds respectively for all ablations. The selected craters for this comparative analysis are illustrated side by side in Figure 6.2.

a)

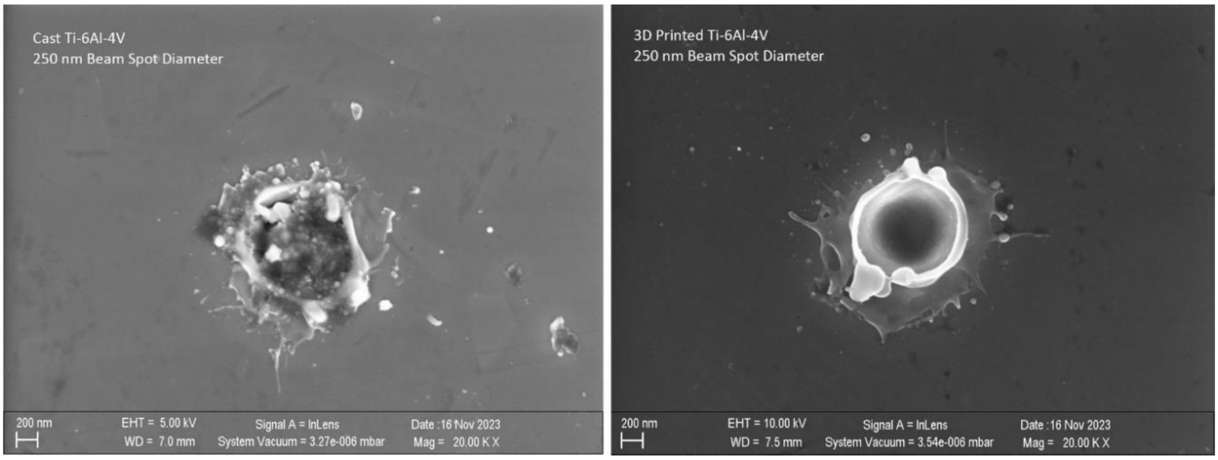
Cast Ti-6Al-4V
250 nm Beam Spot Diameter
200 nm
EHT = 5.00 kV
WD = 7.0 mm
Signal A = InLens
System Vacuum = 3.27e-006 mbar
Date :16 Nov 2023
Mag = 20.00 K X
3D Printed Ti-6Al-4V
250 nm Beam Spot Diameter
200 nm
EHT = 10.00 kV
WD = 7.5 mm
Signal A = InLens
System Vacuum = 3.54e-006 mbar
Date :16 Nov 2023
Mag = 20.00 K X

b)

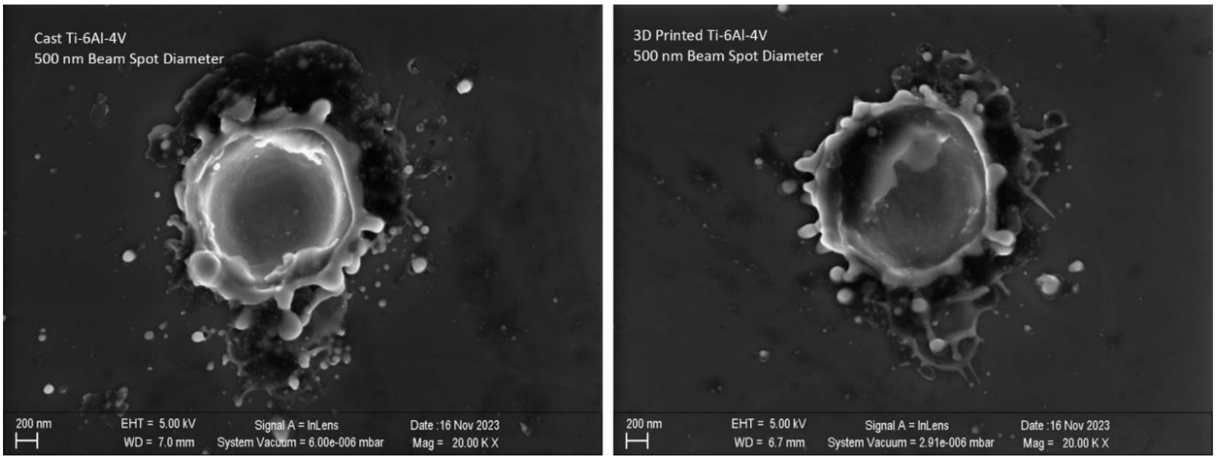
Cast Ti-6Al-4V
500 nm Beam Spot Diameter
200 nm
EHT = 5.00 kV
WD = 7.0 mm
Signal A = InLens
System Vacuum = 6.00e-006 mbar
Date :16 Nov 2023
Mag = 20.00 K X
3D Printed Ti-6Al-4V
500 nm Beam Spot Diameter
200 nm
EHT = 5.00 kV
WD = 6.7 mm
Signal A = InLens
System Vacuum = 2.91e-006 mbar
Date :16 Nov 2023
Mag = 20.00 K X

c)

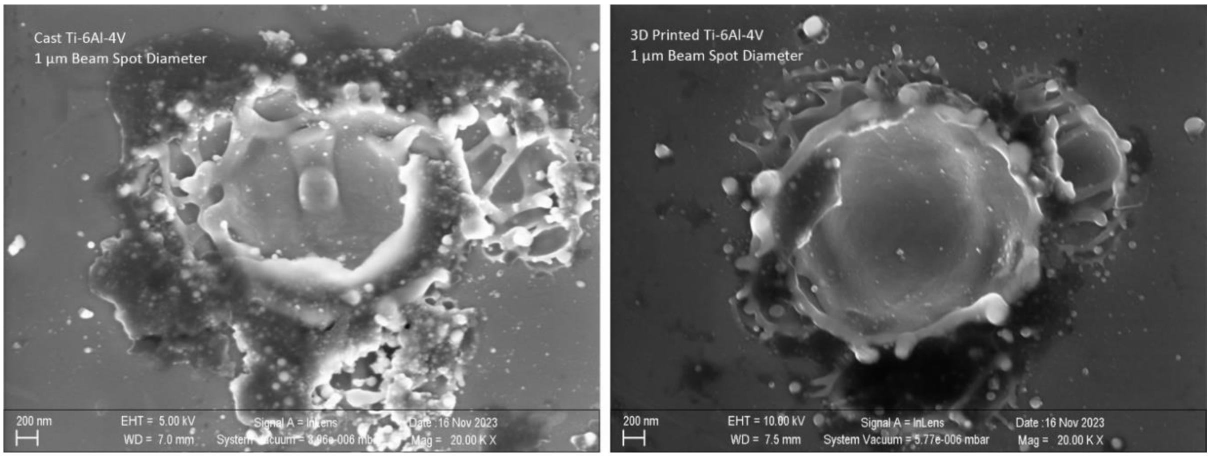
Cast Ti-6Al-4V
1 μm Beam Spot Diameter
200 nm
EHT = 5.00 kV
WD = 7.0 mm
Signal A = InLens
Date :16 Nov 2023
Mag = 20.00 K X
3D Printed Ti-6Al-4V
1 μm Beam Spot Diameter
200 nm
EHT = 10.00 kV
WD = 7.5 mm
Signal A = InLens
System Vacuum = 5.77e-006 mbar
Date :16 Nov 2023
Mag = 20.00 K X

d)

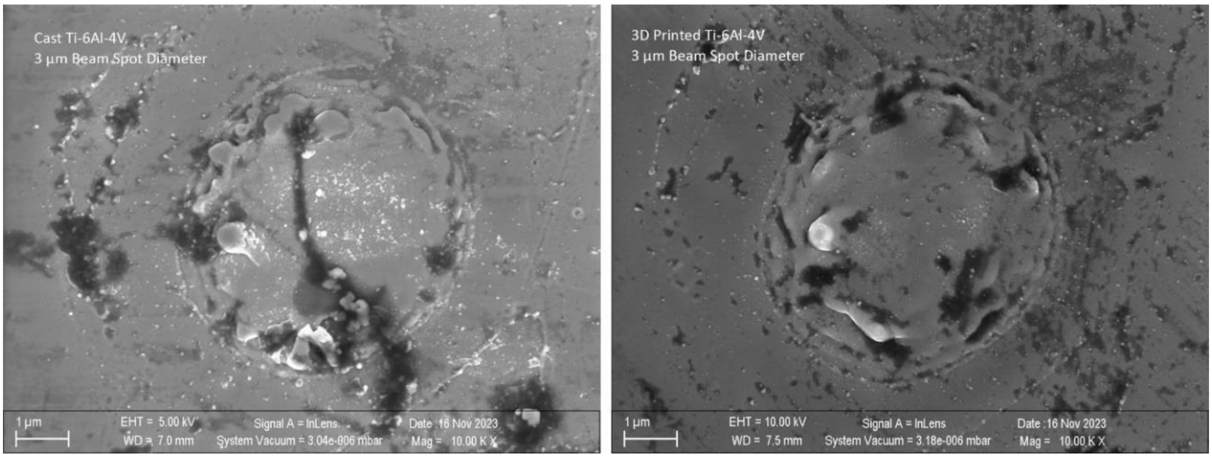

Figure 6.2 - SEM images of cast and 3D printed Ti-6Al-4V ablated by USP laser with beam spot diameters of (a) 250 nm, (b) 500 nm, (c) 1 µm and (d) 3 µm.

The slightly deeper craters observed across the beam spot diameters implied a greater containment of the absorbed laser energy within the targeted volume, leading to increased material removal in the ablation of the 3D-printed specimens. A similar trend was observed in the height of the recast layer. However, the observed variations were minimal and can be argued that they fell within the margin of error associated with the measuring instruments employed for data collection. Visual examination of crater circularity and recast layer resolidification, as depicted in Figure 6.2 indicated a marginal improvement in the cleanliness of the craters formed on the 3D-printed sample. The crater depth and the height of recast layer measured for each ablated spot are detailed in Table 6.1. These measurements were specifically taken from the regions marked by the dotted regions shown in Figure 6.3 for each crater. This specific selection was made to capture the lowest and highest points in each scan, aiming for a representative and consistent assessment of the surface characteristics and facilitate processing a large number of scanned data. The chosen region was assumed to provide a reliable depiction of the material's condition without introducing confounding factors such as contamination, debris or other anomalies that might be present in surrounding areas. This deliberate focus on a well-defined region ensures a more controlled and accurate analysis of the surface features under investigation.

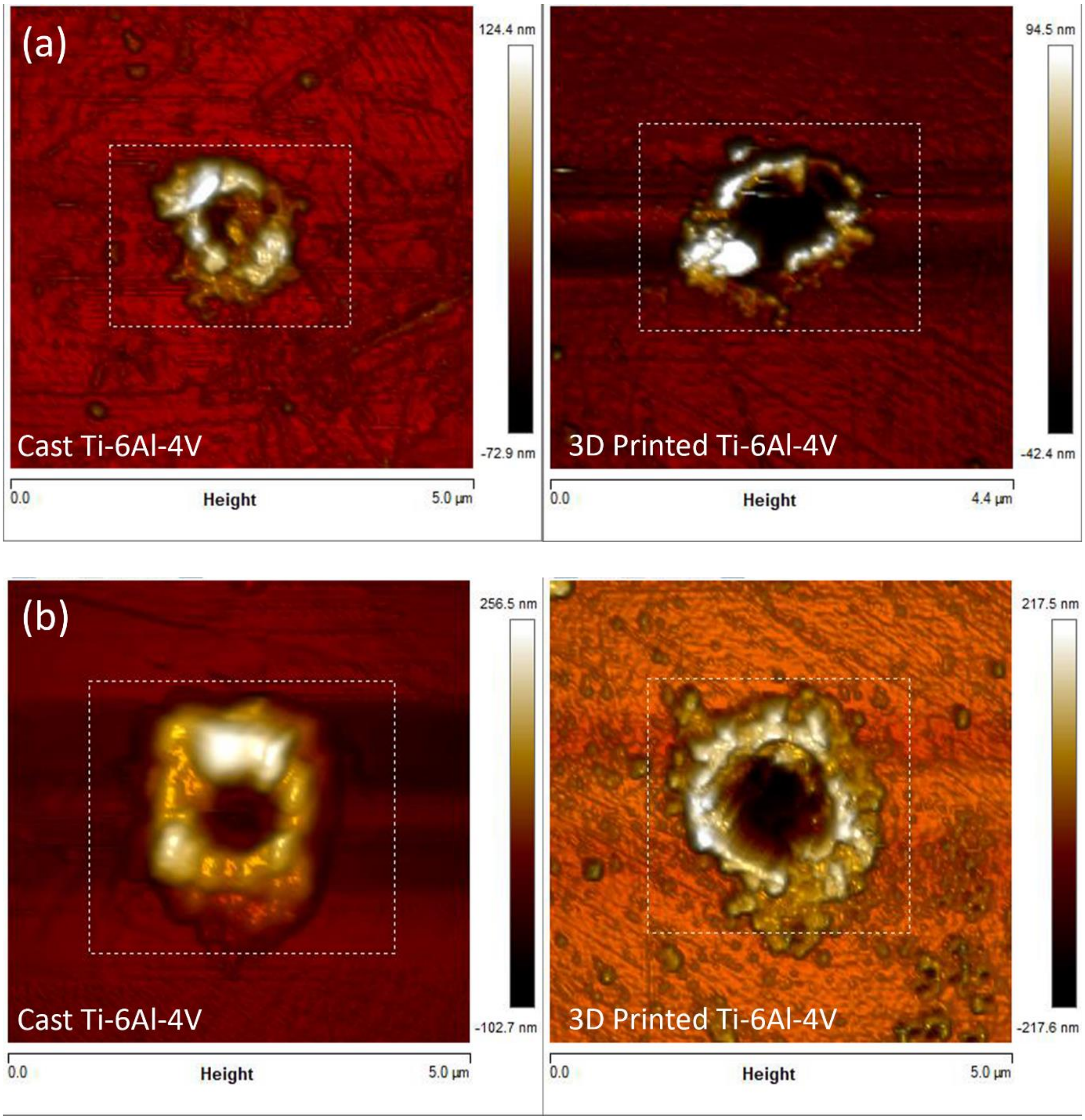
(a)
124.4 nm
-72.9 nm
Cast Ti-6Al-4V
0.0
Height
5.0 µm
94.5 nm
-42.4 nm
3D Printed Ti-6Al-4V
0.0
Height
4.4 µm
(b)
256.5 nm
-102.7 nm
Cast Ti-6Al-4V
0.0
Height
5.0 µm
217.5 nm
-217.6 nm
3D Printed Ti-6Al-4V
0.0
Height
5.0 µm

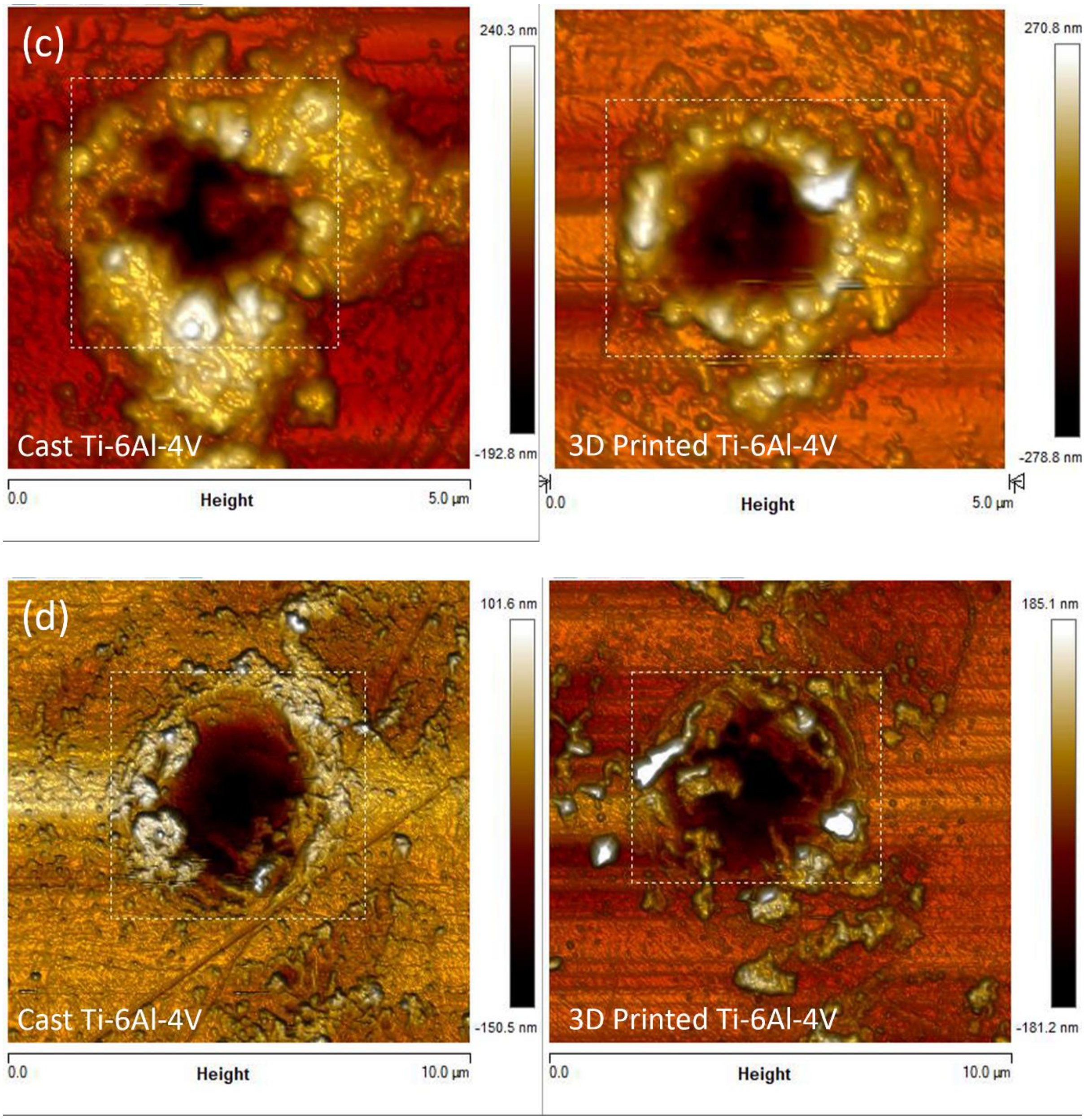

Figure 6.3 - AFM analysis of Ti-6Al-4V samples, cast vs 3D printed surfaces, subjected to USP laser ablation with varying laser beam spot diameters: (a) 250 nm, (b) 500 nm, (c) 1 µm and (d) 3 µm. Data processed using NanoScope Analysis software.

Table 6.1 - Data obtained from NanoScope Analysis software comparing laser ablation of cast vs 3D-printed Ti-6Al-4V alloy.

Material	**Cast Ti-6Al-4V**				**3D-Printed Ti-6Al-4V**			
Beam spot diameter (nm)	250	500	1000	3000	250	500	1000	3000
Crater depth (nm)	172	190	201	192	191	198	205	195
Recast layer height (nm)	150	232	198	55	188	208	200	77

Figures 6.4 and 6.5 provide plotted data illustrating the depths of the selected craters and heights of the recast layers, respectively. The percentage error bars were added to account for and communicate the uncertainty associated with the measurements. The 3D-printed alloy exhibited deeper craters and larger recast layers, indicating a more efficient material removal process compared to the casted alloy. Despite the larger recast layers, the smoother appearance and crater circularity suggested a different material response, possibly attributed to the tetragonal microstructure introduced by the 3D printing method. This efficiency in material removal for the 3D-printed alloy can be attributed to the layer-by-layer additive manufacturing process. The inherent characteristics of 3D-printed materials, such as increased porosity and unique grain structures, can influence the laser-material interaction.

In precision manufacturing, where surface quality and controlled material removal are crucial, finetuning the laser fluence in ablating the surface of 3D-printed alloy could offer advantages. The ability to achieve desired material removal with smoother surfaces may contribute to improved component precision and reduced post-processing procedure.

The conspicuous impact of the size effect was observed up to the 1 μm beam spot diameter in both materials. In another word, as the beam spot diameter decreased, the formed craters were shallower, indicating a heightened ablation threshold. Furthermore, a distinct material response was noted, particularly evident in the size of the recast layer and the decreased depths of the craters when transitioning to the 3 μm beam spot diameter. This suggested a significant alteration in material response, potentially attributed to a more considerable dissipation of laser energy and a subsequent decrease in ablation efficiency.

To gain deeper insights and precisely pinpoint the shift in material response, further examination involving additional beam spot sizes, particularly within the range of 1 to 3 μm, is necessary. Exploring these intermediate values could provide valuable information on the specific point at which the change in material response occurred and where the size effect potentially saturated in each case.

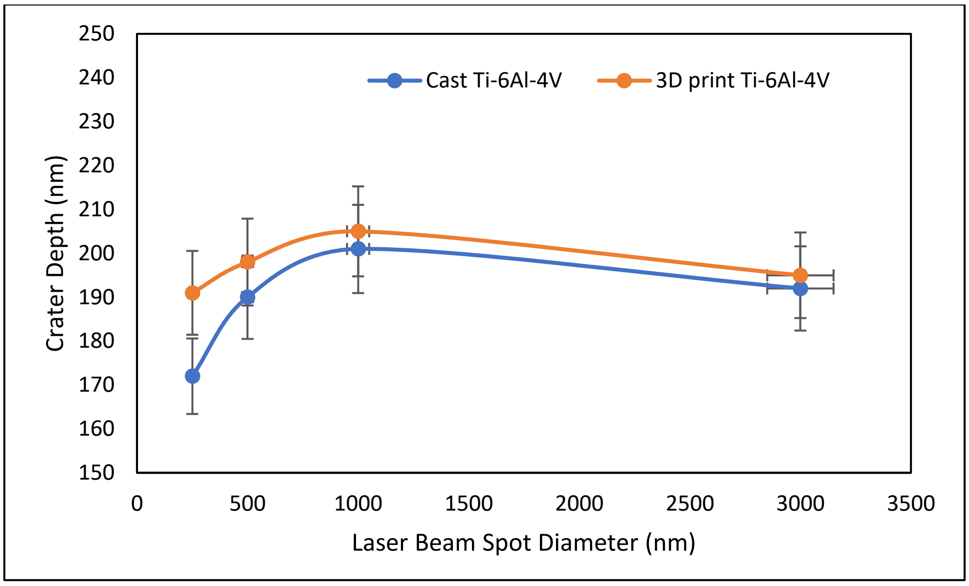

Figure 6.4 – Crater depth as a function of laser beam spot diameter.

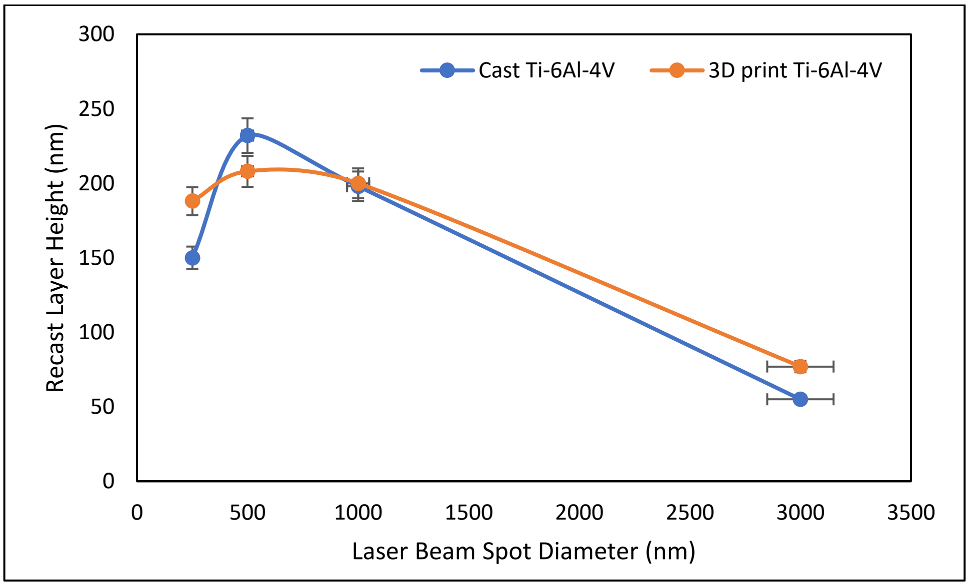

Figure 6.5 – Height of recast layer as a function of laser beam spot diameter.

6.4. Current limitations associated with MD simulations of Ti-6Al-4V

Currently, there are challenges in replicating these experiments with MD simulations. Constructing an accurate simulation setup involves defining complex parameters such as electronic properties, initial material configuration and development of interatomic potentials. A significant constraint arises from the unavailability of a reliable interatomic potential, specifically tailored for the Ti-6Al-4V alloy. MD simulations heavily rely on accurate force fields representing atomic interactions and the absence of a well-established potential for this alloy raises concerns about the reliability of the simulation results.

While the absence of a specific interatomic potential for the Ti-6Al-4V titanium alloy poses a challenge, it is feasible to consider utilising a MD simulation setup calibrated for CP titanium. The use of CP titanium as a surrogate in MD simulations is justifiable due to the transferability of certain material properties across titanium alloys. CP titanium shares fundamental atomic and crystalline structures with Ti-6Al-4V, making them chemically similar. The atomic interactions and responses within the material are often transferrable between these alloys, especially when focusing on common characteristics shared among titanium alloys. Therefore, an MD simulation setup calibrated for CP titanium may capture some essential aspects of Ti-6Al-4V behaviour, providing a reasonable approximation. While this approach involves assumptions and simplifications, it can offer valuable insights into the general trends and response patterns of the alloy.

However, it is crucial to acknowledge the limitations of this approach. The use of a CP titanium simulation setup will not fully capture the alloy-specific nuances unique to Ti-6Al-4V. The distinct composition of the alloy, phase transitions and thermal properties may not be accurately represented by the surrogate material. Therefore, while it is possible to leverage a CP titanium MD simulation setup, the results should be interpreted with caution, recognising that they provide an approximation rather than a precise representation of Ti-6Al-4V.

In summary, while MD simulations present a valuable tool for investigating laser-material interactions, challenges arise in setting up simulations, optimising parameters and the absence of a specific interatomic potential for Ti-6Al-4V. Developing a dedicated interatomic potential for this alloy would require focused efforts in potential function development and calibration. Undertaking such a task is currently beyond the scope of this project, but it stands as a potential avenue for future research. As computational techniques advance, future endeavours could delve into refining the simulation setup to capture the unique properties of this alloy more accurately. This pursuit holds the promise of contributing to a more nuanced understanding of the response of the alloy to USP laser irradiation.

6.5. Discussion and conclusion

As indicated by the experimental findings, the presumption is made that the slightly deeper craters observed in 3D-printed material are attributed to specific factors inherent in the manufacturing process. The tetragonal microstructure and composition, stemming from layer-by-layer synthesis in additive manufacturing, lead to subtle differences in energy absorption characteristics while the surfaces in this experiment were prepared similarly, resulting in an approximately the same roughness ($Ra \cong 9\,nm$) and cleanliness. This enhanced the containment of the absorbed energy within the targeted volume, potentially resulting in slightly deeper craters compared to traditionally manufactured material. Additionally, variations in thermal conductivity between 3D-printed and traditionally manufactured material may have contributed to a localised heating effect, influencing geometric characteristics of craters.

In terms of similarities, 3D-printed and cast titanium both, share a common response to fundamental principles of USP laser ablation, involving energy absorption, heating and material removal. Their shared alloy composition established a foundational similarity in intrinsic properties. This study employed a consistent analytical approach for both materials, focusing on recast layer height and crater depth variations resulting from manufacturing methods used to produce the samples, ensuring a fair and comparable evaluation of their responses.

In conclusion, the experimental study on USP laser ablation of Ti-6Al-4V, manufactured with different methods, has revealed insightful findings. The 3D-printed alloy ($R_a = 32\,nm$) exhibited a more efficient and smoother material removal process, showcasing deeper craters compared to the casted alloy ($R_a = 45\,nm$). Preliminarily, this suggests the potential advantages of 3D-printed titanium alloys in precision manufacturing applications using USP laser ablation. Additionally, the investigation into the size effect demonstrated its pronounced influence up to the 1 μm beam spot diameter in both materials, followed by a sharp decline with the 3 μm spot diameter.

This critical transition point showed a significant alteration in material response, potentially associated with laser energy dissipation and ablation efficiency.

In the future, conducting MD simulations with development of potential functions tailored to the unique characteristics of these materials would offer valuable atomic-level insights into laser-material interactions, aiding in the interpretation of the experimental findings. To expand the investigation of the size effect, a systematic variation of laser beam spot sizes is also beneficial. Exploring the range from 1 to 3 μm and including larger spot diameters could pinpoint the specific thresholds at which material response changes and where the size effect saturates. This would contribute to a more nuanced understanding of the interplay between laser parameters and material response during the ablation process.

Additionally, further material characterisation using Electron Backscattered Diffraction (EBSD) to determine the granularity of the printed sample, could provide insights into the microstructural differences between the casted and 3D-printed alloys. This deeper understanding of grain boundaries, defects and other features influencing laser-material interactions is crucial for refining precision manufacturing processes. Moreover, exploring a broader range of laser parameters beyond fluence, such as pulse duration and repetition rate, could reveal additional nuances in laser-material interactions and their impact on the efficiency of material removal.

Expanding the study to include different titanium alloys commonly used in precision manufacturing applications provides valuable comparative insights into how alloy composition influences laser ablation characteristics. By addressing these avenues for future work, research in USP laser ablation can contribute to a more comprehensive understanding of the laser processing and guide the optimisation of techniques for precision manufacturing applications.

Chapter 7 — MD simulation and experimental results of size effects in USP laser ablation

This chapter highlights the results obtained from MD simulations exploring the size effect phenomenon in femtosecond pulsed laser ablation of alpha phase pure titanium. A series of simulations were carried out to examine various aspects, including the ionic temperature profile, melt pool stresses as well as the depths and geometries of craters resulting from single-pulse irradiation. These simulations were carried out while varying the laser beam spot diameter and later in separate runs, changing the grain sizes. In one set of collected data, substrates measuring up to 50 x 50 x 20 nm, was represented as a single crystal and exposed to an identical electronic temperature rise per unit area in parallel simulations, while varying the beam spot diameter in 4 instances of 10 nm, 15 nm, 20 nm and 25 nm. Due to computational constraints, the substrate size was limited to approximately 3 million atoms. The chosen spot diameters were selected to simulate a range of crater sizes that can produce meaningful results. In another dataset, substrates of identical dimensions were modelled, each containing different number of grains. Each simulation box contained approximately 3 million atoms, and all the other parameters remained identical throughout the simulations.

LAMMPS code including the TTM package was modified to accept an external heat source representing the absorbed laser energy by electronic subsystem. Moreover, the modified code was designed to account for the intricate relationship between local temperature and electronic properties of the material. This consideration is particularly essential in scenarios where temperature variations significantly impact the electronic behaviour of the material [130]. By incorporating this temperature dependency, the simulation is expected to provide a more comprehensive and realistic representation of the material response to varying conditions, thereby enhancing the accuracy and fidelity of the simulations. The EAM interatomic potential for titanium developed by Mendelev et al [132] was employed in these simulations.

7.1. Size effect with varying beam spot diameter

The substate was equilibrated at room temperature (300 K) and was inserted in each simulation to avoid statistical fluctuation of starting temperature. The anticipated outcome was that changes in the laser beam spot diameter would highlight the size effect related response of 4 groups of atoms within distinct beam spot volumes to identical external stimulus. While the beam penetration depth remained constant throughout, a fixed ratio of the total electronic temperature rise to the beam spot area was maintained. To gauge the material response to the laser irradiation, ratio of the increased total energy of the system to the laser beam spot area (absorbed laser fluence) was calculated. Essentially, differences in the energy required to raise the temperature of a unit volume of the material in each simulation served as the evidence of the varying response of the material to the laser irradiation in this case. Table 7.1 displays the initially induced electronic temperature values and outcomes for each simulated scenario. As presented in Figure 7.1, the total energy rise was proportional to the affected atomic volume as expected. The plasma temperature represents the average temperature of atoms in the beam spot volume grouped together over a specified duration of simulations. The temperature of this group was computed at each timestep (1 fs) and the temperatures provided here reflect the average across those intervals during which the kinetic energy of the atoms surpassed the ionisation energy of titanium (~6.8282 eV).

Table 7.1 – Initially induced electronic temperature and results of each simulation comparing laser beam spot size effect.

Spot size (nm)	**Induced electronic temperature (K)**	**Avg. plasma temperature (K)**	**Total energy rise (fJ)**	**Laser fluence (mJ/cm^2)**
10	1.17×10^6	8,979	9.94	12.66
15	2.23×10^6	8,839	20.85	11.80
20	3.79×10^6	9,159	26.91	8.56
25	5.76×10^6	9,353	36.62	7.46

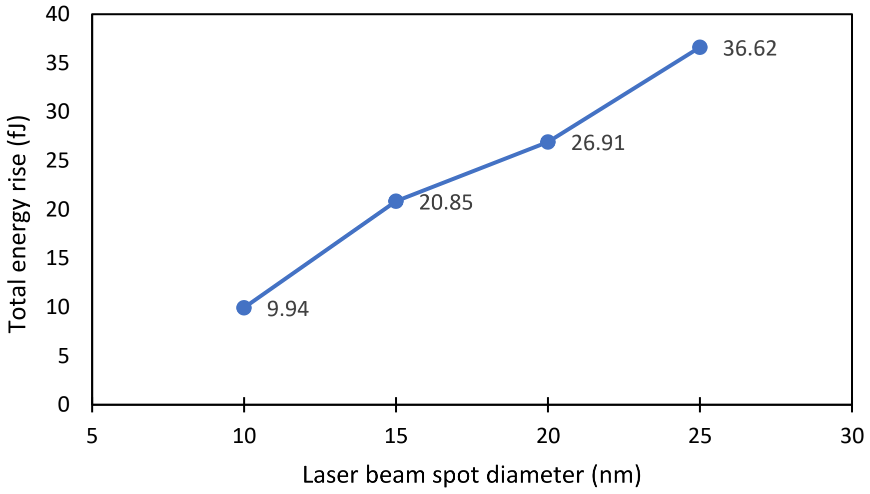

Figure 7.1 - Total system energy as a function of laser beam spot diameter at the end of 50 ps simulations.

Figure 7.2. illustrates the fluctuation of laser fluence of a single 350 femtosecond pulse at the end of the simulation period of 50 picoseconds for each beam spot diameter in calculations constrained by energy conservation. These results indicated that a reduction in the beam spot diameter led to an increase in the energy per unit area required to elevate the temperature of the material. It means that approximately 6 times smaller beam spot area (10 nm spot compared to 25 nm spot) required 1.7 times more laser fluence to produce the unit volume of plasma plume with a similar temperature.

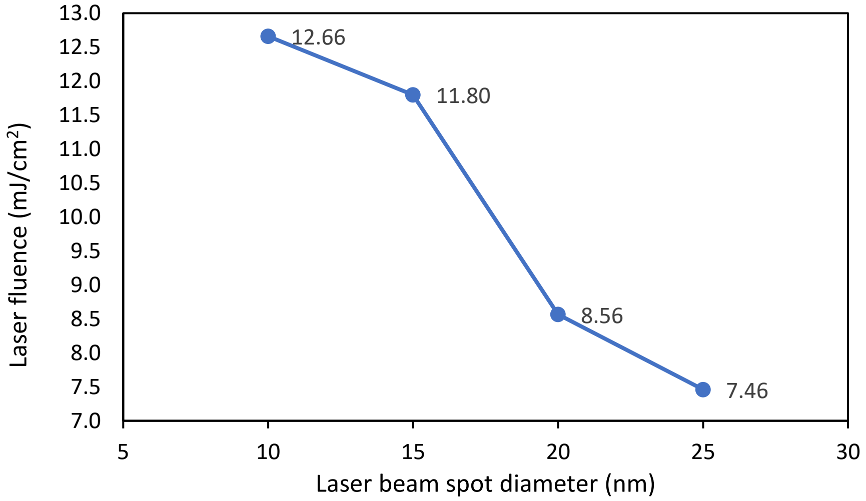

Figure 7.2 - Laser fluence as a function of laser beam spot diameter at the end of 50 ps simulations.

The constraints of the modelling process limited the feasibility of simulating a very small beam spot diameter, such as 1 nm to represent the extreme end of the spectrum. The demands of the simulation software, including grid resolution and precision requirements, posed challenges in accurately representing and analysing processes at such a minute scale. Notably, the practicality of such a small, narrow laser beam is questionable in the real-world context. Even if achieved through beam masking techniques, the likelihood of meaningful interactions with matter is low.

On the other hand, attempting to model excessively large beam spot diameters, like 500 nm, faced hindrance due to computational power limitations. Simulating larger sizes necessitates significantly increased computational resources, making it impractical within the scope of available capabilities. As a result, a deliberate decision was made to push the boundaries as much as possible and select these values for beam spot diameters for the comparisons. This decision stemmed from practical considerations, as it strikes a balance between the modelling limitations at both extremes. While acknowledging that the size effect may be more pronounced at the smaller end and could saturate at the larger end, the chosen approach aimed to capture a meaningful range that was computationally manageable and still provided valuable insights into the size-dependent dynamics without being overly constrained by the extremes of the size spectrum.

The optical penetration depth of the laser beam is independent from the beam spot size. It was observed from the simulations that changes in the beam spot diameter affected the angle of the crater wall. Controlling this parameter holds significant importance in precision manufacturing, particularly when striving for geometric accuracy while employing an USP laser for nano milling. As shown in Figure 7.3.b, the ratio of the angle of the crater wall to the beam spot diameter in these simulations exhibited approximately 30% increase when the beam spot diameter transitioned from 10 nm to 15 nm, 28% increase when it shifted from 15 nm to 20 nm, and 23% increase when it extended from 20 nm to 25 nm.

The ratio of the crater diameter to the beam spot area was almost equally increased in all simulations which suggested that the beam spot size did not significantly affect this parameter (see Figure 7.3.c). However, the thickness of the recast layer and the crater depth, as illustrated in Figure 7.3.d, decreased as the beam spot diameter decreased. Additionally, it was observed that in larger beam spot areas, the bottom of the crater was flattened. This phenomenon may be linked to modelling of the Gaussian distribution of the laser energy at the beam spot volume. It is conceivable that because the standard deviation of the energy distribution was scaled in proportion to the beam spot diameter in the modelling of the beam profile, the region with the highest energy (the hottest area of the spot) was more extensive in cases with a larger laser beam spot diameter. As a result, a larger portion of heat diffusion occurred uniformly in the direction of the beam incidence.

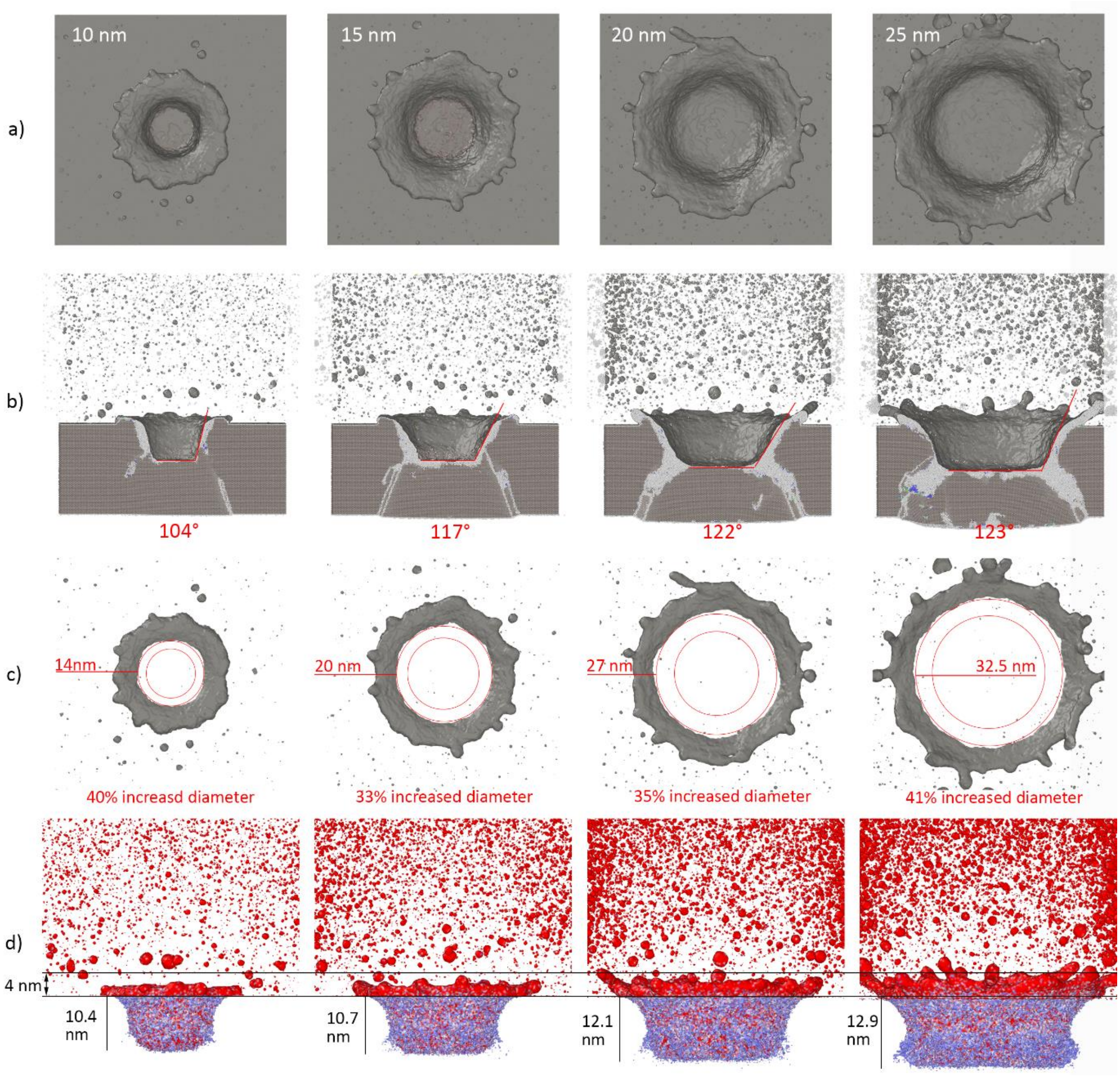

Figure 7.3 - a) Top view of each crater. b) Angle of each crater wall. c) Increase in crater diameter after simulations. d) Crater depths and recast layer thicknesses at the end of 50 ps simulations as a function of laser beam spot diameter.

To assess the heat conductivity of the material, the temperature of a group of atoms located directly beneath the laser beam at an equal depth was measured in all simulations. The exact location of this region is discussed in chapter 5 and illustrated in Figure 5.3. It was anticipated to observe a uniform temperature across all cases due to the constant optical penetration depth. Nevertheless, as depicted in Figure 7.4, the heat conductivity exhibited a progressive increase as the beam spot diameter was enlarged. This observation suggested that heat dissipation was greater in the substrate ablated with the larger spot diameter. As the spot diameter expands, this heightened heat conductivity is expected to expand the HAZ and reduce the ablation efficiency by dissipating more heat to the areas surrounding the laser spot.

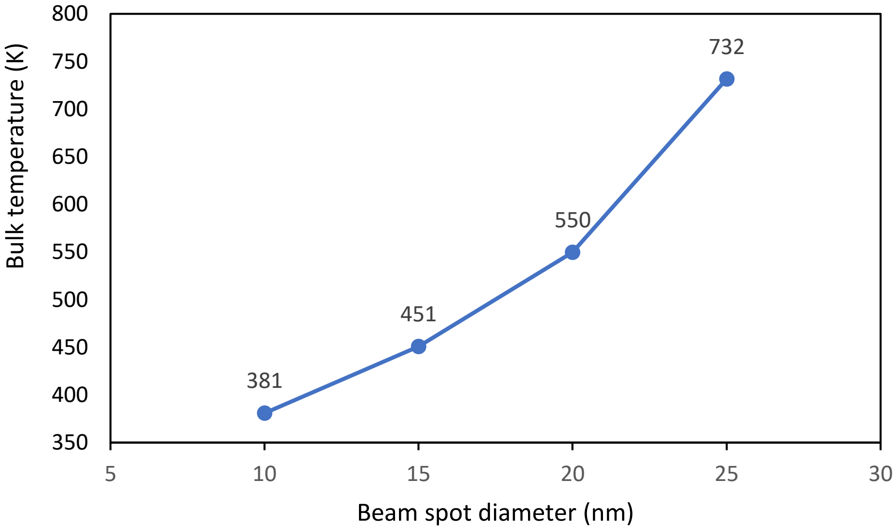

Figure 7.4 - Temperature of atoms beneath craters as a function of laser beam spot diameter at the end of 50 ps simulations.

7.2. Size effect with varying grain size

In the series of simulations, the impact of grain size on the USP laser ablation process was investigated. Consistent volumes measuring 50 nm x 50 nm x 20 nm, each containing 10, 100, 250, and 500 grains were modelled. These models were initially equilibrated at room temperature (300 K) and then subjected to the same external stimulus. The laser beam was introduced into the system as the electronic temperature rise, ensuring uniform energy absorption in all four cases. Throughout the simulations, a constant laser beam spot diameter of 15 nm over 350 femtoseconds were maintained. Figure 7.5 illustrates the overlap between the beam and crater regions with grains on each substrate. The initially induced electronic temperature and simulation results are presented in Table 7.2.

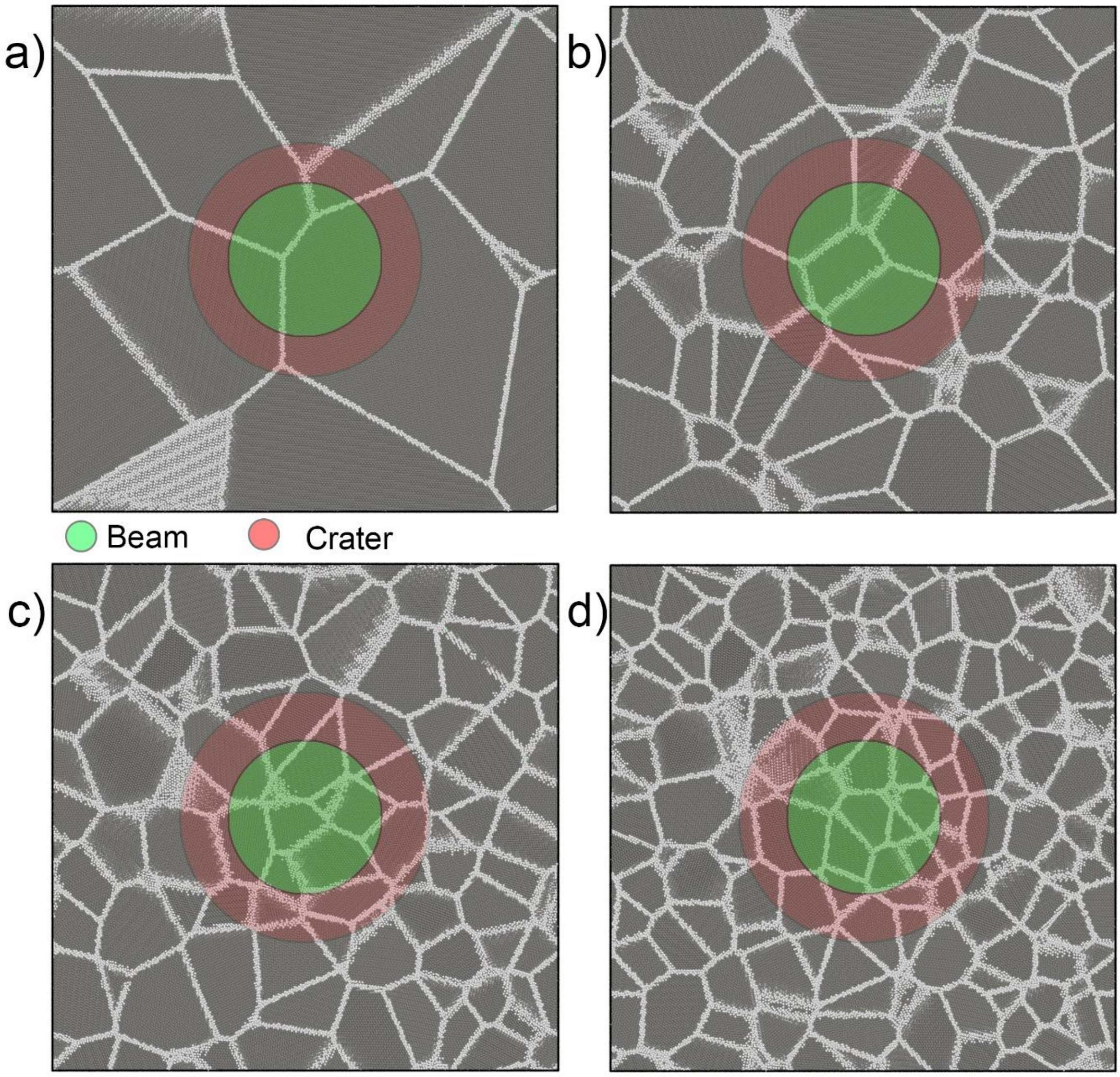

Figure 7.5 - Beam spot and crater regions on substrates with (a) 10 grains, (b) 100 grains, (c) 250 grains and (d) 500 grains.

Table 7.2 - Initial values and results of each simulation comparing grain size effect.

Number of grains	Induced electronic temperature (K)	Avg. plasma temperature (K)	Total energy rise (fJ)	Laser fluence (mJ/cm^2)
10	2.23 x 10^6	9,177	9.40	5.32
100	2.23 x 10^6	9,259	8.10	4.58
250	2.23 x 10^6	9,247	7.27	4.11
500	2.23 x 10^6	9,207	6.88	3.89

The total energy of the system was increased at the end of the 50 picosecond simulations, as detailed in Table 7.2. The results clearly demonstrated a direct relationship between the total energy of the system and grain sizes, with the energy levels rising as the size of grains increased changing from 500 to 10 grains in a constant volume of the material. Figure 7.6 depicts this correlation between energy and grain size. This can be attributed to the decreasing number of grain boundaries as the number of grains reduced, leading to a lower rate of defect flow that demands more energy and increased melting point.

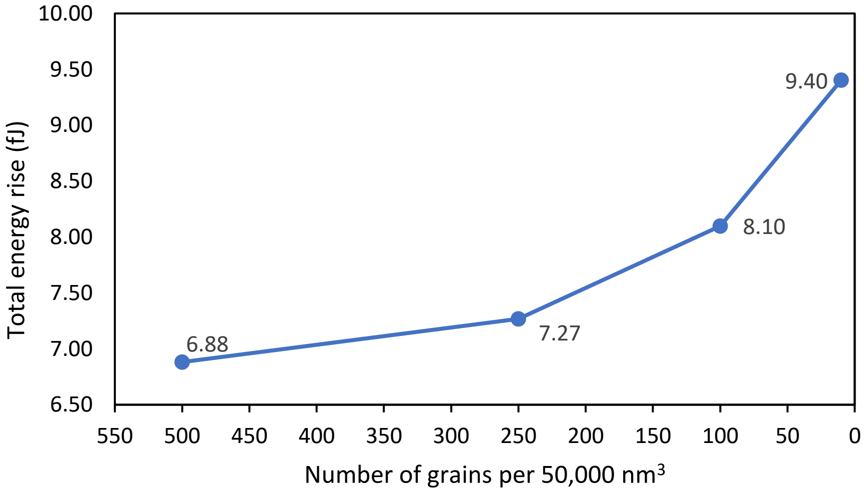

Figure 7.6 - Total energy rise of atomic systems as a function of grain size at the end of 50 ps simulations.

Since the laser spot area was modelled identically in all four cases, the laser fluence curve that is derived from the total energy of the atomic system exhibited a consistent pattern. As shown in Figure 7.7, an increase in grain size led to a 36% rise in the required laser fluence to attain the target plasma temperature, when the number of grains per 50,000 nm³ decreased from 500 to 10.

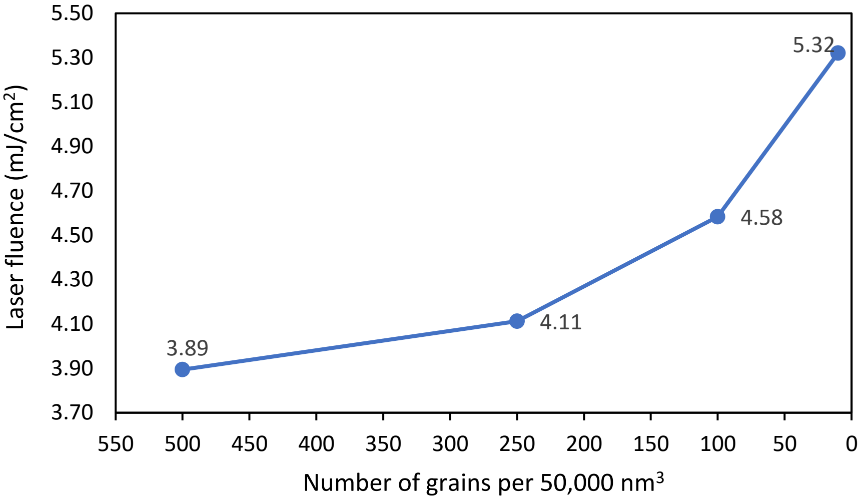

Figure 7.7 - Laser fluence as a function of grain size at the end of 50 ps simulations.

A visual examination of these craters revealed no substantial variations. Nevertheless, it was observed that a larger quantity of grains resulted in a slightly smoother recast layer and increased crater circularity. Figure 7.8 provides a visual representation of these findings.

Furthermore, the grain size appeared to have a slight impact on heat conductivity, as indicated by temperature measurements taken from the bulk of the samples similar to the previous simulations. Evidently, in the sample with larger grains, a slightly higher average temperature was recorded. This could be attributed to increased heat conductivity due to fewer grain boundaries. Figure 7.9 displays these recorded temperature measurements. The influence of grain boundaries in reducing the heat conductivity has been previously discussed in MD simulations comparing single crystal and polycrystalline titanium. In these simulations, the differences in microstructure, grain boundaries and crystal orientations between single crystal and polycrystalline samples affect the heat conduction pathways. The increase in grain boundaries in polycrystalline materials introduces additional scattering mechanisms for heat carriers, hindering the overall heat conduction. This phenomenon has implications for the thermal response of materials under laser irradiation and contributes to variations in the ablation process observed in different microstructures.

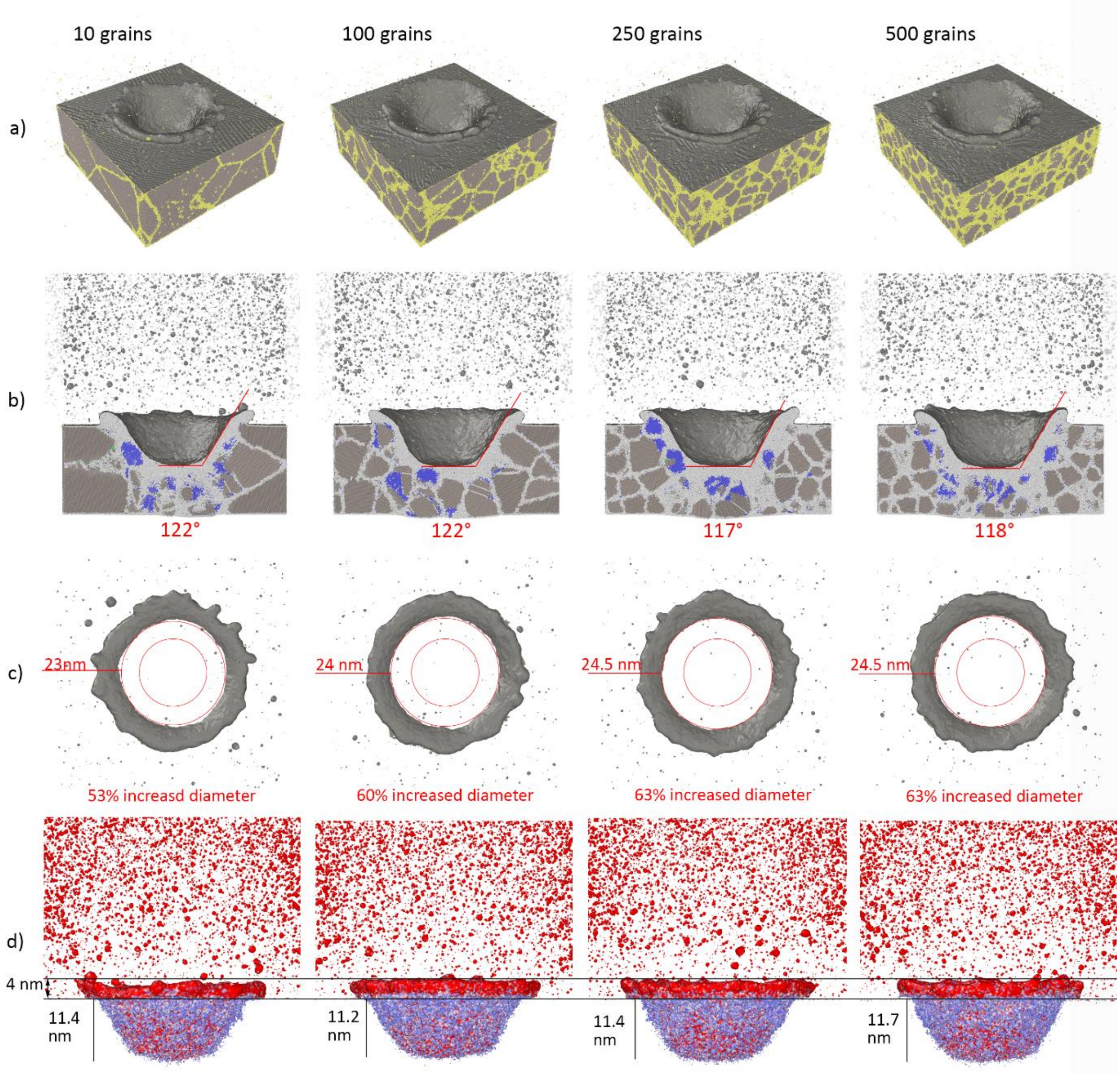

Figure 7.8 – a) Top view of craters. b) Angle of each crater wall. c) Increase in crater diameter after simulations. d) Crater depths and recast layer thicknesses as a function of grain size at the end of 50 ps simulations.

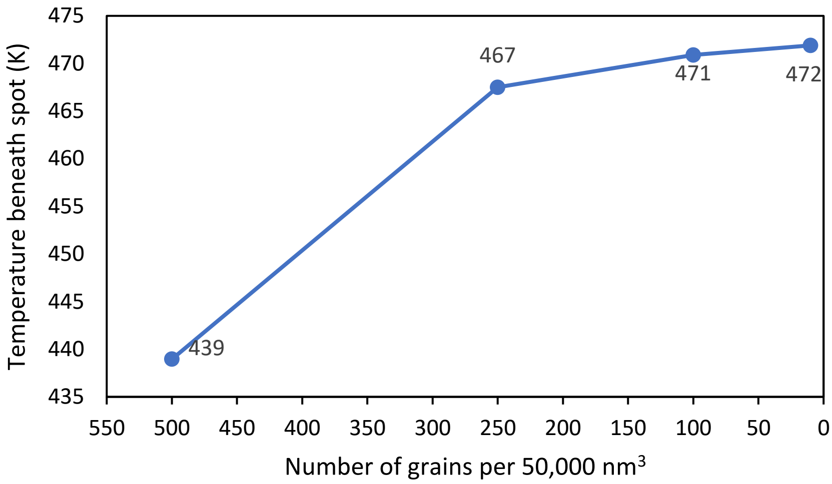

Figure 7.9 - Temperature of atoms beneath craters as a function of grain size at the end of 50 ps simulations.

In precision manufacturing, the observed effects of grain size on laser ablation have important implications. The slightly larger craters associated with smaller grains may influence the dimensional accuracy of manufactured components. Researchers need to consider these variations to ensure the precise control of material removal and geometric accuracy during the laser ablation process. The smoother recast layer and crater surface associated with smaller grains can be advantageous in precision manufacturing. Smoother surfaces contribute to enhanced surface finish, which is often a critical requirement in applications where precision is paramount. This characteristic can be particularly beneficial in industries such as microelectronics or medical device manufacturing, where the surface quality directly impacts functionality and performance. Understanding the implications of grain size variations allows manufacturers to tailor their laser ablation processes based on specific requirements for dimensional accuracy, surface finish and overall precision.

7.3. Experimental evaluation of size effect in laser ablation of titanium

A series of experiments were undertaken at the Materials Lab, Oxford University, UK, to explore the size effect and compare them with the simulation results. In this study, a CP titanium sample was prepared and was subjected to single laser pulse of 350 femtoseconds, with a wavelength of 515 nm (see chapter 4 for details). Three distinct spot diameters—approximately 250 nm, 500 nm, and 1000 nm—were chosen and the laser fluence was set at around 23 J/cm². Subsequently, the experimental results were investigated using a SEM and an AFM. Several compelling factors contribute to the argument that the experimental findings substantiate and confirm the accuracy of the MD simulation results. The observed pattern of size effect in the experimental data were identical to the patterns obtained from the MD simulations of smaller range of craters. The increase in the recast layer as the beam spot was enlarged, mirrored the trends anticipated by the MD simulations. This consistency provided evidence that the simulated conditions and parameters effectively captured the real-world response of the material in this respect.

In the conducted experiments, a discernible trend that emerged was the reduction in the ratio of crater diameter to beam spot diameter as the beam spot diameter increased. This observation aligned seamlessly with the overarching premise of this thesis which, argues that the extent of HAZ and resolidified recast layer is more pronounced at the nanometre length scale. It becomes apparent that the rate of crater expansion is negligible in comparison to variations in the beam spot diameter in larger length scales. Consequently, as the beam spot diameter is scaled down to the nanometre level, the resulting recast layer assumes significant proportions. Although, direct comparison between the simulation and experiments is challenging due to the differing ranges of laser spot sizes, examining the correlation between the percentage increase in crater diameter and the beam spot diameter in ablation with a 250 nm spot, the experimental and simulated results exhibited striking similarity. This alignment serves to reinforce central argument of this thesis by demonstrating the disproportionate growth in the size of the recast layer in nanoscale. It can be contended that this correlation remains relatively stable until the spot diameter is expanded to at least 250 nm, as demonstrated here.

Despite variations in environmental conditions between the experiments - conducted under ambient room temperature and pressure, exposed to atmospheric gases and contaminants - and the idealised conditions in the MD simulations involving a defect-free material within a perfect vacuum devoid of gravity, the observed ratio persisted consistently for the smallest tested spot diameter. Figure 7.11 illustrates the percentage increase in this ratio for all three beam spot diameters with images obtained by SEM.

In the following sections, the size effect on the angle of crater wall, crater depth and the height of the recast layer for all three beam spot diameters is discussed. For each beam spot diameter and energy level in the experiment, five identical craters were created. The selection of these specific craters for analysis was deliberate, as it exhibited superior definition and the highest resolution among the available options. The decision to focus on these particular craters was driven by the need to ensure precision and clarity in the evaluation process. Craters with well-defined features and high resolution provided a more detailed and accurate representation of their structural characteristics. An AFM was used to scan the surfaces of samples and NanoScope Analysis software developed by the manufacturer of the device (Bruker) was utilised to process the data. Figure 7.10 illustrates a 3D representation of the spots picked for this analysis.

In the nanoscale metrology of these results, the use of AFM in this case, the selection of an appropriate datum involved thoughtful considerations. Specifically, cleaner areas within the craters were chosen for measurement to ensure that the collected data accurately reflected the characteristics of the ablated surface. This choice was motivated by the desire to eliminate potential influences from debris or irregularities resulting from the laser ablation process, thus providing a clearer representation of the material's response. Ultimately, the aim was to select a datum that accurately represented the overall response of the material to USP laser ablation within the nanoscale, a representative portrayal that was less skewed by isolated anomalies.

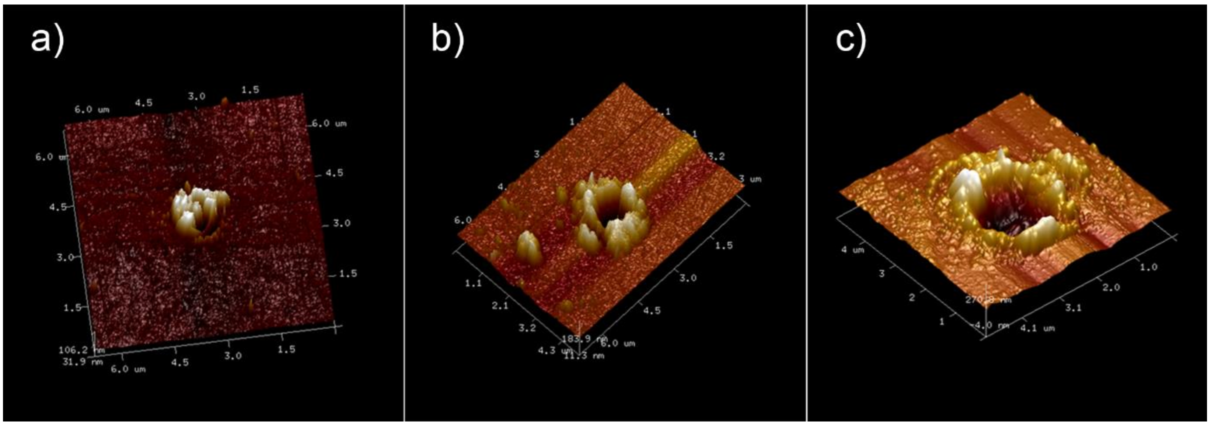

Figure 7.10 - AFM-generated 3D images depicting craters ablated by laser spot diameters of (a) 250 nm, (b) 500 nm, and (c) 1000 nm.

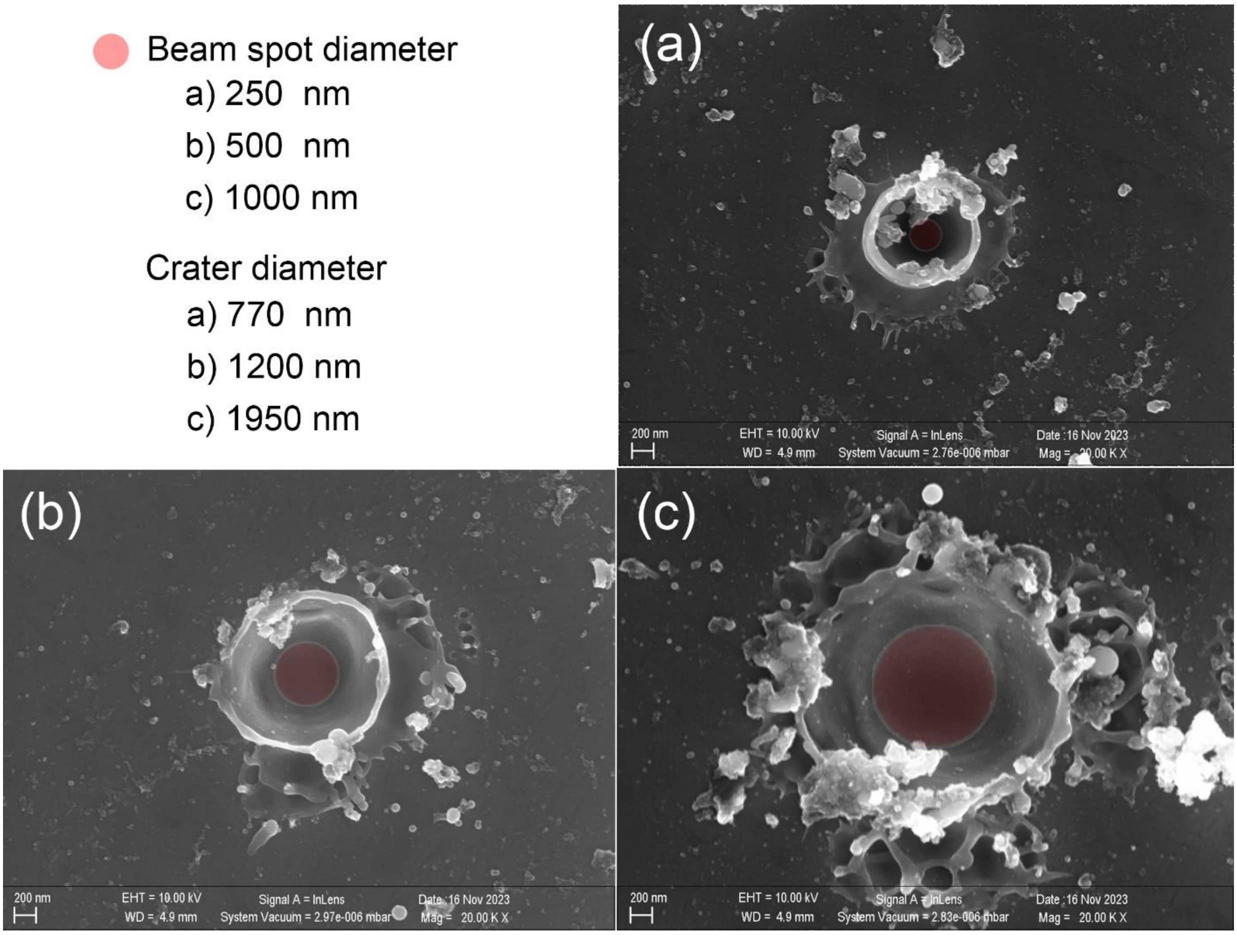

Figure 7.11 - SEM images showcasing single-shot laser ablation of spot sizes measuring (a) 250 nm, (b) 500 nm, and (c) 1000 nm, magnified at 20,000 times. Red circle overlays are the beam spot diameters scaled with the corresponding image.

7.3.1. AFM analysis of CP titanium ablated by 250 nm laser spot diameter

The analysis focused on the cross-sectional cut of the crater, as illustrated in Figure 7.12. The inclination of the crater wall was assessed through measurements taken at three different section profiles. The average recorded angle was determined to be 121 ± 5 degrees, indicating a deviation of approximately 31 degrees from the vertical. The deepest point within the crater was approximated to be at a depth of around 137 nm, while the highest point of the resolidified particles on the surface was estimated to be approximately 134 nm. Detailed values generated by the software are presented in Table 7.3.

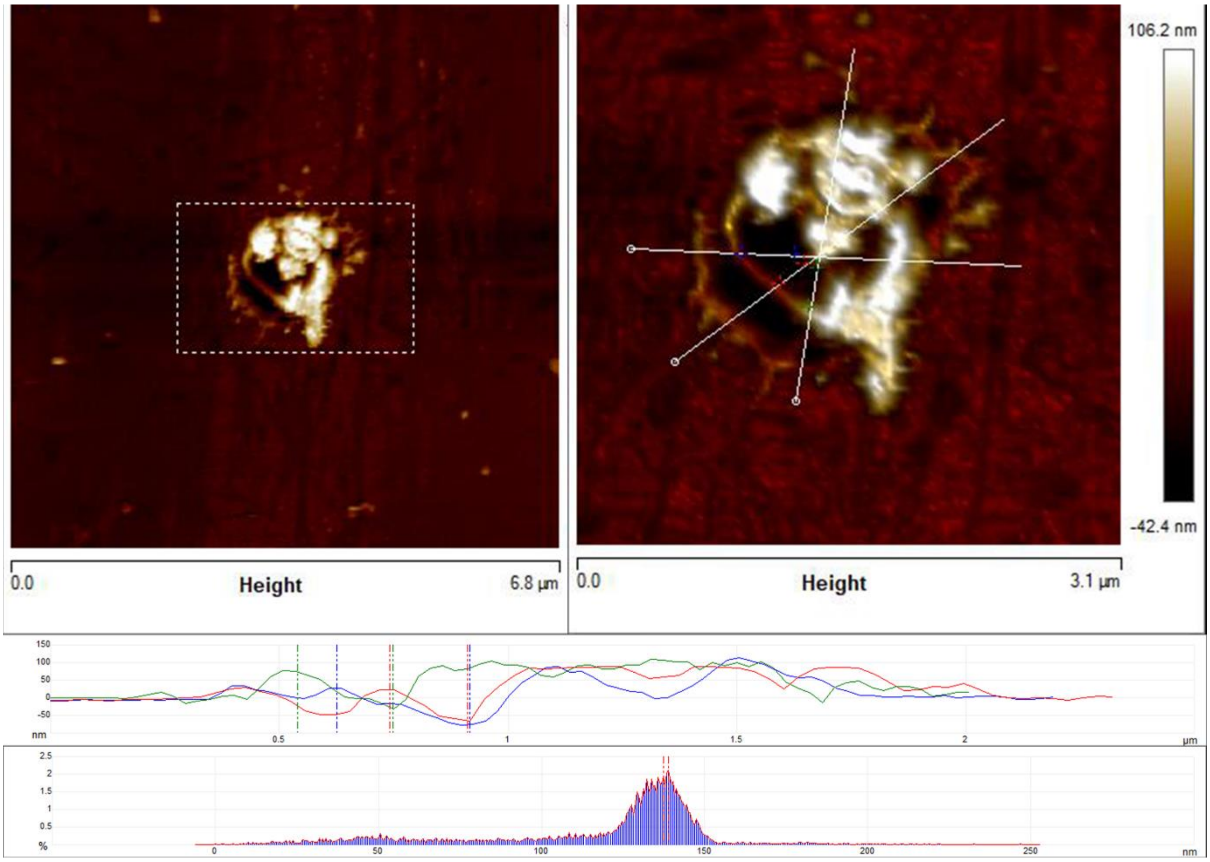

Figure 7.12 – Crater depth and recast layer height for the 250 nm laser beam spot diameter using the Section tool in NanoScope Analysis software. The histogram corresponds to the region marked with a dotted rectangle. Three lines on the crater represent section cuts, each with two points indicating the locations where the crater wall angle was measured. The color-coded section profiles correspond to their respective graphs.

Table 7.3 - Measurements of the cross-sectional profile of the crater formed by a 250 nm laser spot.

Average crater wall angle	121 ° ± 5°
Peak to Peak Distance	3.55 nm
Minimum Peak Depth	137 nm
Maximum Peak Depth	134 nm
Depth at Histogram Maximum	134 nm
Number Peaks	132

7.3.2. AFM analysis of CP titanium ablated by 500 nm laser spot diameter

The section cut of the crater as shown on Figure 7.13 was evaluated. The average measured value for the angle of crater wall was 141.6 ± 3 degrees, deepest point of the crater was suggested to be around 194 nm and the highest point of the recast material was estimated to be around 190 nm. The values generated by the software are provided in Table 7.4.

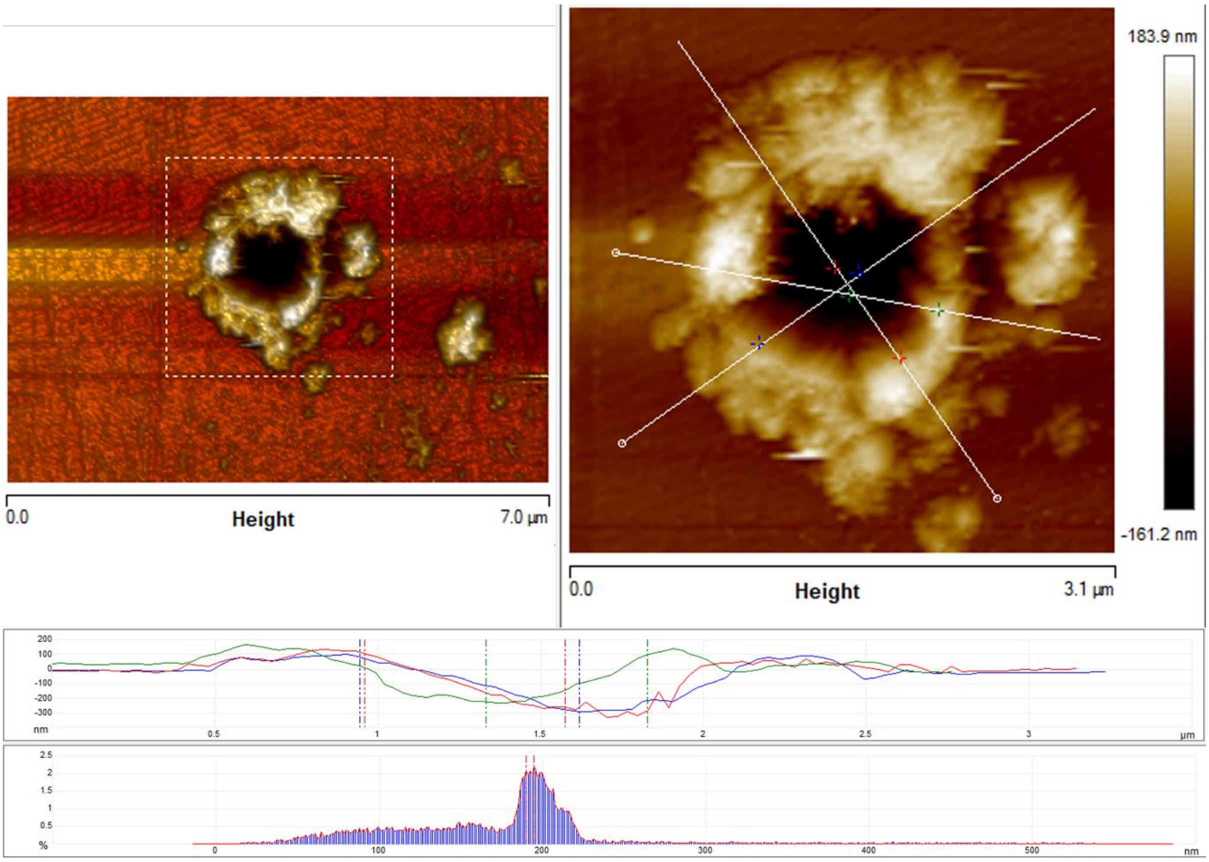

Figure 7.13 – Crater depth and recast layer height for the 500 nm laser beam spot diameter using the Section tool in NanoScope Analysis software. The histogram corresponds to the region marked with a dotted rectangle. Three lines on the crater represent section cuts, each with two points indicating the locations where the crater wall angle was measured. The color-coded section profiles correspond to their respective graphs.

Table 7.4 - Measurements of the cross-sectional profile of the crater formed by a 500 nm laser spot.

Angle	**141.6° ± 3°**
Peak to Peak Distance	3.5 nm
Minimum Peak Depth	194 nm
Maximum Peak Depth	190 nm
Depth at Histogram Maximum	190 nm
Number Peaks	138

7.3.3. AFM analysis of CP titanium ablated by 1000 nm laser spot diameter

The section cut of the crater as shown on Figure 7.14 was evaluated. The average measured value for the angle of crater wall was 145.2 ± 4 degrees, deepest point of the crater was suggested to be around 292 nm and the highest point of the recast material was estimated to be around 305 nm. The values generated by the software are provided in Table 7.5.

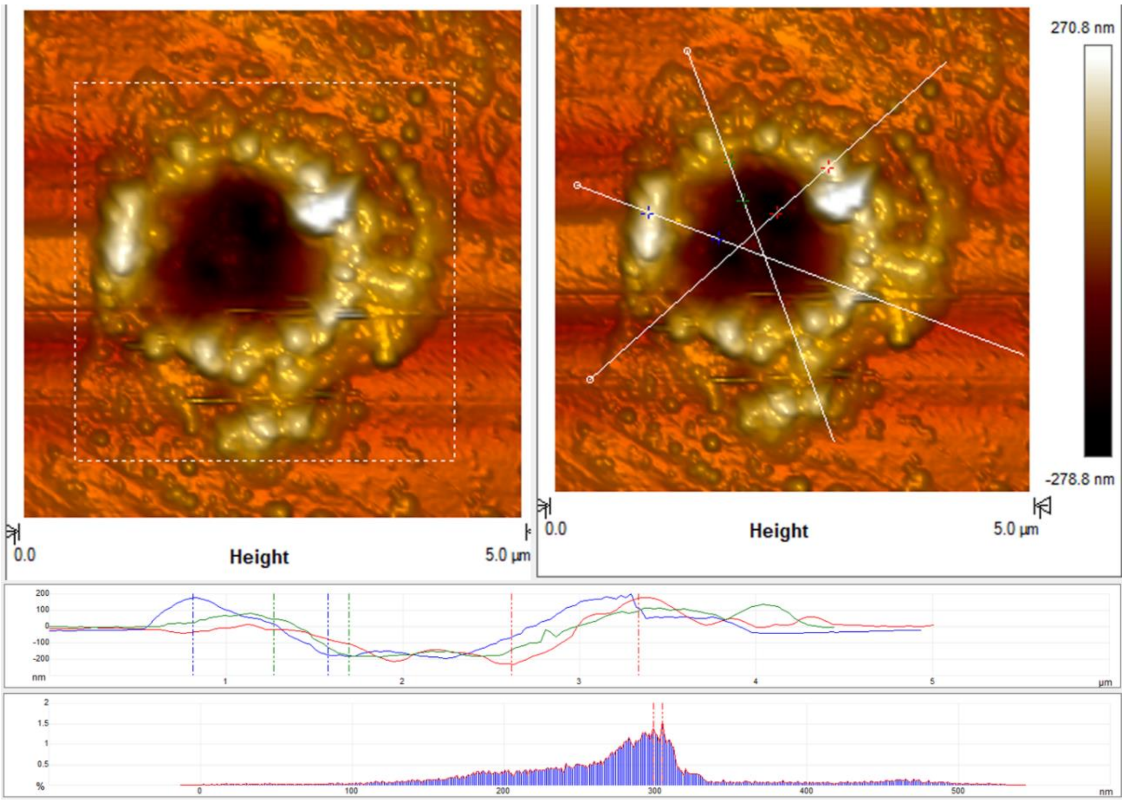

Figure 7.14 - Crater depth and recast layer height for the 1000 nm laser beam spot diameter using the Section tool in NanoScope Analysis software. The histogram corresponds to the region marked with a dotted rectangle. Three lines on the crater represent section cuts, each with two points indicating the locations where the crater wall angle was measured. The color-coded section profiles correspond to their respective graphs.

Table 7.5 - Measurements of the cross-sectional profile of the crater formed by a 1000 nm laser spot.

Angle	**145.2° ± 4°**
Peak to Peak Distance	12 nm
Minimum Peak Depth	292.5 nm
Maximum Peak Depth	305 nm
Depth at Histogram Maximum	305 nm
Number Peaks	149

7.3.4. Comparison of simulation results with experimental measurements

The calculated and measured values obtained from simulations and experiments respectively are detailed in Table 7.6. For a clearer understanding of the trends associated with each dataset, the corresponding values from both experiments and simulations are graphically represented. Figures 7.15 depicts the comparisons between the observed trends in the experiments and the values calculated in simulations.

Table 7.6 - calculated and measured values obtained from simulations and experiments.

	Experiment			**Simulation**			
Beam Spot Diameter (nm)	250	500	1000	10	15	20	25
Crater Wall Angle (°)	121 ± 5	141.6 ± 3	145.2 ± 4	104 ± 2	117 ± 2	122 ± 2	123 ± 2
Crater Depth (nm)	137.36	193.668	292.497	10.4	10.7	12.1	12.9
Recast Layer Height (nm)	134	190	305	1	2	3	4

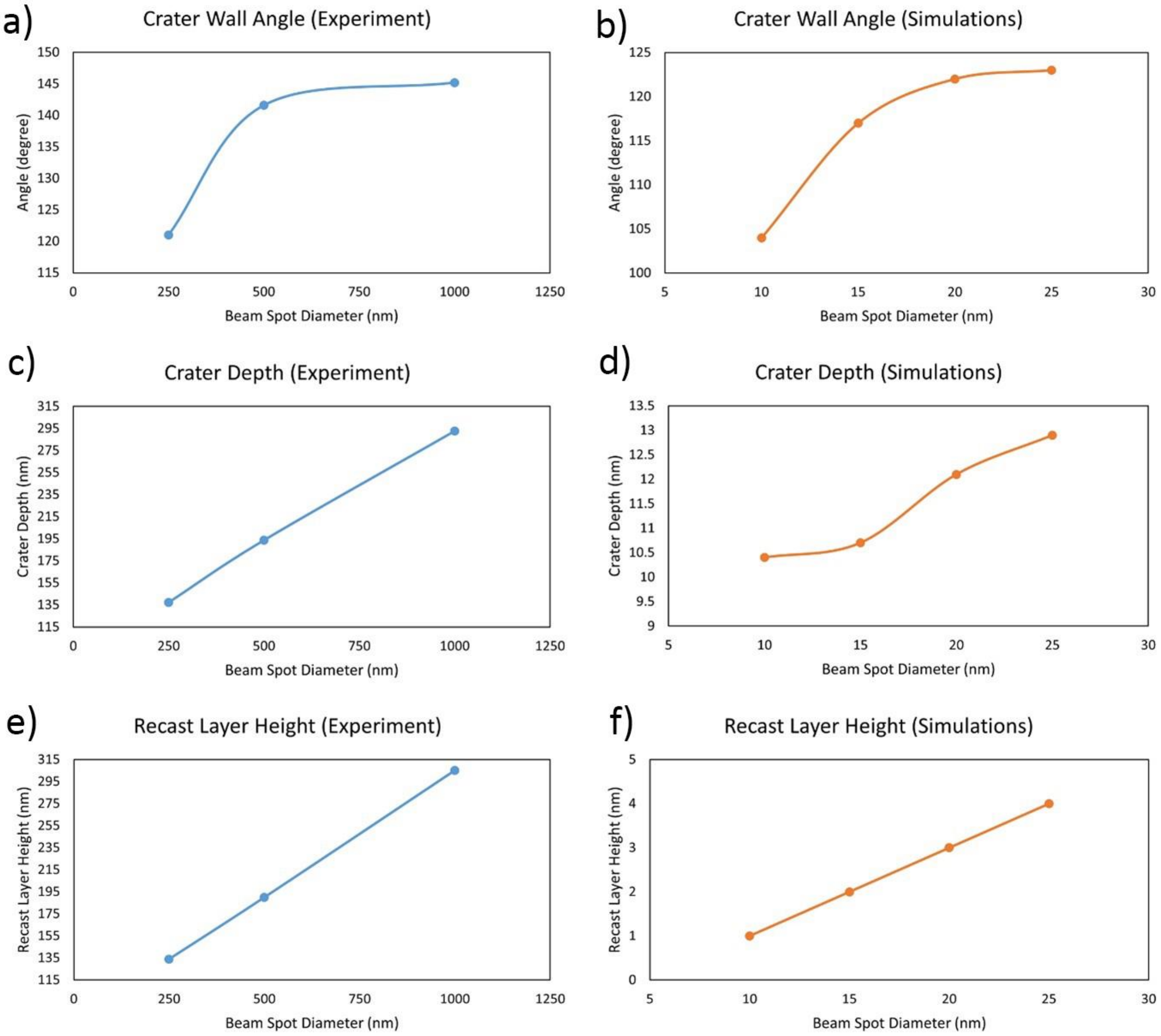

Figure 7.15 – Visualising trends: Comparative analysis of crater wall angle, crater depth and recast layer height in USP laser ablation experiments (a, c, e) and simulations (b, d, f) based on varying beam spot diameters.

The similarities between the experimental and simulated outcomes go beyond mere coincidences. The fact that the experiments were carried out in a realistic setting, subject to various external factors and yet yielded results that closely resemble the MD simulations and the predicted patterns, despite the limitations and assumptions made in simulations, emphasises the reliability of the simulation setup. This comparison not only bolsters confidence in the simulation methodology but also highlights the broader applicability of the insights gleaned from simulations to real-world experimental scenarios. This remarkable transferability of MD simulation results to practical experiments enhances the significance of the findings and underscores the potential impact on improving the real-world applications.

7.4. Conclusion

In conclusion, this extensive series of MD simulations explored the complex relationship between various parameters and the USP laser ablation process of pure titanium. The primary focus was to explore the size effect in response to changes in the beam spot diameter of an identical laser fluence as well as the influence of grain size on the ablation process, with profound implications for precision manufacturing.

The key observations included:

1. The impact of changes in the beam spot diameter on material response to laser irradiation was both distinctive and noteworthy. Decreasing the beam spot size elevated the energy requirement for material temperature elevation. Notably, as the beam spot diameter decreased, it yielded thinner recast layers and relatively shallower craters, maintaining a consistent ratio of crater diameter to beam spot area. This revelation emphasises the potential for optimising the ablation process by precisely adjusting the beam spot diameter. This fine-tuning can be particularly advantageous in applications requiring meticulous material removal control, such as microfabrication and nanostructuring. Manufacturers can significantly enhance laser ablation process efficiency by optimising the beam spot size, leading to improved precision, product quality and reduced energy consumption.
2. Simulations revealed a direct and substantial correlation between the grain size and the material’s response to the incoming laser irradiation. Larger grain sizes required more energy to raise the material’s temperature, speculatively due to the decreased number of grain boundaries, impeding defect flow and increased melting point. While the laser fluence and the beam spot area remained consistent across all cases, a noticeable 36% higher laser fluence was required to ablate an identical volume of atoms as the grain size was increased when decreasing the number of grains from 500 to 10 grains in the identical volume. Visual inspections of the resulting craters also indicated that ablation of smaller grains resulted in a smoother recast layer and increased crater circularity, contributing further to the understanding of the relationship between grain size effect on the laser ablation process. These observations provide valuable

insights for optimising laser parameters in processing of materials with varying grain sizes.

3. In terms of the heat conductivity of the material, while the grain size had a minimal impact, atoms in the bulk of material with smaller grains remained cooler, possibly due to increased grain boundaries and less heat conduction. Simulations also revealed that the larger spot diameter of an identical ablation process led to a slightly higher average temperature rise in the bulk. This indicated an enhanced heat conductivity of the larger spot diameter, likely due to the size effect.

In summary, this chapter unveils the intricate nature of size effects in USP laser ablation, emphasising their profound impact on precision manufacturing and the tailoring of laser ablation processes to meet specific material and geometric needs.

Chapter 8 — Conclusions and future work

8.1. Research outcome

In this section, the outcome of this work is explained against the objectives of the project:

1. Investigate ultrashort pulsed laser ablation of titanium through molecular dynamics simulations and experimental examinations, encompassing variations in beam spot diameter and grain size:

This project explored USP laser ablation of titanium, employing a holistic approach that integrated both MD simulations and experimental examinations. The impact of varying beam spot diameters (10 nm, 15 nm, 20 nm, and 25 nm) on identical substrates was studied using MD simulations. Additionally, the size effect influenced by grain size was explored through MD simulations by subjecting substrates (50 x 50 x 20 nm^3) consisting of 10, 100, 250 and 500 grains to an identical laser irradiation with a beam diameter of 15 nm. To further investigate the impact of grain size, two substrates (100 x 100 x 20 nm^3) were modelled, one as a single crystal and the other consisting of 2000 grains of random shapes and orientations, both subjected to identical laser pulses. Moreover, a series of experiments were conducted wherein cast titanium samples of grade 2 and 5, along with a 3D-printed sample of Ti-6Al-4V alloy, were systematically exposed to laser pulses of various intensities. This approach aimed to explore both the size effect imposed by the laser beam spot diameter and the influence of methods used in the production of samples on USP laser ablation outcomes.

2. Examine the relationship between size effects in laser ablation with a focus on adjusting beam spot diameters for precision manufacturing applications such as fabricating nanostructures on metallic surfaces to enhance surface properties:

Findings highlighted the significance of adjusting beam spot diameters for ultra-precision manufacturing. Notably, the simulations indicated that the 10 nm laser beam spot diameter compared to the 25 nm requires 59% more absorbed laser energy to produce plasma plume with average temperature of 9000 K. The ratio of the angle of the crater wall to the beam spot diameter in these simulations exhibited approximately 30% increase when the beam spot diameter transitioned from 10 nm to 15 nm, 28% increase when it shifted from 15 nm to 20 nm, and 23% increase when it extended from 20 nm to 25 nm. The ratio of the crater diameter to the beam spot area was almost equally increased in all simulations which suggested that the beam spot size did not significantly affect this parameter. However, the thickness of the recast layer and the crater depth decreased as the beam spot diameter decreased.

3. Determine the influence of grain size on the efficiency of ultrashort pulsed laser ablation, exploring the correlation between grain size, ablation threshold, and heat conductivity during the process:

The investigation indicated a clear correlation between grain size and the laser fluence necessary for ablation. With an increase in grain size, there was a corresponding 36% rise in the energy required to elevate the temperature of plasma plume to 9000 K, notably observed when reducing the number of grains from 500 to 10 within an identical volume. This suggested a decrease in heat conductivity in samples with smaller grains, attributable to the increase in grain boundaries. Consequently, the ablation threshold decreased in samples with smaller grains. The reduction in heat conductivity facilitated the containment of absorbed laser fluence within the beam-affected volume, thereby enhancing the ablation efficiency compared to the sample with larger grains.

4. Conduct a comparative analysis of laser ablation outcomes on different grades of titanium, including commercially pure titanium with single crystal and polycrystalline structures, as well as casted and 3D-printed Ti-6Al-4V alloy:

The comparison of results obtained from single-shot laser ablation between casted and 3D-printed Ti-6Al-4V alloy indicated that the 3D-printed surface ($R_a = 32\,nm$) exhibited a slightly neater crater and smoother recast layer compared to the casted material ($R_a = 45\,nm$). This observation was made following the exposure of both substrates to ultrashort pulsed laser irradiation using identical laser parameters.

5. Bridge the gap between molecular dynamics simulations and experimental results by comparing the results and providing a nuanced understanding of the size effects and material distinctions in ultrashort pulsed laser ablation:

Simulations utilised the largest attainable atomic system (constrained the available computational power) to capture atomistic behaviour, offering insights into overarching trends during USP laser ablation. Conversely, experiments concentrated on high-resolution measurements of the smallest achievable craters using techniques such as AFM and SEM. The integration of these methodologies facilitated the study in achieving a thorough comprehension of the effects of beam spot size as a laser parameter and grain size as a representation of material properties. Consequently, this approach expanded the scope of comparing simulation predictions with experimental observations at this scale.

6. Integrate research results into practical solutions, offering insights for precision manufacturing applications based on size effects and material considerations:

These findings have implications for ultra-precision manufacturing in nanoscale. A key parameter influencing material response during laser ablation has been identified as the adjustment of the beam spot diameter. Thinner recast layers and shallower craters are brought about by smaller beam spot sizes, offering improved precision and control over geometric features. Insights for tailoring laser ablation processes in ultra-precision manufacturing based on specific material characteristics were provided by assessing the correlation between grain size and material response. Furthermore, the relationship between heat conductivity and material response to USP laser irradiation provided insights that can be applied to manage heat effectively during these processes.

The influence of the manufacturing method on USP laser ablation is also a crucial aspect addressed here. This study revealed distinct material responses based on the manufacturing method employed to produce a part. Specifically, the 3D-printed Ti-6Al-4V alloy exhibited a relatively more efficient and smoother material removal process, showcasing deeper craters compared to the casted alloy.

Moreover, the investigation into the size effect demonstrated a noticeable alteration in crater depth and geometry as well as the recast layer size, particularly associated with laser energy dissipation, when the beam spot diameter was increased to around 3 μm.

7. Identify potential areas for further research and exploration in ultrashort pulsed laser ablation of titanium, contributing to the advancement of laser technologies

and the development of new surface characteristics and their applications in the field:

Examples of potential areas for further research and exploration are outlined in section 8.4. Scripts used to initiate simulations and logged calculations of thermodynamic properties post simulations are accessible via the link: Parris-G/Scripts: Scripts used to initiate simulations (github.com)

8.2. Contribution to knowledge

This research project has taken an innovative approach to investigate USP laser ablation of titanium and its alloys, namely CP titanium and Ti-6Al-4V, employing a combination of MD simulations and experiments. A significant breakthrough was achieved through the modification of the LAMMPS code, allowing for independent modelling of user-defined beam spot geometries. This modification enhances the flexibility and precision of laser-material interaction exploration, offering nuanced insights into the influence of different spot geometries and sizes on the ablation process. Notably, a more comprehensive way of integrating the temperature-dependent electronic properties into MD simulations represented a key research novelty. This modification provided a more accurate depiction of the material's atomic-scale response to temperature changes, addressing a critical aspect of laser-material interactions in extreme conditions. By capturing temperature variations and their effects on electronic responses, these simulations aimed to offer a comprehensive portrayal of a USP laser ablation process under varying conditions.

The integration of this modified temperature-dependent TTM package into the widely used and open-source LAMMPS code represents a significant advantage for the field of MD simulations. LAMMPS, being well documented and open-source resource, offers accessibility and transparency, making it an attractive platform for researchers across various disciplines. Compared to more complex simulation software with commercial pricing, the LAMMPS-TTM combination provides a user-friendly and cost-effective solution. The open-source nature allows researchers to modify and adapt the code according to their specific needs, fostering collaboration and accelerating advancements in the field.

Furthermore, the modified TTM package is not limited to the study of USP laser ablation alone. Its applicability extends to any other two-temperature phenomenon requiring an external energy source, providing a versatile tool for researchers exploring various thermal processes at the atomic scale. In addition, subject to existing potential functions, this integrated approach can facilitate the simulation of a diverse range of materials under similar conditions. Researchers can leverage this capability to extract valuable data beyond the scope of the current project, contributing to a more comprehensive understanding of material responses to USP laser irradiation.

Therefore, the TTM/LASER add-on to the LAMMPS code, including the ability to model user-defined external energy source and the incorporation of comprehensive temperature-dependent electronic properties, further advances the work of Phillips et al [120] and Starikov and Pisarev [10], highlighting the commitment of this project to advancing research in USP laser ablation.

This project achieved a significant milestone by establishing a correlation between patterns observed in MD simulation results and experimental findings. Despite the inherent difficulties associated with simulating large atomic systems and conducting experiments at the nanoscale, this project successfully demonstrated consistency between these two methodologies. It is important to note that direct comparison between simulations and experiments was not achievable due to differences in scale. However, in this project, every effort was dedicated to advancing MD simulations and ensuring their synchronisation with experimental conditions.

This endeavour highlights the innovative efforts of this project in bridging computational simulations with practical experimental scenarios, despite the challenges of scale disparity due to the limitations of current computational power available for simulations. However, this methodology enhances the reliability and applicability of insights derived from simulations, expanding the scope of what can be realistically simulated and measured in nanoscale experiments. This success in aligning these research facets by comparing and analysing the patterns in each method provides a strong foundation for further exploration of USP laser ablation processes, facilitating more accurate predictions and a deeper understanding of material responses under extreme conditions. This breakthrough not only contributed to the advancement of MD simulations but also reinforced the crucial role they play in shaping the landscape of intricate processes at the atomic level, expanding the horizons of both simulation capabilities and experimental applications in the realm of nanoscale research to contribute to the gap in knowledge identified by Stratakis et al [6] and further explore the role of laser beam spot size on the ablation process as was highlighted by Perrière et al [4].

In the realm of experimentation, this project has also made commendable strides by, measuring and examining the complexities of incredibly small features. This marks an impressive milestone, given the considerable hurdles involved in conducting experiments at such minute scales.

8.3. Limitations and assumptions associated with MD simulations

When employing MD simulations to investigate femtosecond laser ablation, several limitations arise due to the distinctive characteristics of this process. The ultrafast dynamics and the initial stages of laser-material interaction, characterised by high energy densities delivered by laser beams, pose difficulties in accurate representation in simulations. These conditions can lead to extreme local temperature and pressure, impacting the accuracy of classical force fields in describing electronic and thermal effects under such circumstances. At high temperatures induced by USP laser irradiation, atoms in the skin layer vibrate vigorously. Classical force fields are based on harmonic assumptions and can lead to inaccuracies in calculating bond lengths, angles and torsional energies in these environments. High pressure also can compress atoms more than usual, resulting in repulsions that may not be fully captured by classical force fields. Moreover, extreme temperatures and pressures highlight electronic effects such as charge transfer and polarisation that is often ignored by classical force fields, resulting in a poor description of electronic structure under such circumstances. Additionally, USP laser induces non-equilibrium electronic excitations in materials, a phenomenon not fully explored by MD simulations, which do not explicitly model electronic states. This is significant in the context of USP laser ablation since the site affected by the laser beam remains in non-equilibrium for the entire duration of the pulse (for up to 10 ps) and the atomic energy and movements are directly influenced by the electronic response of the material to the irradiation. The modified TTM code in this project was designed to address these limitations to an extent.

Moreover, the potential occurrence of phase transitions such as melting and vaporisation during ablation process introduce challenges, particularly in predicting these transitions and subsequent material response accurately. Similarly, surface effects such as surface melting, ablation thresholds and damage mechanisms may be challenging to capture accurately in MD simulations. The use of EAM potentials in this project provided a robust framework for a more precise and insightful exploration of the material responses under the extreme conditions induced by the ablation process.

Accurate modelling of thermal transport in these highly dynamic processes is also crucial where rapid heating and subsequent cooling play a significant role. Furthermore, the complex interaction between femtosecond laser pulses and materials may involve multiphoton absorption. Femtosecond laser pulses can induce nonlinear effects such as self-focusing or filamentation, which may not be adequately captured by standard MD simulations that assume linear response. The accuracy of the models used to describe these interactions can significantly influence simulation results. However, these effects become significantly more pronounced at extremely high laser intensities. The MD simulations conducted in this study focus on laser powers close to the material’s ablation threshold, where such effects are not typically encountered.

The accurate representation of material properties, including thermal conductivity, specific heat, and electronic structure is essential for realistic representation of USP laser ablation. Additionally, depending on the scale of the system being simulated, the computational resources required for large-scale simulations of femtosecond laser ablation can be demanding, limiting the ability to study realistic materials or complex geometries. The goal of this project was to maximise the sample size within the constraints of the available computational power. To improve the accuracy, input values representing the material properties were fine-tuned based on the current temperature at each step of the calculations.

Moreover, the simulations in this project began post absorption of the pulse energy. This deliberate choice was made to streamline the simulation process and enhance computational efficiency. Considering the complexity introduced by accounting for surface quality and skin effect on the absorbed energy, opting for the simplified assumption served the purpose of expediting the simulation without compromising the primary objectives of the study. By focusing on the absorbed pulse energy alone, the simulation aimed to provide fundamental insights while circumventing the intricacies associated with modelling surface quality and skin effect, thereby ensuring a more manageable and resource-efficient approach.

Despite these challenges, MD simulations can provide valuable insights into the fundamental processes involved in USP laser ablation. Ongoing advancements in simulation methodologies and increased computational power hold promise for addressing some of these limitations in future research.

8.4. Future research

Future work in the field of USP laser ablation and precision manufacturing can focus on several avenues to enhance understanding and optimise processes. Conducting MD simulations with potential functions tailored to the unique characteristics of Ti-6Al-4V alloy used in precision manufacturing can offer more accurate atomic-level insights into laser-material interactions with this material. Systematically varying laser parameters beyond fluence, such as pulse duration and repetition rate, could uncover additional nuances in laser-material interactions and their impact on material removal efficiency.

Future investigations could extend the simulation capabilities by incorporating the modelling of various laser beam spot geometries. By simulating diverse beam spot shapes, such as elliptical, rectangular or irregular configurations, researchers can gain a more comprehensive understanding of how different geometries influence the laser-material interaction during USP laser ablation. This expansion in simulation parameters would provide valuable insights into the nuanced effects of beam spot geometry on material removal efficiency, heat dissipation, and other crucial aspects of the ablation process.

Utilising advanced imaging techniques for further material characterisation, especially focusing on the microstructural differences between different manufacturing methods, is crucial for refining precision manufacturing processes. The study can be extended to explore different types of commonly used alloys in precision manufacturing applications, investigating how variations in alloy composition influence laser ablation characteristics.

Additionally, exploring multi-scale modelling approaches that integrate different techniques, combining MD simulations with continuum-level models can provide a more comprehensive understanding of the material response to USP laser ablation across various length and time scales. Applying AI to multi-scale modelling approaches can also enhance the integration of different simulation techniques. AI-driven models can adapt and refine themselves based on the feedback from various length and time scales, leading to a more comprehensive understanding of the material response to USP laser ablation.

Conducting further experiments to confirm predictions made through MD simulations, including exploring additional materials, manufacturing methods and laser parameters, ensures the broader applicability of the insights gained from simulations. Investigating laser-induced surface modifications beyond ablation, such as LIPSS, crystalline structure alterations or induced stresses, can also contribute to a more holistic understanding of laser-material interactions.

Integrating real-time imaging techniques into the study of USP laser ablation can also provide a wealth of knowledge in this field. Techniques such as Transmission Electron Microscopy (TEM), high-speed microscopy, time-resolved imaging and ultrafast photography can provide unparalleled temporal precision, capturing transient stages of laser ablation. Advanced imaging modalities like confocal microscopy, multiphoton microscopy and SEM could offer a multi-dimensional view, enhancing the understanding of surface morphology and material transformations. In-situ monitoring with real-time feedback and exploring the potential of AI for image analysis could streamline data processing. This approach promises to contribute to more precise and controlled laser-based manufacturing applications.

In essence, this forward-looking agenda holds the promise of not just incremental progress but transformative breakthroughs in the intricate realm of USP laser ablation. The pursuit of these research avenues and more, collectively, is poised to shape the future trajectory of precision manufacturing, unlocking novel possibilities and pushing the boundaries of what can be achieved in this dynamic and evolving field.

References

1 Fadeeva, E. *et al.* Bacterial retention on superhydrophobic titanium surfaces fabricated by femtosecond laser ablation. *Langmuir*, 2011, 27 (6), pp. 3012–3019. DOI: 10.1021/la104607g

2 Larrañaga-Altuna, M. *et al.* Bactericidal surfaces: an emerging 21st century ultra-precision manufacturing and materials puzzle. *Applied Physics Reviews*, 2021, pp. 1–83.

3 Bruzzone, A.A.G. *et al.* Advances in engineered surfaces for functional performance. *CIRP Annals - Manufacturing Technology*, 2008, 57 (2), pp. 750–769. DOI: 10.1016/j.cirp.2008.09.003

4 Perrière, J. *et al.* Nanoparticle formation by femtosecond laser ablation. *Journal of Physics D: Applied Physics*, 2007, 40 (22), pp. 7069–7076. DOI: 10.1088/0022-3727/40/22/031

5 Ahmed, N. *et al.* Laser Ablation Process Competency to Fabricate Microchannels in Titanium Alloy. *Materials and Manufacturing Processes*, 2015, 30 (11), pp. 1290–1297. DOI: 10.1080/10426914.2015.1019132

6 Stratakis, E. *et al.* Laser engineering of biomimetic surfaces. *Materials Science and Engineering R: Reports*, 2020, 141 (June), p. 100562. DOI: 10.1016/j.mser.2020.100562

7 Lin, Z. *et al.* Femtosecond Laser Precision Engineering: From Micron, Submicron, to Nanoscale. *Ultrafast Science*, 2021, 2021. DOI: 10.34133/2021/9783514

8 M.I. Kaganov, I.M. Lifshitz, L.V.T. Relaxation between Electrons and the Crystalline Lattice. *Jetp*, 1955, 4 (9), p. 173.

9 Marla, D. *et al.* Critical assessment of the issues in the modeling of ablation and plasma expansion processes in the pulsed laser deposition of metals. *Journal of Applied Physics*, 2011, 109 (2). DOI: 10.1063/1.3537838

10 Pisarev, V. V. *et al.* Atomistic simulation of ion track formation in UO2. *Journal of Physics Condensed Matter*, 2014, 26 (47). DOI: 10.1088/0953-8984/26/47/475401

11 Zhang, Z. *et al.* Mechanisms of femtosecond laser ablation of Ni3Al: Molecular dynamics study. *Optics and Laser Technology*, 2021, 133 (March 2020), p. 106505. DOI: 10.1016/j.optlastec.2020.106505

12 Yan, Y. *et al.* An experimental study of PMMA precision cryogenic micro-milling. *Biomaterials and Polymers Horizon*, 2021, 1 (1), pp. 15–21. DOI: 10.37819/bph.001.01.0123

13 Goel, S. *et al.* Diamond machining of silicon: A review of advances in molecular dynamics simulation. *International Journal of Machine Tools and Manufacture*, 2015, 88, pp. 131–164. DOI: https://doi.org/10.1016/j.ijmachtools.2014.09.013

14 Misra, S. *et al.* Nanofabrication route to achieve sustainable production of Next Generation defect-free graphene : Analysis and Characterisation. *Nanofabrication*, 2021.

15 Maiman, T.H. *et al.* Stimulated Optical Emission in Fluorescent Solids. II. Spectroscopy and Stimulated Emission in Ruby. *Phys. Rev.*, 1961, 123 (4), pp. 1151–1157. DOI: 10.1103/PhysRev.123.1151

16 Lecture, N. Extreme Light Physics and Application. 2018, pp. 96–140.

17 Schaeffer, R. *Fundamentals of laser micromachining*. CRC press, 2012.

18 Karlsons, D. *et al.* Q -Switched CaWO 4 : Nd 3 + Laser. 1963, 3407 (June 1963), pp. 10–12.

19 Antum, O.F.Q. V. Characteristics of mode-coupled lasers. 1963, pp. 12–20.

20 Strickland, D. *et al.* Compression of amplified chirped optical pulses. *Optics Communications*, 1985, 56 (3), pp. 219–221. DOI: 10.1016/0030-4018(85)90120-8

21 Qiu, T.Q. *et al.* Heat Transfer Mechanisms During Short-Pulse Laser Heating of Metals. *Journal of Heat Transfer*, 1993, 115 (4), pp. 835–841. DOI: 10.1115/1.2911377

22 Anisimov, S.I. *et al.* Electron emission from metal surfaces exposed to ultrashort laser pulses. *Zh. Eksp. Teor. Fiz*, 1974, 66 (2), pp. 375–377.

23 Qiu, T.Q. *et al.* Femtosecond laser heating of multi-layer metals-I. Analysis. *International Journal of Heat and Mass Transfer*, 1994, 37 (17), pp. 2789–2797. DOI: 10.1016/0017-9310(94)90396-4

24 Dennis, A. *et al.* The importance of wavelength for tight temperature control during µ-laser-assisted machining. *Journal of Micromanufacturing*, 2021, 4 (1), pp. 93–98. DOI: 10.1177/2516598420917866

25 Chichkov, B.N. *et al.* Femtosecond, picosecond and nanosecond laser ablation of solids. *Applied Physics A: Materials Science & Processing*, 1996, 63 (2), pp. 109–115. DOI: 10.1007/s003390050359

26 Ye, M. *et al.* Time-of-flight and emission spectroscopy study of femtosecond laser ablation of titanium. *Journal of Applied Physics*, 2001, 89 (9), pp. 5183–5190. DOI: 10.1063/1.1360696

27 Zhigilei, L. V. *et al.* Velocity distributions of molecules ejected in laser ablation. *Applied Physics Letters*, 1997, 71 (4), pp. 551–553. DOI: 10.1063/1.119606

28 Hirayama, Y. *et al.* Heat effects of metals ablated with femtosecond laser pulses. *Applied Surface Science*, 2002, 197–198, pp. 741–745. DOI: 10.1016/S0169-4332(02)00403-8

29 Rethfeld, B. *et al.* Timescales in the response of materials to femtosecond laser excitation. *Applied Physics A: Materials Science and Processing*, 2004, 79 (4–6), pp. 767–769. DOI: 10.1007/s00339-004-2805-9

30 Feng, Q. *et al.* Ti : Sapphire Laser System 780 nm wavelength 150 fs pulses 1kHz repetition rate Neutral density filters 3-axis stage Focusing lens Z optical axis Quarter wave plate Fast acting shutter Sample. *Materials Science*, 2004.

31 Grojo, D. *et al.* Plasma analyses during femtosecond laser ablation of Ti, Zr, and Hf. *Journal of Applied Physics*, 2005, 97 (6). DOI: 10.1063/1.1861519

32 Tanaka, Y. *et al.* Microscopic mechanism of ultrashort-pulse laser ablation of metals: a molecular dynamics study incorporating electronic entropy effects. 2023. DOI: 10.1088/1361-6463/acdb81

33 Mishra, R.K. *et al.* Computational prediction of electrical and thermal properties of graphene and BaTiO3 reinforced epoxy nanocomposites. 2022, 1, pp. 1–14.

34 Ciccotti, G. *et al.* Molecular simulations: past, present, and future (a Topical Issue in EPJB). *European Physical Journal B*, 2022, 95 (1). DOI: 10.1140/epjb/s10051-021-00249-x

35 Cleveland, C.L. *et al.* A study of a laser-annealirg system using a new molecular dynamics method modified to faithfully simulate typical experimental conditions is presented. Following melting, the re- crystallization interface is layer structured in the melt. Rapid recrystalli. 1982, 49 (11), pp. 11–14.

36 Yamashita, Y. *et al.* Heat transport analysis for femtosecond laser ablation with molecular dynamics-two temperature model method. *Fusion Engineering and Design*, 2006, 81 (8-14 PART B), pp. 1695–1700. DOI: 10.1016/j.fusengdes.2005.09.011

37 Chen, J.K. *et al.* A semiclassical two-temperature model for ultrafast laser heating. *International Journal of Heat and Mass Transfer*, 2006, 49 (1–2), pp. 307–316. DOI: 10.1016/j.ijheatmasstransfer.2005.06.022

38 Zhou, Y. *et al.* Efficient modeling of metal ablation irradiated by femtosecond laser via simplified two-temperature model coupling molecular dynamics. *Journal of Manufacturing Processes*, 2022, 77, pp. 783–793. DOI: 10.1016/j.jmapro.2022.03.048

39 Tsukamoto, M. *et al.* Microstructures formation on titanium plate by femtosecond laser ablation. *Journal of Physics: Conference Series*, 2007, 59 (1), pp. 666–669. DOI: 10.1088/1742-6596/59/1/140

40 Zheng, B. *et al.* Ablation experiment and threshold calculation of titanium alloy irradiated by ultra-fast pulse laser. *AIP Advances*, 2014, 4 (3), pp. 1–9. DOI: 10.1063/1.4867088

41 Vorobyev, A.Y. *et al.* Femtosecond laser structuring of titanium implants. *Applied Surface Science*, 2007, 253 (17), pp. 7272–7280. DOI: 10.1016/j.apsusc.2007.03.006

42 Nayak, B.K. *et al.* Formation of nano-textured conical microstructures in titanium metal surface by femtosecond laser irradiation. *Applied Physics A: Materials Science and Processing*, 2008, 90 (3), pp. 399–402. DOI: 10.1007/s00339-007-4349-2

43 Lin, Z. *et al.* Electron-phonon coupling and electron heat capacity of metals under conditions of strong electron-phonon nonequilibrium. *Physical Review B - Condensed Matter and Materials Physics*, 2008, 77 (7), pp. 1–17. DOI: 10.1103/PhysRevB.77.075133

44 Lewis, L.J. *et al.* Laser ablation with short and ultrashort laser pulses: Basic mechanisms from molecular-dynamics simulations. *Applied Surface Science*, 2009, 255 (10), pp. 5101–5106. DOI: 10.1016/j.apsusc.2008.07.116

45 Zhigilei, L. v. *et al.* Atomistic modeling of short pulse laser ablation of metals: Connections between melting, spallation, and phase explosion. *Journal of Physical Chemistry C*, 2009, 113 (27), pp. 11892–11906. DOI: 10.1021/jp902294m

46 Inogamov, N.A. *et al.* Two-temperature relaxation and melting after absorption of femtosecond laser pulse. *Applied Surface Science*, 2009, 255 (24), pp. 9712–9716. DOI: 10.1016/j.apsusc.2009.04.139

47 Seydoux-Guillaume, A.-M. *et al.* Dominance of mechanical over thermally induced damage during femtosecond laser ablation of monazite. *European Journal of Mineralogy*, 2010, 22 (2), pp. 235–244. DOI: 10.1127/0935-1221/2010/0022-2001

48 Fang, R. *et al.* Improved two-temperature model and its application in femtosecond laser ablation of metal target. *Laser and Particle Beams*, 2010, 28 (1), pp. 157–164. DOI: 10.1017/S0263034610000030

49 Leitz, K.H. *et al.* Metal ablation with short and ultrashort laser pulses. *Physics Procedia*, 2011, 12 (PART 2), pp. 230–238. DOI: 10.1016/j.phpro.2011.03.128

50 Nicolodelli, G. *et al.* Influence of effective number of pulses on the morphological structure of teeth and bovine femur after femtosecond laser ablation. *Journal of Biomedical Optics*, 2012, 17 (4), p. 048001. DOI: 10.1117/1.jbo.17.4.048001

51 Valenzuela, A. *et al.* Comparison between geometrically focused pulses versus filaments in femtosecond laser ablation of steel and titanium alloys. *Applied Physics B: Lasers and Optics*, 2014, 116 (2), pp. 485–491. DOI: 10.1007/s00340-013-5724-7

52 Vorobyev, A.Y. *et al.* Multifunctional surfaces produced by femtosecond laser pulses. *Journal of Applied Physics*, 2015, 117 (3). DOI: 10.1063/1.4905616

53 Zhang, H. *et al.* Influence of laser-induced air breakdown on femtosecond laser ablation of aluminum. *Optics Express*, 2015, 23 (2), p. 1370. DOI: 10.1364/oe.23.001370

54 Rethfeld, B. *et al.* Modelling ultrafast laser ablation. *Journal of Physics D: Applied Physics*, 2017, 50 (19). DOI: 10.1088/1361-6463/50/19/193001

55 Gamaly, E.G. *et al.* Physics of ultra-short laser interaction with matter: From phonon excitation to ultimate transformations. *Progress in Quantum Electronics*, 2013, 37 (5), pp. 215–323. DOI: 10.1016/j.pquantelec.2013.05.001

56 Suslova, A. *et al.* Simulation of femtosecond laser absorption by metallic targets and their thermal evolution. *Laser and Particle Beams*, 2017, 35 (3), pp. 415–428. DOI: 10.1017/S0263034617000404

57 Žemaitis, A. *et al.* Advanced laser scanning for highly-efficient ablation and ultrafast surface structuring: experiment and model. *Scientific Reports*, 2018, 8 (1), pp. 1–14. DOI: 10.1038/s41598-018-35604-z

58 Abdelmalek, A. *et al.* Ablation of copper metal films by femtosecond laser multipulse irradiation. *Applied Sciences (Switzerland)*, 2018, 8 (10). DOI: 10.3390/app8101826

59 Dong, Y. *et al.* Numerical simulation of multi-pulsed femtosecond laser ablation: effect of a moving laser focus. *Optical Materials Express*, 2019, 9 (11), p. 4194. DOI: 10.1364/ome.9.004194

60 Ullah, M.W. *et al.* A new approach for electronic heat conduction in molecular dynamics simulations. *Modelling and Simulation in Materials Science and Engineering*, 2019, 27 (7), pp. 1–22. DOI: 10.1088/1361-651X/ab309f

61 Michalek, A. *et al.* Modelling ultrafast laser structuring/texturing of freeform surfaces. *Applied Surface Science Advances*, 2020, 2 (December), p. 100036. DOI: 10.1016/j.apsadv.2020.100036

62 Bonse, J. *et al.* Laser-Induced Periodic Surface Structures (LIPSS). *Handbook of Laser Micro- and Nano-Engineering*, 2021, 23 (3), pp. 1–59. DOI: 10.1007/978-3-319-69537-2_17-2

63 Tsibidis, G.D. *et al.* The role of crystalline orientation in the formation of surface patterns on solids irradiated with femtosecond laser double pulses. *Applied Sciences (Switzerland)*, 2020, 10 (24), pp. 1–24. DOI: 10.3390/app10248811

64 Ijaola, A.O. *et al.* Wettability Transition for Laser Textured Surfaces: A Comprehensive Review. *Surfaces and Interfaces*, 2020, 21 (October), p. 100802. DOI: 10.1016/j.surfin.2020.100802

65 Mukharamova, N. *et al.* Femtosecond laser produced periodic plasma in a colloidal crystal probed by XFEL radiation. *Scientific Reports*, 2020, 10 (1), pp. 1–11. DOI: 10.1038/s41598-020-67214-z

66 Inogamov, N.A. *et al.* Laser Ablation: Physical Concepts and Applications (Review). *High Temperature*, 2020, 58 (4), pp. 632–646. DOI: 10.1134/S0018151X20040045

67 Mazhukin, V.I. *et al.* Role of electron pressure in the problem of femtosecond laser action on metals. *Applied Surface Science*, 2020, 530 (June), p. 147227. DOI: 10.1016/j.apsusc.2020.147227

68 Bucă, A.M. *et al.* Non-fourier estimate of electron temperature in case of femtosecond laser pulses interaction with metals. *Metals*, 2020, 10 (5), pp. 1–9. DOI: 10.3390/met10050606

69 Xie, J. *et al.* Atomic simulation of irradiation of Cu film using femtosecond laser with different pulse durations. *Journal of Laser Applications*, 2020, 32 (2), p. 022016. DOI: 10.2351/1.5144512

70 Wang, X. *et al.* Simulation of femtosecond laser ablation and spallation of titanium film based on two-temperature model and molecular dynamics. *Journal of Laser Applications*, 2021, 33 (1), p. 012047. DOI: 10.2351/7.0000264

71 Pan, C. *et al.* Ultrafast optical response and ablation mechanisms of molybdenum disulfide under intense femtosecond laser irradiation. *Light: Science and Applications*, 2020, 9 (1). DOI: 10.1038/s41377-020-0318-8

72 Furukawa, Y. *et al.* Temporal change in laser penetration length of titanium and platinum for double-pulse ablation measured by a novel ablation method. *Journal of Laser Applications*, 2021, 33 (1), p. 012023. DOI: 10.2351/7.0000325

73 E. O. Hall. *The Deformation and Ageing of Mild Steel: III Discussion of Results You may also like Magnetic catalysis in AdS 4*. Cambridge, [no date].

74 Haque, M.A. *et al. Application of MEMS force sensors for in situ mechanical characterization of nano-scale thin ®lms in SEM and TEM*. [no date].

75 Sharpe, W.N. *et al. Effect of Specimen Size on Young's Modulus and Fracture Strength of Polysilicon*. 2001.

76 Espinosa, H.D. *et al. A methodology for determining mechanical properties of freestanding thin ÿlms and MEMS materials*. 2003. Available from: www.elsevier.com/locate/jmpsURL:http://clifton.mech.nwu.edu/~espinosa

77 Mcmeeking~, R.M. *FINITE DEFORMATION ANALYSIS OF CRACK-TIP OPENING IN ELASTIC-PLASTIC MATERIALS AND IMPLICATIONS FOR FRACTURE*. Pergamon Press, 1977.

78 Reimanist, I.E. *et al. EFFECTS OF PLASTICITY ON THE CRACK PROPAGATION RESISTANCE OF A METAL/CERAMIC INTERFACE*. 1990.

79 Fleck, N.A. *et al. STRAIN GRADIENT PLASTICITY: THEORY AND EXPERIMENT*. 1994.

80 Dahlberg, C.F.O. *et al.* Fractional strain-gradient plasticity. *European Journal of Mechanics, A/Solids*, 2019, 75, pp. 348–354. DOI: 10.1016/j.euromechsol.2019.02.006

81 Gurtin, M.E. *et al.* A theory of strain-gradient plasticity for isotropic, plastically irrotational materials. Part I: Small deformations. *Journal of the Mechanics and Physics of Solids*, 2005, 53 (7), pp. 1624–1649. DOI: 10.1016/j.jmps.2004.12.008

82 Fleck, N.A. *et al. A reformulation of strain gradient plasticity*. 2001. Available from: www.elsevier.com/locate/jmps

83 Gao, H. *et al.* Mechanism-based strain gradient plasticity - I. Theory. *Journal of the Mechanics and Physics of Solids*, 1999, 47 (6), pp. 1239–1263. DOI: 10.1016/S0022-5096(98)00103-3

84 Tho, K.K. *et al.* Numerical simulation of indentation with size effect. *Materials Science and Engineering: A*, 2006, 421 (1–2), pp. 268–275. DOI: 10.1016/j.msea.2006.01.070

85 Lu, Y.M. *et al.* Shear-banding Induced Indentation Size Effect in Metallic Glasses. *Scientific Reports*, 2016, 6. DOI: 10.1038/srep28523

86 Ridier, K. *et al.* Finite Size Effects on the Switching Dynamics of Spin-Crossover Thin Films Photoexcited by a Femtosecond Laser Pulse. *Advanced Materials*, 2019, 31 (25), pp. 1–7. DOI: 10.1002/adma.201901361

87 Uchic, M.D. *et al.* Sample dimensions influence strength and crystal plasticity. *Science*, 2004, 305 (5686), pp. 986–989. DOI: 10.1126/science.1098993

88 Pharr, G.M. *et al.* The indentation size effect: A critical examination of experimental observations and mechanistic interpretations. *Annual Review of Materials Research*, 2010, 40, pp. 271–292. DOI: 10.1146/annurev-matsci-070909-104456

89 Swadener, J.G. *et al. The correlation of the indentation size eeect measured with indenters of various shapes*. 2002. Available from: www.elsevier.com/locate/jmps

90 McLaughlin, K.K. *et al.* Deformation underneath low-load indentations in copper. *Journal of Physics D: Applied Physics*, 2008, 41 (7). DOI: 10.1088/0022-3727/41/7/074007

91 Demir, E. *et al.* Investigation of the indentation size effect through the measurement of the geometrically necessary dislocations beneath small indents of different depths using EBSD tomography. *Acta Materialia*, 2009, 57 (2), pp. 559–569. DOI: 10.1016/j.actamat.2008.09.039

92 Kiener, D. *et al.* Microstructural evolution of the deformed volume beneath microindents in tungsten and copper. *Acta Materialia*, 2006, 54 (10), pp. 2801–2811. DOI: 10.1016/j.actamat.2006.02.024

93 Pethicai, J.B. *et al.* Hardness measurement at penetration depths as small as 20 nm. *Philosophical Magazine A*, 1983, 48 (4), pp. 593–606. DOI: 10.1080/01418618308234914

94 Buffat, Ph. *et al.* Size effect on the melting temperature of gold particles. *Physical Review A*, 1976, 13 (6), pp. 2287–2298. DOI: 10.1103/PhysRevA.13.2287

95 Zhang, M. *et al.* Size-dependent melting point depression of nanostructures: Nanocalorimetric measurements. *Physical Review B*, 2000, 62 (15), pp. 10548–10557. DOI: 10.1103/PhysRevB.62.10548

96 Little, S.A. *et al.* Optical detection of melting point depression for silver nanoparticles via in situ real time spectroscopic ellipsometry. *Applied Physics Letters*, 2012, 100 (5). DOI: 10.1063/1.3681367

97 Zhang, S. *et al.* Depression of melting point and latent heat of molten salts as inorganic phase change material: Size effect and mechanism. *Journal of Molecular Liquids*, 2022, 346. DOI: 10.1016/j.molliq.2021.117058

98 Tong, X. *et al.* Effect of grain size on low-temperature electrical resistivity and thermal conductivity of pure magnesium. *Materials Letters*, 2018, 229, pp. 261–264. DOI: 10.1016/j.matlet.2018.07.037

99 Mahajan, R. *et al.* Cooling a microprocessor chip. *Proceedings of the IEEE*, 2006, 94 (8), pp. 1476–1485. DOI: 10.1109/JPROC.2006.879800

100 Yu, J.K. *et al.* Reduction of thermal conductivity in phononic nanomesh structures. *Nature Nanotechnology*, 2010, 5 (10), pp. 718–721. DOI: 10.1038/nnano.2010.149

101 Ouyang, G. *et al.* Surface energy of nanostructural materials with negative curvature and related size effects. *Chemical Reviews*, 2009, 109 (9), pp. 4221–4247. DOI: 10.1021/cr900055f

102 Klimo, O. *et al.* Short pulse laser interaction with micro-structured targets: Simulations of laser absorption and ion acceleration. *New Journal of Physics*, 2011, 13. DOI: 10.1088/1367-2630/13/5/053028

103 Pšikal, J. *et al. PIC simulations of femtosecond interactions with mass-limited targets*. [no date].

104 Derrien, T.J.-Y. *et al.* Insights into Laser-Matter Interaction from Inside: Wealth of Processes, Multiplicity of Mechanisms and Possible Roadmaps for Energy Localization. In: Stoian, R. et al. (eds.) *Ultrafast Laser Nanostructuring: The Pursuit of Extreme Scales*. Cham: Springer International Publishing, 2023, pp. 3–64. DOI: 10.1007/978-3-031-14752-4_1

105 Bardella, L. *et al.* Modelling the torsion of thin metal wires by distortion gradient plasticity. *Journal of the Mechanics and Physics of Solids*, 2015, 78, pp. 467–492. DOI: 10.1016/j.jmps.2015.03.003

106 Gurtin, M.E. A gradient theory of small-deformation isotropic plasticity that accounts for the Burgers vector and for dissipation due to plastic spin. *Journal of the Mechanics and Physics of Solids*, 2004, 52 (11), pp. 2545–2568. DOI: 10.1016/j.jmps.2004.04.010

107 Fleck, N.A. *et al.* Strain gradient plasticity: Theory and experiment. *Acta Metallurgica Et Materialia*, 1994, 42 (2), pp. 475–487. DOI: 10.1016/0956-7151(94)90502-9

108 Goel, S. *et al.* Twinning anisotropy of tantalum during nanoindentation. *Materials Science and Engineering: A*, 2015, 627, pp. 249–261. DOI: 10.1016/j.msea.2014.12.075

109 Wu, H.A. Molecular dynamics simulation of loading rate and surface effects on the elastic bending behavior of metal nanorod. *Computational Materials Science*, 2004, 31 (3–4), pp. 287–291. DOI: 10.1016/j.commatsci.2004.03.017

110 Yoneya, M. *et al.* Molecular dynamics simulations of pentacene thin films: The effect of surface on polymorph selection. *Journal of Materials Chemistry*, 2010, 20 (46), pp. 10397–10402. DOI: 10.1039/c0jm01577f

111 Andersen, H.C. Molecular dynamics simulations at constant pressure and/or temperature. *The Journal of Chemical Physics*, 1980, 72 (4), pp. 2384–2393. DOI: 10.1063/1.439486

112 Norman, G.E. *et al.* Atomistic Modeling of Warm Dense Matter in the Two-Temperature State. *Contributions to Plasma Physics*, 2013, 53 (2), pp. 129–139. DOI: 10.1002/ctpp.201310025

113 He, M. *et al.* Computational Study of Short-Pulse Laser-Induced Generation of Crystal Defects in Ni-Based Single-Phase Binary Solid-Solution Alloys. *Journal of Physical Chemistry C*, 2019, 123 (4), pp. 2202–2215. DOI: 10.1021/acs.jpcc.8b09922

114 Roth, J. *et al.* Molecular dynamics simulations studies of laser ablation in metals. In: *AIP Conference Proceedings*. 2012, pp. 504–523. DOI: 10.1063/1.4739905

115 Hacisalihoglu, I. *et al.* Tribocorrosion properties of different type titanium alloys in simulated body fluid. *Wear*, 2015, 332–333, pp. 679–686. DOI: https://doi.org/10.1016/j.wear.2014.12.017

116 Hundley, J.M. *et al.* Multiscale modeling of metal-composite interfaces in titanium-graphite fiber metal laminates part II: Continuum scale. *Journal of Composite Materials*, 2012, 46 (10), pp. 1235–1249. DOI: 10.1177/0021998311416685

117 Han, M.-K. *et al.* Effect of Indium Content on the Microstructure, Mechanical Properties and Corrosion Behavior of Titanium Alloys. *Metals*, 2015, 5, pp. 850–862. DOI: 10.3390/met5020850

118 Conforto, E. *et al.* A fast method for determining favourable orientation relationships and interface planes: Application to titanium-titanium hydrides

transformations. *Acta Materialia*, 2007, 55 (3), pp. 785–798. DOI: 10.1016/j.actamat.2006.06.061

119 Plimpton, S. Fast Parallel Algorithms for Short-Range Molecular Dynamics. *Journal of Computational Physics*, 1995, 117 (1), pp. 1–19. DOI: https://doi.org/10.1006/jcph.1995.1039

120 Phillips, C.L. *et al.* A two-temperature model of radiation damage in α -quartz. *Journal of Chemical Physics*, 2010, 133 (14). DOI: 10.1063/1.3481356

121 Duffy, D.M. *et al.* Including the effects of electronic stopping and electron-ion interactions in radiation damage simulations. *Journal of Physics Condensed Matter*, 2007, 19 (1), pp. 1–11. DOI: 10.1088/0953-8984/19/1/016207

122 Rutherford, A.M. *et al.* The effect of electron-ion interactions on radiation damage simulations. *Journal of Physics Condensed Matter*, 2007, 19 (49). DOI: 10.1088/0953-8984/19/49/496201

123 Jones, R. *et al. Atoms-to-Continuum (AtC) user package for LAMMPS*. [no date].

124 Hoffman, R.D. *et al. The Lattice Constants of High Purity Alpha Titanium*. [no date].

125 Al-Malkawi, G.H. *et al.* Impact of the electron-phonon coupling factor and electron heat capacity on the thermal response of targets irradiated by femtosecond laser. *Journal of Laser Applications*, 2018, 30 (4), p. 042004. DOI: 10.2351/1.5057709

126 Ji, P. *et al.* Ab initio determination of effective electron-phonon coupling factor in copper. *Physics Letters, Section A: General, Atomic and Solid State Physics*, 2016, 380 (17), pp. 1551–1555. DOI: 10.1016/j.physleta.2016.02.044

127 Çatli, S. High-density dental implants and radiotherapy planning : evaluation of effects on dose distribution using pencil beam convolution algorithm and Monte Carlo method. 2015, 16 (5), pp. 46–52.

128 Ho, C.Y. *et al.* Thermal Conductivity of the Elements. *Journal of Physical and Chemical Reference Data*, 1972, 1 (2), pp. 279–421. DOI: 10.1063/1.3253100

129 Lin, Z. *et al. THE ROLE OF THERMAL EXCITATION OF D BAND ELECTRONS IN ULTRAFAST LASER INTERACTION WITH NOBLE (Cu) AND TRANSITION (Pt) METALS*. 2007. Available from: http://www.faculty.virginia.edu/CompMat/

130 Lin, Z. *et al.* Temperature dependences of the electron-phonon coupling, electron heat capacity and thermal conductivity in Ni under femtosecond laser irradiation. *Applied Surface Science*, 2007, 253 (15), pp. 6295–6300. DOI: 10.1016/j.apsusc.2007.01.032

131 Lin, Z. *et al.* Thermal excitation of d band electrons in Au: implications for laser-induced phase transformations. In: *High-Power Laser Ablation VI*. SPIE, 2006, p. 62610U. DOI: 10.1117/12.674636

132 Mendelev, M.I. *et al.* Development of an interatomic potential for the simulation of defects, plasticity, and phase transformations in titanium. *Journal of Chemical Physics*, 2016, 145 (15). DOI: 10.1063/1.4964654

133 Stukowski, A. Visualization and analysis of atomistic simulation data with OVITO–the Open Visualization Tool. *Modelling and Simulation in Materials Science and Engineering*, 2010, 18 (1), p. 015012. DOI: 10.1088/0965-0393/18/1/015012

134 Naydenkin, E. V. *et al.* The effect of chemical and phase composition on mechanical properties and thermal stability of ultrafine-grained titanium alloys. In: *AIP Conference Proceedings*. American Institute of Physics Inc., 2019. DOI: 10.1063/1.5132106

135 Guo, F.A. *et al.* Examination of thermal properties by scanning thermal microscopy in ultrafine-grained pure titanium surface layer produced by surface mechanical attrition treatment. *Thermochimica Acta*, 2004, 419 (1), pp. 239–246. DOI: https://doi.org/10.1016/j.tca.2004.02.018

136 Goel, S. *et al.* Nanoindentation of polysilicon and single crystal silicon: Molecular dynamics simulation and experimental validation. *Journal of Physics D: Applied Physics*, 2014, 47 (27). DOI: 10.1088/0022-3727/47/27/275304

137 Popov, V. V. *et al.* Design and 3D-printing of titanium bone implants: brief review of approach and clinical cases. *Biomedical Engineering Letters*, 2018, 8 (4), pp. 337–344. DOI: 10.1007/s13534-018-0080-5

138 El-Hajje, A. *et al.* Physical and mechanical characterisation of 3D-printed porous titanium for biomedical applications. *Journal of Materials Science: Materials in Medicine*, 2014, 25 (11), pp. 2471–2480. DOI: 10.1007/s10856-014-5277-2

139 Subramani, K. Titanium surface modification techniques for implant fabrication–from microscale to the nanoscale. *Journal of Biomimetics, Biomaterials and Tissue Engineering*, 2010, 5, pp. 39–56.

140 Gorsse, S. *et al.* Additive manufacturing of metals: a brief review of the characteristic microstructures and properties of steels, Ti-6Al-4V and high-entropy alloys. *Science and Technology of Advanced Materials*, 2017, 18 (1), pp. 584–610. DOI: 10.1080/14686996.2017.1361305

Appendices

A. Material certification

Pure titanium (cast)

ADVENT
RESEARCH MATERIALS

Iraj Pariz
2 Willow Field
Eastbourne Road
Halland, Lewes
East Sussex BN8 6PS

Tel: 07849212875
E-mail: parizi@lsbu.ac.uk

Date: 3rd February 2023
Customer code: WEB006
Our Reference: 51058

Your Order no: WEB-11208
Delivery Note no: 49080
Invoice no: 51058

Certificate of Conformity

Material Description:

1x

Titanium Plate Catalogue no TI228915 Temper annealed
Purity 99.6+% Thickness 10.0mm
Size 100mm x 100mm Quantity 1pc

Batch no. Gi1764

Typical analysis ppm: C 200, N 120, H 50, Fe 1500, O 1500. Balance Ti.

ASTM B265 Grade 2.

Material in first class condition on despatch

We hereby certify that the goods listed on our delivery note dated 3rd February 2023 have been tested and inspected, and found to confirm in all respects to our order number and are in accordance with the description in our web catalogue.

advent-rm.com

Advent Research Materials Ltd
Quality assurance

ADVENT
01 Rm
1988

Advent Research Materials Ltd.
info@advent-rm.com | advent-rm.com
Tel +44 1865 88 4440 | Fax +44 1865 88 4460
ISO 9001:2015 FS 671050
Oakfield Industrial Estate, Eynsham, Oxford, England, OX29 4JA
VAT No GB 521 0593 81 | Registered in England No 2273165

Titanium alloy Ti-6Al-4V (cast)

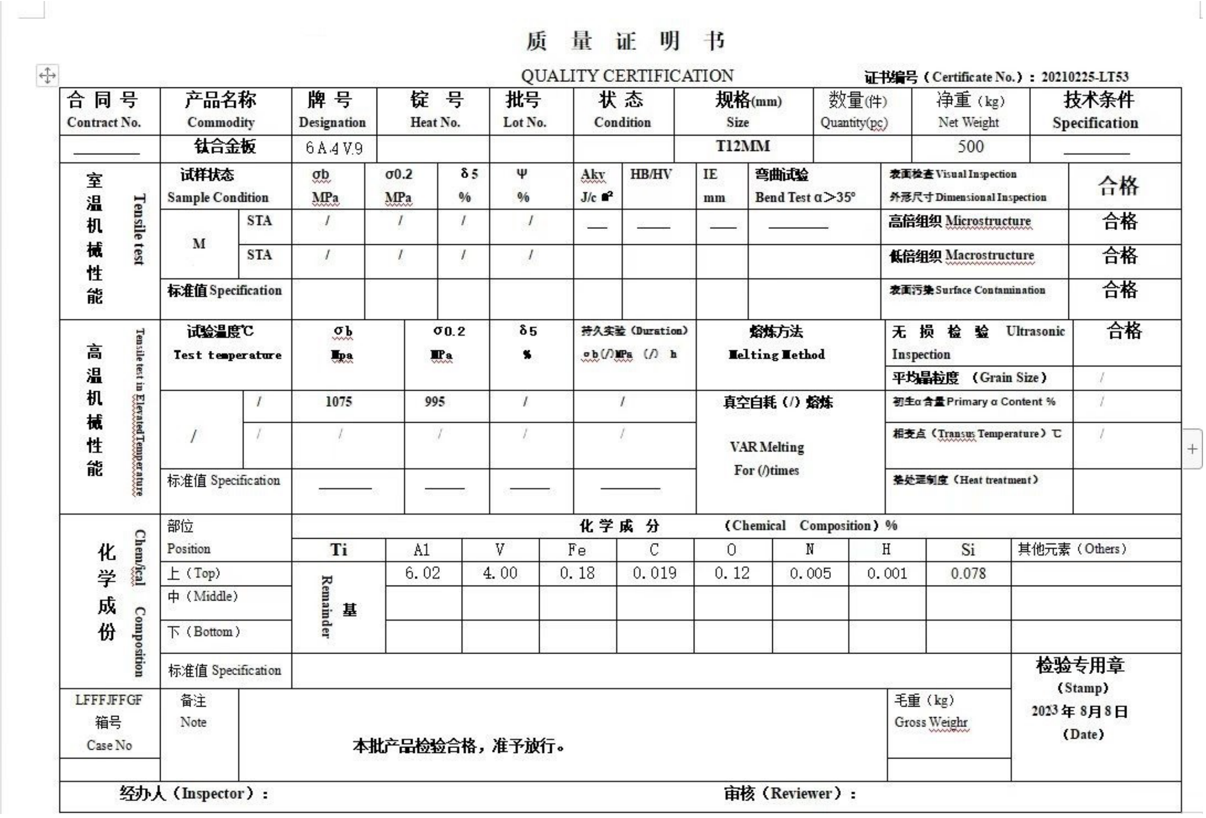

质 量 证 明 书

QUALITY CERTIFICATION

证书编号（Certificate No.）：20210225-LT53

合同号 Contract No.	产品名称 Commodity	牌号 Designation	锭号 Heat No.	批号 Lot No.	状态 Condition	规格(mm) Size	数量(件) Quantity(pc)	净重（kg） Net Weight	技术条件 Specification
————	钛合金板	6A4V9				T12MM		500	————

室温机械性能 Tensile test	试样状态 Sample Condition		σb MPa	σ0.2 MPa	δ5 %	Ψ %	Akv J/c㎡	HB/HV	IE mm	弯曲试验 Bend Test α>35°	表面检查 Visual Inspection 外形尺寸 Dimensional Inspection	合格
	M	STA	/	/	/	/	—	——	—	————	高倍组织 Microstructure	合格
		STA	/	/	/	/					低倍组织 Macrostructure	合格
	标准值 Specification										表面污染 Surface Contamination	合格

高温机械性能 Tensile test in Elevated Temperature	试验温度℃ Test temperature		σb Mpa	σ0.2 MPa	δ5 %	持久实验（Duration） σb(/)MPa (/) h	熔炼方法 Melting Method	无损检验 Ultrasonic Inspection	合格
								平均晶粒度（Grain Size）	/
	/	/	1075	995	/	/	真空自耗（/）熔炼 VAR Melting For (/)times	初生α含量 Primary α Content %	/
		/	/	/	/	/		相变点（Transus Temperature）℃	/
	标准值 Specification		————	———	———	————		热处理制度（Heat treatment）	

化学成份 Chemical Composition	部位 Position	化学成分（Chemical Composition）%									
		Ti	Al	V	Fe	C	O	N	H	Si	其他元素（Others）
	上（Top）	基 Remainder	6.02	4.00	0.18	0.019	0.12	0.005	0.001	0.078	
	中（Middle）										
	下（Bottom）										
	标准值 Specification										

LFFFJFFGF 箱号 Case No	备注 Note	本批产品检验合格，准予放行。	毛重（kg） Gross Weighr	检验专用章 （Stamp） 2023年8月8日 （Date）

经办人（Inspector）：

审核（Reviewer）：

Titanium alloy Ti-6Al-4V (powder)

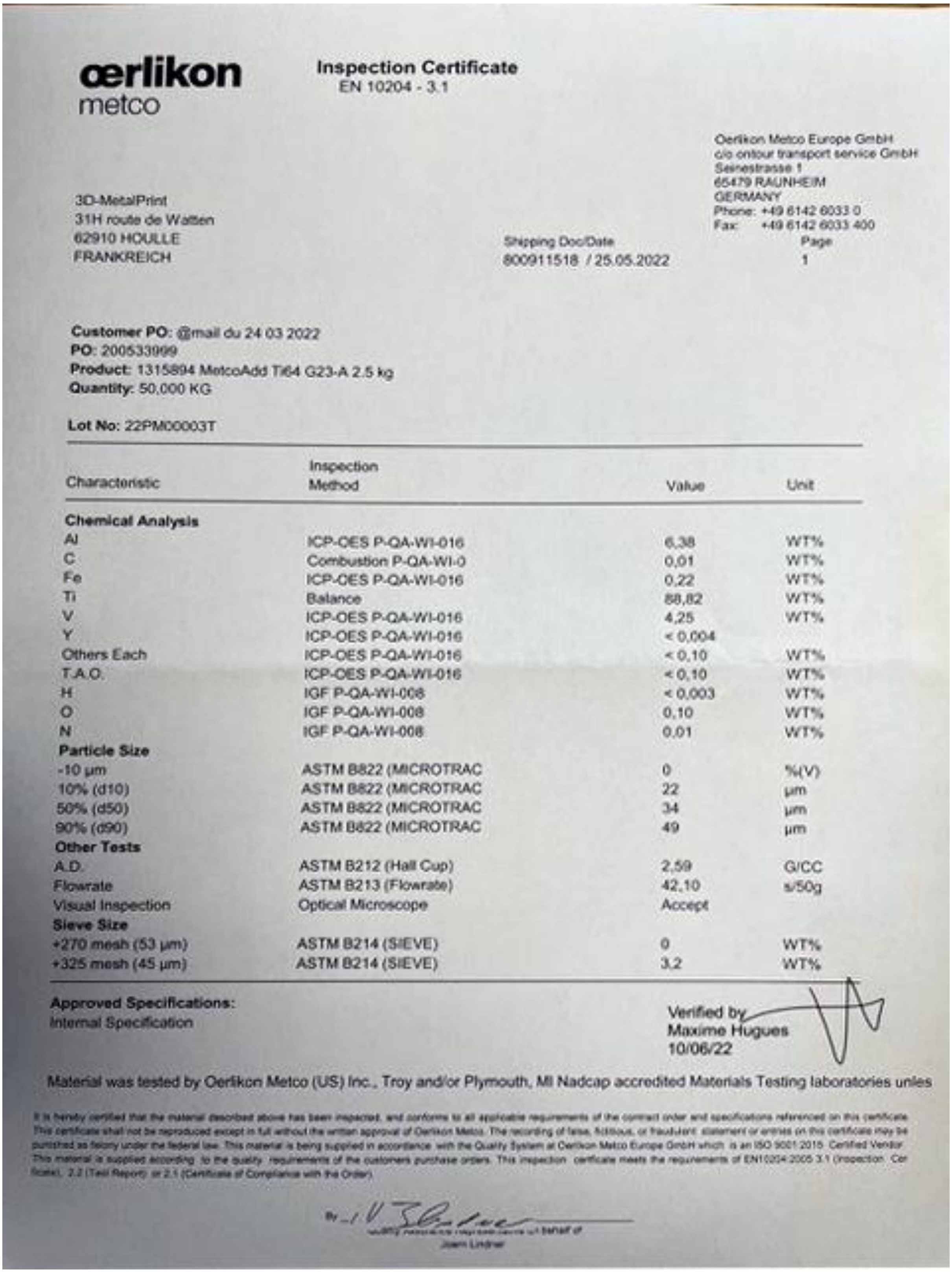

œrlikon
metco

Inspection Certificate
EN 10204 - 3.1

Oerlikon Metco Europe GmbH
c/o ontour transport service GmbH
Seinestrasse 1
65479 RAUNHEIM
GERMANY
Phone: +49 6142 6033 0
Fax: +49 6142 6033 400

3D-MetalPrint
31H route de Watten
62910 HOULLE
FRANKREICH

Shipping Doc/Date
800911518 / 25.05.2022

Page
1

Customer PO: @mail du 24 03 2022
PO: 200533999
Product: 1315894 MetcoAdd Ti64 G23-A 2.5 kg
Quantity: 50,000 KG

Lot No: 22PM00003T

Characteristic	Inspection Method	Value	Unit
Chemical Analysis			
Al	ICP-OES P-QA-WI-016	6,38	WT%
C	Combustion P-QA-WI-0	0,01	WT%
Fe	ICP-OES P-QA-WI-016	0,22	WT%
Ti	Balance	88,82	WT%
V	ICP-OES P-QA-WI-016	4,25	WT%
Y	ICP-OES P-QA-WI-016	< 0,004	
Others Each	ICP-OES P-QA-WI-016	< 0,10	WT%
T.A.O.	ICP-OES P-QA-WI-016	< 0,10	WT%
H	IGF P-QA-WI-008	< 0,003	WT%
O	IGF P-QA-WI-008	0,10	WT%
N	IGF P-QA-WI-008	0,01	WT%
Particle Size			
-10 µm	ASTM B822 (MICROTRAC	0	%(V)
10% (d10)	ASTM B822 (MICROTRAC	22	µm
50% (d50)	ASTM B822 (MICROTRAC	34	µm
90% (d90)	ASTM B822 (MICROTRAC	49	µm
Other Tests			
A.D.	ASTM B212 (Hall Cup)	2,59	G/CC
Flowrate	ASTM B213 (Flowrate)	42,10	s/50g
Visual Inspection	Optical Microscope	Accept	
Sieve Size			
+270 mesh (53 µm)	ASTM B214 (SIEVE)	0	WT%
+325 mesh (45 µm)	ASTM B214 (SIEVE)	3,2	WT%

Approved Specifications:
Internal Specification

Verified by
Maxime Hugues
10/06/22

Material was tested by Oerlikon Metco (US) Inc., Troy and/or Plymouth, MI Nadcap accredited Materials Testing laboratories unles

It is hereby certified that the material described above has been inspected, and conforms to all applicable requirements of the contract order and specifications referenced on this certificate. This certificate shall not be reproduced except in full without the written approval of Oerlikon Metco. The recording of false, fictitious, or fraudulent statement or entries on this certificate may be punished as felony under the federal law. This material is being supplied in accordance with the Quality System at Oerlikon Metco Europe GmbH which is an ISO 9001:2015 Certified Vendor. This material is supplied according to the quality requirements of the customers purchase orders. This inspection certificate meets the requirements of EN10204:2005 3.1 (Inspection Certificate), 2.2 (Test Report) or 2.1 (Certificate of Compliance with the Order).

By
quality assurance representative on behalf of
Joern Lindner